The Henryk Niewodniczański
Institute of Nuclear Physics
Polish Academy of Sciences

Report No 1940/PH

Energy Evolution of the Total Cross Sections – Significance of the HERA γp Measurements

Janusz Chwastowski

Habilitation Thesis
Praca Habilitacyjna

Abstract

A similarity of the energy dependence of the total cross sections for various hadron–hadron interactions has been confirmed by a number of experiments. This similarity is most remarkable at high centre–of–mass energies. HERA accelerator offers a unique opportunity to study the photoproduction from a nucleon at the highest energies possible nowadays. Photoproduction was studied for the process $e^{\pm}p \rightarrow e^{\pm}\gamma^*p \rightarrow e^{\pm} + X$ where X represents the hadronic final state and γ^* is the quasi-real photon. The experimental results on the photoproduction obtained by the H1 and ZEUS Collaborations are reviewed. The measurement of the total cross section for photoproduction is reported in great detail. The photoproduction total cross section measurements are discussed with in the framework of phenomenological models. They show that the energy dependence of the total cross section for photoproduction is similar to the one observed for hadronic interaction. Possible extensions of the photoproduction measurements to the lepton-nucleus collisions are outlined.

Contents

Chapter 1

Introduction

The study of the total cross section played a crucial role in nuclear and particle physics. The total cross section is related to the probability of an interaction and hence its measurement is one of the basic measurements to be performed. The energy dependence of the total cross section for various interactions was extensively investigated both experimentally and theoretically. The (anti-)proton–proton scattering is one of the most investigated processes in a very broad energy range. At the centre-of-mass energy, s, below a few GeV the total cross section has a complicated structure showing formation of excited states or resonances. For larger energies it decreases and at energies above few tens of GeV it starts to increase slowly with centre–of–mass energy.

In the optical model [1] the total cross section is related directly to the size of an object. Indeed
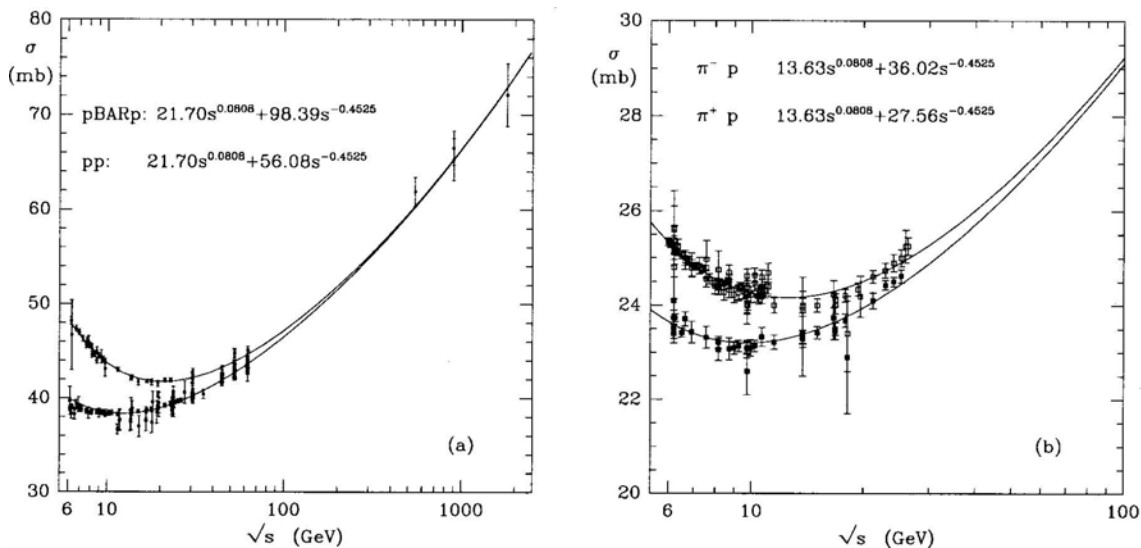

Figure 1.1: The total cross section for: (a) pp and $\bar{p}p$ collisions, (b) π^+p and π^-p scattering as a function of the centre–of–mass energy. The cross sections show a universal rise at high-energy, $\sigma \sim s^{0.08}$. Solid curves represent the fits of [2]. From [2].

this model quite accurately predicted the value of the pp cross section at intermediate energies. However, the model predicts an energy independent cross section.

On the other hand the cross section increase with energy was already predicted by Heisenberg [3] in 1952. His prediction was confirmed only with advent of the CERN ISR in case of the pp collisions for the cms energies between 20 and 63 GeV. This growth is observed up to the highest energies accessible in the cosmic-ray experiments [4, 5]. Moreover, measurements of the pion-proton and kaon-proton cross sections carried out at Fermilab demonstrated that the cross section growth with energy is a common property of hadron-nucleon interactions. This rise was interpreted as the hadrons appear to "expand" and become more "opaque".

The measured energy dependence of the pp, $p\bar{p}$, $\pi^+ p$ and $\pi^- p$ cross sections is shown in Fig. 1.1 together with the phenomenological parameterisation of [2]. The high-energy behaviour of the depicted cross sections is well represented by a common functional form, $\sigma \sim s^{0.08}$. This strongly suggests a possible universality of the high-energy dependence of the cross section.

A natural question is whether the cross section rise with energy will continue and how fast it is. The Froissart-Martin bound [6] implies that the cross section rise with cms energy cannot be faster than $log^2(s)$. Actually, a parameterisation [7] which is quadratic in the logarithm of the centre–of–mass energy quite well describes measured dependencies. It is worth stressing that due to this slow increase of the cross section its high energy behaviour can only be tested with precise high energy data. The high energy experiments deliver also a possibility to test another asymptotic prediction - the Pomeranchuk's theorem [8] which states that the particle and anti-particle cross section difference vanishes at asymptotic energies as compared to the cross sections themselves. The data on hadronic interactions seem to support this view (cf. Figure 1.1).

Unfortunately, the total cross section for hadronic interactions cannot yet be calculated from quantum chromodynamics (QCD). Quantum chromodynamics has been very successful in describing hadronic interactions at large momentum–transfer where perturbative methods are applicable. For low momentum–transfer values, in the long-range regime, the QCD has not yet given accurate predictions. This regime of soft hadronic interactions is dominated by phenomenological or QCD-inspired models constrained by the asymptotic theorems. Due to the non-perturbative nature of soft hadronic interactions the question why the total cross sections increase with energy remains largely unanswered.

The Regge theory [9, 10] based on analyticity, unitarity and crossing symmetry of the scattering amplitude describes the soft interactions as an exchange of trajectories related to the poles or cuts in the complex angular momentum plane. It successfully describes the high energy data on the total cross section by the exchange of the Pomeron [11] and lower-lying meson trajectories. In QCD, the Pomeron is described in terms of multi-gluon exchange and a point-like coupling to quarks and gluons. A color singlet two-gluon exchange with $C = +1$ corresponds to the Pomeron exchange while the color singlet three-gluon exchange with $C = -1$ describes the odderon [12]. Presently, various parameterisations of the cms energy dependence of the cross sections exist. These parameterisations, based on the phenomenological analyses of the existing data, usually make use of the scattering matrix analytic properties, the Regge theory and of the additive quark model [13]. They give a good account of the measured dependencies. The increase of the cross section at high energies is related to the Pomeron exchange.

Experimental data show that the photoproduction from a nucleon has features similar to the ones observed in hadron–hadron interaction. In particular, the total cross section shows qualitatively the same energy dependence. A similar behaviour is also observed for the $\gamma\gamma$ collisions.

This similarity suggests a possible universality of the total cross section energy dependence at high energies for all these types of interactions. Another feature seen in the photoproduction data was a copious production of the vector meson states. This gave a rise to the vector meson dominance model [14] (VDM) which interpreted the photon hadronic interactions as an interaction of a mesonic vector state the photon fluctuates into with a nucleon. This model was particularly successful in describing the photoproduction data. It predicts that at very high energies where the total cross section is governed by the Pomeron exchange the pp, γp and $\gamma\gamma$ total cross sections should be related by the following factorisation relation:

$$\sigma_{TOT}^{\gamma\gamma} \cdot \sigma_{TOT}^{pp} = (\sigma_{TOT}^{\gamma p})^2. \tag{1.1}$$

Another prediction is that if, at asymptotic energies, a photon can be described entirely by the VDM then the total photoproduction cross section should have exactly the same, universal energy dependence as the hadron-proton total cross section. Therefore, it is interesting to see whether the total photoproduction cross section actually shows this cms energy dependence, i.e. whether the hadronic nature of the photon in soft interactions is maintained up to the highest energies.

The HERA ep collider allows the study of the photoproduction at the energy of 200 GeV. This is the highest energy accessible nowadays for photoproduction measurement and about an order of magnitude higher than that of the fixed target photoproduction experiments. Therefore, HERA is an ideal tool to test the high energy photoproduction cross section behaviour and hence the similarities and differences between the γp and other interactions.

The ZEUS Collaboration decided to measure the total cross section for photoproduction using the reaction $e^+ p \rightarrow e^+ \gamma^* p \rightarrow e^+ X$ where γ^* is the quasi-real photon and X denotes the hadronic final state. One should note that the total photoproduction cross section measurements were earlier published by both H1 [15] and ZEUS [16] Collaborations. The earlier ZEUS investigations were based on the data taken during an extended running period. Since the high energy tests require as precise measurements as possible then relying on the gained experience and using the acquired knowledge on both the detector and the accelerator running, the data were collected in a series of dedicated runs during a limited, relatively short time. This allowed to limit possible variations of the apparatus response, to control the experimental conditions and thus resulted in a reduction of systematic effects. The details of this measurement will be described later.

A natural extension of the photoproduction study comes from a measurement of the photon–nucleus interactions. Planned upgrade of the RHIC complex with an electron accelerator will allow the investigations of QCD at high parton densities and large values of color fields. In particular, the propagation of quarks through the nuclear matter, the dynamics of high-energy interactions of small colour singlet systems, the experimental separation between long- and short-range components of the photon and the influence of the nuclear medium on the photon–nucleon interactions can be studied experimentally.

The author of this thesis took an active part in the photoproduction total cross section measurement with ZEUS detector starting from the planning phase. He performed the so-called "first" analysis of the experimental data including both the scattered positron and the hadronic final state analyses.

Some material presented in the current thesis was published in [17, 18, 19] and presented by the author at the conferences [20, 21, 19].

3

This thesis is organised as follows. Chapter 2 introduces the basics on the cross sections. Later the theoretical aspects pertaining to the total cross section measurement for photoproduction at the *ep* collider and phenomenological models are discussed. The results on photoproduction obtained at HERA are reviewed in Chapter 3. Chapter 4 describes the experimental apparatus, data and procedure used in the $\sigma_{TOT}^{\gamma p}$ measurement with the ZEUS detector. It also introduces the experimental methods of the photoproduction total cross section measurements and compares the fixed target to storage ring methods. The measurements interpretation is also discussed there. Chapter 5 summary obtained results and observations. It also discusses possible extensions of he photoproduction measurements at an electron-ion collider.

Chapter 2

Theoretical Aspects

This chapter describes theoretical ideas related to the analysis of the total photoproduction cross section. At first the cross section definition and the kinematic variables are defined. Later the relation between the ep and $\gamma^\star p$ cross sections is introduced. Eventually, the phenomenological models describing the energy dependence of the cross section are briefly reviewed.

2.1 Cross Section Basics

A scattering experiment is one of the basic tools of particle and nuclear physics. It's aim is to study the interaction between particles and to obtain information on their internal structure.
A scattering experiment is described by the reaction

$$a + b \rightarrow c + d + ... + z \tag{2.1}$$

in which a target particle b is bombarded by the beam particle a (a projectile) of a defined energy, c, d... denote the reaction products which can be numerous. The reaction products can be registered with an appropriate apparatus.
Presently, both the beams of stable (electrons, protons, neutrons or heavy ions) and unstable (such as muons, kaons or hyperons) particles are available. The beam energy ranges between 10^{-3} eV in case of "cold" neutrons and about 1 TeV for protons.
Two points at the distance Δx can be resolved if the wavelength, λ, of the probe is comparable, i.e. $\lambda \lesssim \Delta x$. To achieve this one needs energetic beams. The de-Broglie wavelength of the beam particle is $\lambda = h/p = hc/\sqrt{2mc^2 \cdot E_{kin} + E_{kin}^2}$ where h is the Planck constant, c is the speed of light, p is the beam momentum, E_{kin} its kinetic energy, and m is the beam particle mass. For very energetic beams with $E_{kin} \gg mc^2$, $\lambda \approx hc/E$ where E is the beam particle energy. The uncertainty principle says that

$$pc \gtrsim \frac{hc}{2\pi\Delta x} \approx \frac{200 MeV fm}{\Delta x}$$

so to reveal the substructure of the target particle a beam of energy above 1 GeV is needed.

There are two categories of the experiments. The so-called fixed (stationary) target experiments use a gaseous, liquid or solid, resting targets. Another possibility is delivered by the storage rings where a collision of two beams of particles takes place. The idea of colliding beams accelerators come from simple observation that for two beams of the same type colliding at the zero angle the laboratory frame is also the centre–of–mass frame. The beams of electrons, positrons, protons and anti-protons or ions are used.

The target and beam particles can preserve their identities (however they can change their four-momenta) so one deals with an elastic reaction. The spatial shape of the target can be deduced from the scattering rate dependence on the beam energy and scattering angle.

In the inelastic process a part of available energy excites the initial state particles into a higher state which subsequently decays into one or more particles.

If all the products of a reaction are measured and identified then one deals with an *exclusive* measurement. The *inclusive* measurement is a measurement in which only one, final state particle is selected, identified and measured irrespectively of the rest of the final state. Usually, it is denoted by

$$a + b \rightarrow c + X.$$
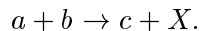
The scattering experiments yield information on both the kinematics and the dynamics of the reaction studied. Primarily measured and analysed quantities are the reaction rates, the energy spectra and the angular distributions of the reaction products. A fundamental quantity which measures the probability of a reaction is the cross section, σ.

The cross section for the reaction 2.1 can be defined as

$$\sigma = \frac{interaction \; rate \; \mathcal{R}}{(unit \; incident \; flux) \cdot (target \; particle)}.$$

If the beam contains n_a particle and v_i is the relative speed of particles a and b then the flux, $\mathcal{F}$, per unit time per unit area is given by

$$\mathcal{F} = n_a \cdot v_i.$$

If the number of target particles per unit area is n_b then the chance of an interaction is $\sigma \cdot n_b$ and the number of the interactions per unit time is $\sigma \cdot n_b n_a v_i$. Thus the interaction rate per target particle is $\mathcal{R} = \sigma \cdot n_a v_i$ and hence

$$\mathcal{R} = \sigma \cdot \mathcal{F}.$$

The cross sections is measured in *barns* (1 barn = $10^{-28} m^2$) and it is related to the probability that one event occurs for one beam particle incident at right angle on a material containing 1 scattering centre per 1 cm^2.

The interaction rate, $\mathcal{R}$, is the product of the density of final states (the Lorentz invariant phase space factor), ρ_f, and the matrix element $\mathcal{M}_{if}$ which describes the transition between the initial and final states, i.e.

$$\mathcal{R} = \frac{2\pi}{\hbar} |\mathcal{M}_{if}|^2 \rho_f.$$

The matrix element contains "whole" physics of the process considered: the energy and the coupling constant dependencies, the angular distribution and others. In case of an unpolarised cross section the matrix element has to be averaged over the spins of particles a and b. One should

note that for many processes for which the coupling constant is large the matrix element cannot be calculated by the theory. In particular the hadronic cross section cannot yet be calculated within QCD. A representation of the matrix element pertaining to the photoproduction cross section measurement will be discussed later.

On the other hand it is useful to introduce the cross section in an operational manner.

Consider a beam of n particles per unit area and per unit time. The beam bombards a slab of target material of thickness t containing N scattering or absorption centres per unit volume. The chance that an interaction takes place while passing through a lamina of thickness dx and area A (see Fig. 2.1) is

$$\frac{NAdx\sigma}{A} = N\sigma dx = dx/l$$

where l has the dimensions of length and is called the mean free path for a collision. Additionally,
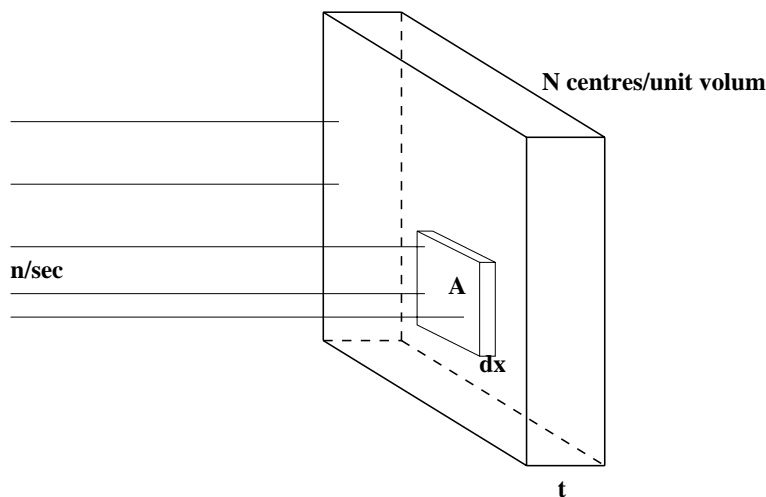
Figure 2.1: Cross section definition.

it is assumed that the flux of incident particles is small so particles do not interfere, in each scattering process only one particle takes part and the removal of target particles due to recoil can be neglected.

If all possible interactions between the beam and target particles are summed then one talks about the total cross section, σ_{tot}. In analogy, the cross section for the elastic reaction, $\sigma_{el.}$ and for the inelastic reaction, $\sigma_{in.}$ can be defined. Obviously, $\sigma_{tot} = \sigma_{el.} + \sigma_{inel.}$.

The beam attenuation is

$$dn = -nN\sigma dx.$$

The number of unscattered particles observed behind the slab is then

$$n(t) = n \exp\left(-N\sigma t\right) = n \exp\left(-\mu t\right)$$

where $\mu = N\sigma = 1/l$ is the linear attenuation coefficient for collision of a beam in a given material and has the dimensions of cm^{-1}. The mass attenuation coefficient $\mu_m = \mu/\rho$ (ρ is the

7

material density) is measured in cm^2/g and

$$\mu_m = \frac{\mu}{\rho} = \frac{N\sigma}{\rho} = \frac{\sigma}{m_a}$$

where m_a is the mass of the scattering centre. The number of the collisions, or the yield, is

$$Y = n - n(t) = n[1 - \exp(-N\sigma t)].$$

For small attenuation $Y \approx nNt\sigma$ which gives

$$\sigma = \frac{Y}{nNt}. \tag{2.2}$$

The above equation is the basis for a classical measurement of the cross section in a transmission
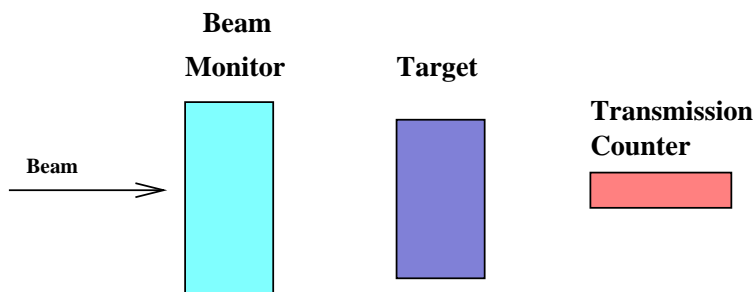
Figure 2.2: Schematic view of the transmission experiment.

experiment. A schematic view of the transmission experiment is shown in Fig. 2.2. The apparatus consists of three parts:

- the beam monitor,

- the target,

- the transmission counter.

The σ_{tot} value is deduced from the number of unscattered projectiles. One should note that the term "unscattered" means the zero angle scattering. The Coulomb scattering and the experimental resolution limits the measurement to the number of particles scattered at angle, Θ, smaller than some maximum angle, Θ_{max}. In other words the transmission is measured as a function $F(\Theta_{max})$ and the number of unscattered particles is deduced by extrapolating the value of $F(\Theta_{max})$ to $\Theta_{max} = 0$.

A variation of the transition experiment is a total absorption measurement. It is a very useful way to determine the total cross section for an interaction of particles with matter. The measurement is repeated in turn for different thicknesses of the target. The procedure is stopped when the transmission counter shows only the background counts. The method requires a very detailed knowledge of the background in vicinity of the experimental setup.
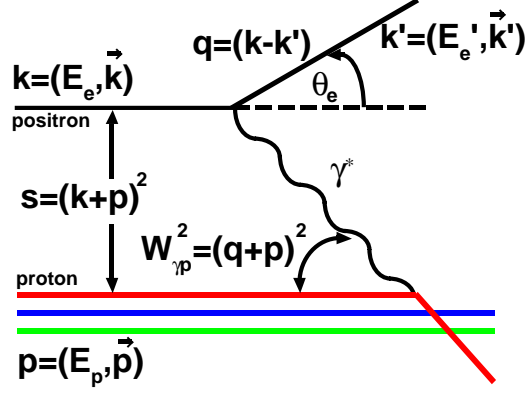
Figure 2.3: Kinematic variables used to describe low-Q^2 ep interactions.

2.2   Event Kinematics

In the following the coordinate system is a right-handed Cartesian system with Z axis pointing in the proton direction and horizontal X axis pointing to the left.

A diagram of the ep interaction for low momentum transfers is shown in Fig. 2.3. The incoming positron has four momentum k and its energy is E_e. The scattered positron energy is E'_e and its four-momentum is denoted by k'. The incoming proton has energy E_p and four-momentum p. The positron mass is m_e and the proton mass is m_p. The event kinematics may be described in terms of the Lorentz-invariant variables, Q^2 and y, the photon virtuality and event inelasticity, respectively, where

$$Q^2 = -q^2 = -(k - k') \ ,$$

and

$$y = \frac{p \cdot q}{p \cdot k} \ .$$

The exchanged photon energy is

$$\nu = \frac{p \cdot q}{m_p}$$

and x - Bjorken scaling variable is

$$x = \frac{Q^2}{2p \cdot q}.$$

The photon-proton centre-of-mass energy is given by

$$W^2 = W^2_{\gamma p} = (q + p)^2 \ .$$

In terms of experimental variables,

$$Q^2 = Q^2_{\min} + 4E_e E'_e \sin^2 \frac{\theta_e}{2},$$

where θ_e is the positron scattering angle (see Fig. 2.3),

$$W = W_{\gamma p} = 2\sqrt{E_e E_p y}.$$

The inelasticity has particularly simple form in the proton rest frame

$$y = 1 - \frac{E'_e}{E_e}.$$

The minimum value of Q^2 at a given inelasticity is

$$Q^2_{\min} = \frac{m_e^2 y^2}{1 - y} .$$

A very useful variable is the pseudorapidity,

$$\eta = -\frac{1}{2} \ln \tan \frac{\theta}{2}$$

where θ is the particle polar angle.

2.3   Electron - Proton Cross Section

The cross section can be expressed as

$$d\sigma = \frac{1}{\mathcal{F}} |\mathcal{M}|^2 dLips$$

where $\mathcal{F}$ is the flux of available particles, $dLips$ is the Lorentz invariant phase space that gives the number of final states. The physics of the interaction is described by the invariant amplitude $\mathcal{M}$ which in case of the unpolarised cross section has to be averaged over the incoming particles' spins and summed over the spins of final state particles. Since to the lowest order the electron–proton scattering is mediated by a photon the amplitude $\mathcal{M}$ can be expressed using the leptonic, $L_{\mu\nu}$, and hadronic, $W_{\mu\nu}$, tensors as

$$|\mathcal{M}|^2 = \frac{16\pi^2 \alpha^2}{q^4} L^{\mu\nu} 4\pi m_p W_{\mu\nu}.$$

The leptonic tensor is given by

$$L_{\mu\nu} = 2(k'_\mu k_\nu + k_\mu k'_\nu + \frac{q^2}{2} g_{\mu\nu}).$$

The hadronic tensor $W_{\mu\nu}$ which describes the electromagnetic structure of the target cannot be calculated from first principles. It depends on two four-vectors p and q. Using the conservation laws for the unpolarised cross section the tensor can be written in terms of two scalar functions W_1 and W_2

$$W_{\mu\nu} = \left(-g_{\mu\nu} + \frac{q_\mu q_\nu}{q^2} \right) W_1 + \left(p_\mu - q_\mu \frac{p \cdot q}{q^2} \right) \left(p_\nu - q_\nu \frac{p \cdot q}{q^2} \right) \frac{W_2}{m_p^2}.$$

Hence

$$d^2\sigma^{ep} = \frac{1}{2s} \frac{16\pi^2 \alpha^2}{Q^4} 4\pi m_p \left[2W_1 Q^2 \left(1 - \frac{2m_e}{Q^2} \right) + W_2 \frac{s^2}{m_p^2} \left(1 - y + \frac{m_p^2 xy}{s} \right) \right] \frac{1}{4(2\pi)^2} dQ^2 dy.$$

Defining the proton structure functions

$$F_1(y, Q^2) = m_p W_1(y, Q^2)$$

and

$$F_2(y, Q^2) = \nu W_2(y, Q^2)$$

the double differential neutral current ep cross section can be written as

$$\frac{d^2\sigma^{ep}}{dQ^2 dy} = \frac{4\pi\alpha^2}{Q^4}\left[y\left(1 - \frac{2m_e^2}{Q^2}\right)xF_1(y, Q^2) + \frac{1}{y}\left(1 - y - \frac{xym_p^2}{s}\right)F_2(y, Q^2)\right]. \qquad (2.3)$$

The ep cross section can be interpreted [22, 23] as a product of a flux of virtual photons and the total cross section, $\sigma_{tot}^{\gamma^\star p}$, for the scattering of virtual photons off protons. If K is the photon energy, ϵ_λ^μ is the polarisation vector for the virtual photon helicity λ then the total $\gamma^* p$ cross section is

$$\sigma_\lambda = \frac{4\pi^2\alpha}{K}\epsilon_\lambda^\mu \epsilon_\lambda^\nu W_{\mu\nu}.$$

In case of real photons the flux factor is $4m_p K$ and the photon is transversely polarised ($\lambda = \pm 1$). For virtual photons, similarly to the massive spin 1 particle, the polarisation vector is

$$\epsilon_\pm^\mu = \pm\frac{1}{\sqrt{2}}(0; 1; \pm i; 0) \qquad\qquad \epsilon_0^\mu = \pm\frac{1}{\sqrt{Q^2}}(\sqrt{\nu^2 + Q^2}; 0; 0; \nu).$$

In this case the flux factor is not a well defined concept. Usually two definitions are used. Both require that $K \to \nu$ when $Q^2 \to 0$. The Gilman flux factor [22] is proportional to $K_G = \sqrt{Q^2 + \nu^2}$ - the virtual photon momentum. The Hand convention [23] requires that K is the real photon energy needed to create an equivalent invariant mass for a virtual photon and the flux factor is proportional to $K_H = \nu - Q^2/2m_p = \nu(1 - x)$.
The transverse and longitudinal photon–proton cross sections are

$$\sigma_T = \frac{\sigma_+ + \sigma_-}{2} = \frac{4\pi\alpha^2}{K}W_1$$

$$\sigma_L = \sigma_0 = \frac{4\pi\alpha^2}{K}\left[\left(1 + \frac{\nu^2}{Q^2}\right)W_2 - W_1\right].$$

The above can be re-written in terms of the structure functions F_1 and F_2 as

$$\sigma_T = \frac{4\pi\alpha^2}{m_p K}F_1$$

and

$$\sigma_L = \frac{4\pi\alpha^2}{m_p K}\left(\frac{F_2}{2x} - F_1\right) = \frac{4\pi\alpha^2}{m_p K}\frac{F_L}{2x}$$

where $F_L = F_2 - 2xF_1$ is the longitudinal structure function. Using the above relations to determine the structure functions and introducing the result into Eqn. 2.3 one obtains the

11

double differential neutral current cross section in terms of the virtual photon transverse and longitudinal cross sections (the equivalent photon approximation [24])

$$\frac{d^2\sigma_{tot}^{ep}(y,Q^2)}{dydQ^2} = \frac{\alpha}{2\pi}\frac{1}{Q^2}\left[\ \left(\frac{1+(1-y)^2}{y} - \frac{2(1-y)}{y}\frac{Q_{\min}^2}{Q^2}\right)\ \cdot \sigma_T^{\gamma^\star p}(y,Q^2)\right.$$
$$\left. + \frac{2(1-y)}{y}\cdot\sigma_L^{\gamma^\star p}(y,Q^2)\right]. \qquad (2.4)$$

The above formula is used to extract the $\gamma^\star p$ cross section from the measured ep cross section.

2.4   Regge Phenomenology

The Regge theory [9, 10] describes the cross section behaviour in the high energy limit. It is very successful in describing the data. However, it does not deliver the explanation of hadronic interactions in terms of the QCD. The Regge approach establishes a connection between the high energy scattering and a spectrum of particles and resonances. One should note that there are attempts to derive the Regge theory on the QCD grounds (for example see [25] for a review of ideas).

The theory uses a concept of the complex angular momentum to describe the scattering amplitude. In its relativistic formulation a high energy behaviour of the amplitude is related to the singularities in the complex momentum plane of the partial wave in crossed channel. The Regge theory is based on the scattering matrix unitarity and analyticity. It makes the use of the crossing symmetry which relates the two body scattering processes $AB \rightarrow CD$ and $A\bar{C} \rightarrow \bar{B}D$. In the former the centre–of–mass energy is $s = (p_A + p_B)^2$ and the four-momentum transfer $t = (p_A - p_C)^2$ defines the scattering angle. In the latter reaction the role of the two variables is interchanged. The crossing symmetry implies that the two processes are described by the same amplitude since the object exchanged in the first process and created in the second have the same quantum numbers. The simplest singularities are the Regge poles the exchange of which is a generalisation of an exchange of a particle with spin j to complex values of j. The Regge theory describes the interaction by including exchanges with all possible j-values (with the same quantum numbers) fulfilling thus the Froissart–Martin bound [6] for the total cross sections. A plot of the exchanged particle spin j versus its mass m_j^2 shows that all possible exchanges form trajectories called the Regge trajectories or Reggeons. In particular, it was found that the trajectories can be parameterised by a linear function $\alpha(t) = \alpha_0 + \alpha' t$ such that $\alpha(t)$ passes through integer values of j for $t = m_j^2$. The two-particle scattering amplitude $A(s,t)$, as a function of the cms energy, s, and the four-momentum transfer, t, can be decomposed into partial waves

$$A(s,t) = \sum_{l=0}^{\infty}(2j+1)A_j(t)P_j(\cos\Theta_t)$$

where $A_j(t)$ is the partial wave amplitude, P_j is the j-order Legendre polynomial and $cos\Theta_t = 1+2s/(t-4m^2)$. If the partial wave corresponds to the exchange of a particle described by spin j and mass m_j the amplitude is given by

$$A_j(t) = \frac{\beta(t)}{j-\alpha(t)}.$$

12

Regge idea was to include all particles belonging to a trajectory using an analytical continuation of the scattering amplitude into the complex angular momentum plane. Using the Sommerfeld-Watson transformation and selecting a suitable path in the complex angular momentum plane the scattering amplitude is given by the residue of the poles at $\alpha(t) = j$ and

$$A(s,t) \sim (2\alpha(t) + 1)\beta(t)\frac{P_{\alpha(t)}}{\sin(\pi\alpha(t))}.$$

Since the asymptotic form of $P_j(\cos\Theta) \to (\cos\Theta)^j$ for $\cos\Theta \to \infty$ ($s \to \infty$) then

$$A(s,t) \sim \beta(t)(\cos\Theta_t)^{\alpha(t)} \sim \beta(t)s^{\alpha(t)}.$$

Using the optical theorem $\sigma_{tot} = \frac{1}{s}ImA(s, t = 0)$ the total cross section behaves as

$$\sigma_{tot} \sim s^{\alpha(t=0)-1}.$$

Since the intercept of the ρ, ω ... trajectory is about 0.5 then the total cross section decreases with energy. However, the measurements show that the total cross section after the initial decrease starts to increase slowly with energy. This cannot be explained by known trajectories ($\alpha(t = 0) < 1$)). A new trajectory (Pomeranchuk trajectory) with the leading pole called the Pomeron was postulated [11]. It has $\alpha(t = 0) \geq 1$ and the quantum numbers of the vacuum. Since the energy dependence of the total cross section seems to be hadron type independent then the Pomeron pole is thought to be universal. It is supposed that the Pomeron exchange represents gluon exchanges.

The Regge theory predicts that for two-body reactions

$$\frac{d\sigma}{dt} \sim \frac{1}{s^2}|A(s,t)|^2 \sim F(t)\left(\frac{s}{s_0}\right)^{2(\alpha(t)-1)}$$

where $\alpha(t)$ describes the leading trajectory, $s_0 \simeq 1$ GeV^2 and $F(t)$ is a slowly varying function of t. For a linear trajectory $\alpha(t) = \alpha_0 + \alpha' \cdot t$ with α_0 and α' being its intercept and slope, the above formula can be re-written as

$$\frac{d\sigma}{dt} \sim F(t)\left(\frac{s}{s_0}\right)^{2(\alpha_0-1)} \exp\{2\alpha' log(s/s_0)t\}.$$

Thus the Regge exchange with linear trajectory predicts an exponential fall-off of the t-distribution with the slope parameter which increases with increasing energy. This means that small scattering angles become more preferable or in other words the forward scattering peak becomes sharper or "shrinks" with increasing energy.

2.5 Vector Meson Dominance Model

The Vector Meson Dominance Model [14] (VDM) was devised to explain the experimental data on γp interactions at low energies. In this model the photon is assumed to be a superposition of two states: a *bare*-photon $|\gamma_B >$ and a hadronic $\sqrt{\alpha}|h >$ state

$$|\gamma > = \sqrt{Z_3}|\gamma_B > + \sqrt{\alpha}|h >$$

where α is the fine-structure constant and $\sqrt{Z_3}$ gives a proper normalisation. The hadronic component undergoes hadronic interactions. The photon hadronic component is suppressed by $\sqrt{\alpha}$, nevertheless it is dominant at low Q^2 since the hadronic cross sections are large. The *bare*-photon component is responsible for the interactions between the photon and partonic constituents of the target. The VDM in its simplest form neglects *bare*-photon component interactions and restricts the hadronic component to the lowest vector meson states (ρ, ω, ϕ). The model predicts that

$$\sigma_T^{\gamma^\star p}(W, Q^2) = \sum_{V=\rho,\omega,\phi} \frac{4\alpha\pi}{f_V^2} \left(\frac{m_V^2}{Q^2 + m_V^2} \right)^2 \sigma_V \qquad (2.5)$$

and

$$\sigma_L^{\gamma^\star p}(W, Q^2) = \sum_{V=\rho,\omega,\phi} \frac{4\alpha\pi}{f_V^2} \frac{\xi_V Q^2}{m_V^2} \left(\frac{m_V^2}{Q^2 + m_V^2} \right)^2 \sigma_V \qquad (2.6)$$

where σ_V is the cross section for a transversely polarised vector meson, m_V is the vector meson mass, f_V is the photon to vector meson coupling constant. The photon – vector meson coupling constant is assumed to be the photon energy and Q^2 independent [26] and is determined from e^+e^-–annihilation. The factor ξ_V, the ratio of the longitudinal to the transverse cross sections for the vector meson - proton interaction, was introduced [14] since the cross section for a longitudinally polarised particle can differ from that of the transversely polarised one. Its value is $0 \leq \xi_V \leq 1$ [26]. Using the optical theorem the VDM relates the total photoproduction cross section to the sum of vector meson forward production amplitudes

$$\sigma_{tot}^{\gamma p} = \sqrt{16\pi \frac{d\sigma^{\gamma p \to \gamma p}}{dt}\bigg|_{t=0}} = \sum_{V=\rho,\omega,\phi} \sqrt{16\pi \frac{4\alpha\pi}{f_V^2} \frac{d\sigma^{\gamma p \to V p}}{dt}\bigg|_{t=0}} \qquad (2.7)$$

The above formula is an approximate one. The ρ, ω and ϕ contributions give about 80% of the cross section. This fact and the observation that the photon couples to a continuum of states in e^+e^-–annihilation founded the Generalised Vector Meson Dominance model [27, 28] (GVD). In this model $\sigma_T^{\gamma^\star p}(W, Q^2)$ can be related to $\sigma_T^{\gamma p}(W)$ as

$$\sigma_T^{\gamma^\star p}(W, Q^2) = \left[\frac{r_C \cdot M_0^2}{M_0^2 + Q^2} + \sum_{V=\rho,\omega,\phi} r_V \left(\frac{m_V^2}{Q^2 + m_V^2} \right)^2 \right] \sigma_T^{\gamma p}(W) \qquad (2.8)$$

where M_0 is the lower cutoff on the mass of the continuum vector states and r_C, r_V are the constants satisfying the normalisation condition $r_C + \sum_V r_V = 1$ at $Q^2 = 0$. A similar expression can be written for the longitudinal part of the cross section with additional Q^2 dependence to ensure a proper behaviour of the cross section in the photoproduction limit. The GVD model was extended to non-diagonal transitions like $\rho p \to \rho' p$. The off-diagonal formulation of GVD [28] takes explicitly into account the $\gamma^\star \to q\bar{q}$ transitions and a QCD-inspired structure for the $(q\bar{q})p$ forward scattering amplitude. The two-gluon-exchange structure of the $(q\bar{q})p$ interactions leads to the cancellation of the diagonal and non-diagonal contributions that were postulated in [29]. The model was found [30] to reproduce the HERA data [31, 32, 33, 34]. It was shown [35] to be linked with the colour-dipole picture of deep inelastic scattering at low x. Within the Generalised Vector Dominance Model the scaling of the $\gamma^\star p$ total cross section

$$\sigma^{\gamma^\star p}(W^2, Q^2) = \sigma^{\gamma^\star p}(\eta)$$

was demonstrated [35] where η is the function which depends on the ratio of both Q^2 and W^2.

2.6 Low-x-low-Q^2 Parameterisations

2.6.1 Donnachie-Landshoff Parameterisation

In 1992 Donnachie and Landshoff introduced [2] a simple parameterisation (DL92) of the total cross sections based on the Regge theory. They parameterised the total cross sections with

$$\sigma_{tot} = X \cdot s^\epsilon + Y \cdot s^{-\eta}. \tag{2.9}$$

Both ϵ and η are the effective powers and vary slowly with centre-of-mass energy. The first term corresponds to the pomeron exchange and its energy dependence is $s^{\alpha(0)-1}$ in the Regge theory. In reality due to multiple pomeron exchanges ϵ is a little less [10] than $\alpha(0) - 1$. The second term corresponds to ρ, ω, f and a exchange. Factors X and Y are characteristic for a given reaction and are derived from the fit to the data. Since the pomeron has the quantum numbers of the vacuum its couplings to particle and anti-particle are the same. Hence, X is the same for ab and $\bar{a}b$ reactions. The fits to the pp and $\bar{p}p$ data on the total cross section yielded

$$\epsilon = 0.0808 \text{ and } \eta = 0.4525. \tag{2.10}$$

This parameterisation was very successful in describing the pp and $\bar{p}p$ data from 5 to 1800 GeV and the photoproduction data.

In 1998 Donnachie and Landshoff extended their model [36] (DL98). They introduced a concept of two pomerons an "old" one called the "soft pomeron" and a "new" one called the "hard pomeron". The pomerons are assumed to be simple poles in the complex angular momentum plane. The pomerons' contributions are Q^2 independent. Each contribution is a simple power of W multiplied by an unknown function of Q^2. Hence, the proton structure function is the sum of the three terms corresponding to the two pomerons and a reggeon,

$$F_2(x, Q^2) = \sum_{i=0}^{3} f_i(Q^2) x^{-\epsilon_i}.$$

Because

$$\sigma^{\gamma p} = \frac{4\pi\alpha_{EM}}{Q^2} F_2|_{Q^2=0}$$

then F_2 has to vanish linearly with Q^2 at fixed W. Consequently $f_i(Q^2)$ vanishes like $(Q^2)^{1+\epsilon_i}$. The authors fixed the values of $\epsilon_1 = 0.0808$ and $\epsilon_2 = 0.4525$ from hadron-hadron data and added a third term ϵ_0 corresponding to the hard pomeron exchange. As a first approximation they parameterised the $f_i(Q^2)$ as in the case of DL92, i.e.

$$f_i(Q^2) = A_i \left(\frac{Q^2}{Q^2 + a_i} \right)^{1+\epsilon_i}$$

and fitted the data for $x < 0.07$ and $\sqrt{s} > 6$ GeV. Since the $f_i(Q^2)$ are unknown then it is not to be expected that the above approximation will work for any Q^2. To extract ϵ_0 they used the

data for $Q^2 < 10$ GeV^2 including these at $Q^2 = 0$. Later they extracted the values of $f_i(Q^2)$ at each Q^2. These results were subsequently used to find functional forms of $f_i(Q^2)$. Finally the functions

$$f_0(Q^2) = A_0 \left(\frac{Q^2}{Q^2 + a_0} \right)^{1+\epsilon_0}$$

$$f_1(Q^2) = A_1 \left(\frac{Q^2}{Q^2 + a_1} \right)^{1+\epsilon_1} \frac{1}{1 + \sqrt{Q^2/Q_1^2}}$$

$$f_2(Q^2) = A_2 \left(\frac{Q^2}{Q^2 + a_2} \right)^{1+\epsilon_2}$$

are fitted to the data keeping ϵ_1 and ϵ_2 fixed to the values of Eqn. 2.10. This fit yields $\epsilon_0 = 0.418$.

If the energy dependence of the soft and hard pomeron persists for $s \to \infty$ it will eventually conflict with Froissart-Martin unitarity bound [6]

$$\sigma_{tot} \leq C \, log(s/s_0),$$

where $C = \pi/m_\pi^2 \approx 60$ mb. Setting $s_0 = 1$ GeV the total cross section data are much below the unitarity bound at present energies.

2.6.2 Cudell et al. Parameterisation

Another Regge motivated parameterisation was introduced by Cudell and co-workers [37]. This parameterisation assumes that the cross sections should be reproduced by simplest singularities in the complex angular momentum plane. This corresponds to the exchange of bound-state trajectories i.e. simple poles. The imaginary part of the amplitude for the $h_1 \, h_2$ interactions is given by

$$ImA_{h_1 h_2}(s,t) = \Sigma_i (\pm 1)^{S_i} C_{h_1 h_2}(t) \left(\frac{s}{s_0} \right)^{\alpha_i(t)},$$

where S_i is the signature of the exchange. The constants $C_{h_1 h_2}(0)$ are process dependent and the trajectories $\alpha_i(t)$ are universal. The pomeron trajectory is responsible for the high energy growth of the cross section. The others correspond to mesons. At high energies only those with the largest intercepts contribute at $t = 0$, $\alpha_i(0) = 1/2$. The parameterisation assumes independent $C = +1$ (a/f) and $C = -1$ (ρ/ω) intercepts and the total cross section reads

$$\frac{ImA_{h_1 h_2}(s)}{s} = X^{h_1 h_2} s^\epsilon + Y_1^{h_1 h_2} s^{\eta_1} \pm Y_2^{h_1 h_2} s^{\eta_2},$$

where

$$\alpha_{\mathcal{P}} = 1 + \epsilon,$$

$$\alpha_{C=+1} = 1 + \eta_1,$$

$$\alpha_{C=-1} = 1 + \eta_2.$$

The factor $Y_2^{h_1 h_2}$ changes its sign when $h_1 h_2$ data are compared to $h_1 \bar{h}_2$. The real parts of the forward elastic amplitudes are computed from analyticity. Due to the unlimited growth of the

16

cross section with energy this parameterisation will eventually violate the unitarity bound.

In [7] Cudell et al. introduced several variations of the above type parameterisation. Some of them include also a term which is due to the triple-pole at $j = 1$ and which is quadratic in the logarithm of the cms energy. Such parameterisations "automatically" fulfill the Froissart-Martin bound. One of such parameterisations selected according to the aspects of the fit quality (see [7] for details) is assigned the highest "rank" and is subsequently used by the Particle Data Group (PDG) [38].

2.6.3 The ALLM Parameterisation

The Abramowicz-Levin-Levy-Maor parameterisation (ALLM) [39] describes the total $\gamma^\star p$ cross section above the resonance region ($W^2 > 3$ GeV^2) in whole the Q^2 range. The parameterisation is also based on the Regge motivated approach and extended to large Q^2 values in a way compatible with QCD expectations. The proton structure function is assumed to be

$$F_2(x, Q^2) = \frac{Q^2}{Q^2 + m_0}(F_2^{\mathcal{P}}(x, Q^2) + F_2^{\mathcal{R}}(x, Q^2))$$

where m_0 is the effective photon mass and $F_2^{\mathcal{P}}(x, Q^2)$ and $F_2^{\mathcal{R}}(x, Q^2)$ are contributions of the pomeron and reggeon exchanges and have a form:

$$F_2^{\mathcal{P}}(x, Q^2) = c_{\mathcal{P}}(t)x_{\mathcal{P}}^{\alpha_{\mathcal{P}}(t)}(1 - x)^{b_{\mathcal{P}}(t)},$$

$$F_2^{\mathcal{R}}(x, Q^2) = c_{\mathcal{R}}(t)x_{\mathcal{R}}^{\alpha_{\mathcal{R}}(t)}(1 - x)^{b_{\mathcal{R}}(t)}.$$

The slow varying function t is defined as

$$t = ln\frac{ln\frac{Q^2+Q_0^2}{\Lambda}}{ln\frac{Q_0^2}{\Lambda}}$$

where Λ is the QCD scale and Q_0^2 is a parameter. The functions

$$\frac{1}{x_{\mathcal{P}}} = 1 + \frac{W^2 - M^2}{Q^2 + m_{\mathcal{P}}}$$

$$\frac{1}{x_{\mathcal{R}}} = 1 + \frac{W^2 - M^2}{Q^2 + m_{\mathcal{R}}}$$

approach Bjorken x for large Q^2. Here M is the proton mass and the parameters m_0, $m_{\mathcal{P}}$, $m_{\mathcal{R}}$ and Q_0^2 allow a smooth transition to $Q^2 = 0$.

In 1997 the ALLM parameterisation was updated (ALLM97) [40]. The ALLM97 gives a good description of the data in a wide domain of Q^2 and x. Also in this parameterisation the pomeron intercept $\alpha_{\mathcal{P}}(0)$ depends on the Q^2. However, this dependence is milder than the one for the ALLM parameterisation. The intercept varies between DL92 fixed value of 1.08 at $Q^2 = 0$ and a value of ≈ 1.3 at the highest Q^2.

2.6.4 Block et al. Parameterisation

M. M. Block and others [41] introduced another type of the parameterisation. It was originally devised for the pp and $\bar{p}p$ data on the total cross sections, on the slope parameter of the elastic differential cross section and on the ratio of the real to imaginary part of the forward scattering amplitude. Block and co-workers attribute the growth of the high energy cross section with energy to the increasing number of soft partons inside the colliding particles [42]. In this model a hadron asymptotically becomes a black disk of partons. The cross sections are calculated as

$$\sigma_{tot}(s) = 2 \int \{1 - e^{-\chi_I(b,s)cos\chi_R(b,s)}\} d^2\vec{b}$$

where the complex eikonal $\chi(b,s) = \chi_R(b,s) + i \cdot \chi_I(b,s)$, and b is the impact parameter. The quark-quark, quark-gluon and gluon-gluon interactions contribute to the even eikonal profile function and

$$\chi^{even}(b,s) = \chi_{qq}(b,s) + \chi_{qg}(b,s) + \chi_{gg}(b,s).$$

Further

$$\chi^{even}(b,s) = i \left[\sigma_{qq} W(b;\mu_{qq}) + \sigma_{qg} W(b;\sqrt{\mu_{qg}\mu_{gg}}) + \sigma_{gg} W(b;\mu_{gg}) \right]$$

with σ_{ij} being the cross section of the interacting partons and $W(b;\mu)$ their overlap function in the impact parameter space.

The elastic cross section $\sigma_{el}(s)$ is given by

$$\sigma_{el}(s) = \int \left| 1 - e^{-\chi_I(b,s)+i\chi_R(b,s)} \right| d^2\vec{b}$$

and the inelastic cross section, $\sigma_{inel}(s)$, is

$$\sigma_{inel}(s) = \sigma_{tot}(s) - \sigma_{el}(s).$$

Eventually, the data for both pp and $\bar{p}p$ are fitted with the total eikonal

$$\chi^{\bar{p}p}_{pp} = \chi_{even} \pm \chi_{odd}.$$

The odd eikonal accounts for a difference between pp and $\bar{p}p$ data and it vanishes at high energies. It is parameterised [43] as

$$\chi_{odd}(b,s) = -C_{odd}\sigma_{gg}\frac{m_0}{\sqrt{s}}e^{i\pi/4}W(b;\mu_{odd})$$

where μ_{odd} is determined by the experiment and the normalisation constant C_{odd} has to be fitted.

The rising cross section is parametrized by the normalisation, the energy scale, the parameter μ_{gg} which describes the area occupied by gluons and by $\lambda = 1 + \epsilon$. The parameter λ is defined by the gluon structure function of the proton which should behave like $1/x^\lambda$ for small x. The model delivers a convenient parameterisation of the pp and $\bar{p}p$ forward scattering amplitude. Also within it the factorisation of: the cross sections, the nuclear slope parameters and the ratios of the real to imaginary part of the forward scattering amplitude was proven [44].

Assuming the additive quark model and substituting

$$\sigma_{ij} \rightarrow \frac{2}{3}\sigma_{ij}$$

18

$$\mu_{ij} \rightarrow \sqrt{\frac{3}{2}} \mu_{ij}$$

and using the probability that a photon interacts as a hadron $P_{had} = 1/240$ [41] one can calculate the photoproduction total cross section from the even eikonal. One should note that the value $P_{had} = 1/240$ is close to that of $P_{had} = 1/249 = \sum_{\rho,\omega,\phi} 4\pi\alpha/f_V^2$ (for $f_\rho^2/4\pi = 2.2$, $f_\omega^2/4\pi = 23.6$ and $f_\phi^2/4\pi = 18.4$) obtained [26] within the VDM. In that sense a parameter-free description of the photoproduction cross section, of the phase of the forward scattering amplitude and the forward slope for $\gamma p \rightarrow Vp$ ($V = \rho, \omega, \phi$) is obtained. Moreover, the total elastic and differential cross section for $\gamma p \rightarrow Vp$ can be calculated. This model gives a good description of the existing data.

2.6.5 Badełek-Kwieciński Parameterisation

The authors calculate [45, 46] the proton structure function F_2 as a sum of the vector meson and the partonic parts:
$$F_2(x, Q^2) = F_2^{(V)}(x, Q^2) + F_2^{(p)}(x, Q^2).$$

The vector meson part is given by

$$\frac{Q^2}{4\pi} \sum_V \frac{m_V^4 \sigma_{Vp}(W^2)}{\gamma_V^2(m_V^2 + Q^2)}$$

where the sum runs over the vector mesons with a mass smaller than the parameter Q_0, σ_{Vp} is the total Vp cross section estimated from the πp and Kp data and γ_V^2 is found from the leptonic width of the vector meson. The partonic part is as follows

$$F_2^{(p)}(x, Q^2) = \frac{Q^2}{Q^2 + Q_0^2} F_2^{AS}(\bar{x}, Q^2 + Q_0^2)$$

with

$$\bar{x} = \frac{Q^2 + Q_0^2}{W^2 + Q^2 - M^2 + Q_0^2},$$

were M is the proton mass, and F_2^{AS} is the structure function in the large Q^2 domain and is described by the improved parton model. Practically, the model uses lowest lying vector meson states ρ, ω, ϕ and $Q_0 = 1.2$ GeV^2. The model predicts the correct shape of the total photoproduction cross section however it overestimates its magnitude by about 10% [46]. The unitarity condition is violated in this model.

2.6.6 The CKMT Parameterisation

Cappela, Kaidalov, Merino and Tran-Than-Van use [47] a concept of the "bare" pomeron. The universal dependence of the total cross section on the energy, ν, described by ν^{Δ_0}, with $\Delta_0 \approx 0.08$, is due to the existence of absorptive corrections (re-scatterings). The "bare" pomeron intercept is much larger and in the eikonal calculations it becomes $1 + \Delta_1$ with $\Delta_1 \approx 0.13$. The more complete absorptive calculations [48] lead to the "bare" pomeron intercept of $1 + \Delta_2$

($\Delta_2 = 0.2 - 0.25$). The absorptive corrections decrease rapidly with increasing Q^2. The structure function in the region of small Q^2 ($0 \le Q^2 \le 5$ GeV^2) is parameterised as:

$$F_2(x, Q^2) = Ax^{-\Delta(Q^2)}(1-x)^{n(Q^2)+4}\left(\frac{Q^2}{Q^2+a}\right)^{1+\Delta(Q^2)} + Bx^{1-\alpha_{\mathcal{R}}}(1-x)^{n(Q^2)}\left(\frac{Q^2}{Q^2+b}\right)^{\alpha_{\mathcal{R}}}$$

with $\alpha_{\mathcal{R}}$ being the Reggeon trajectory intercept, the power $n(Q^2)$ is given by

$$n(Q^2) = \frac{3}{2}\left(1 + \frac{Q^2}{Q^2+c}\right)$$

and

$$\Delta(Q^2) = \Delta_0\left(1 + \frac{2Q^2}{Q^2+d}\right).$$

The parameters are obtained from the fit requesting that the F_2 and its *log*-derivative at $Q^2 = Q_0^2$ coincide with the one obtained from the QCD evolution equation. They use $Q_0^2 = 2$ GeV^2 and modify the F_2 by a higher-twist contribution:

$$F_2(x, Q^2) = F_2^{pert}(x, Q^2)\left(1 + \frac{f(x)}{Q^2}\right), Q^2 \ge Q_0^2.$$

For the total photoproduction cross section the parameterisation gives

$$\sigma_{tot}^{\gamma p} = 4\pi^2 \alpha_{EM}(Aa^{-(1+\Delta_0)}(2m\nu)^{\Delta_0} + Bb^{-\alpha_{\mathcal{R}}}(2m\nu)^{\alpha_{\mathcal{R}}-1}).$$

The parameters are: $A = 0.1502, a = 0.2631$ GeV^2, $\Delta_0 = 0.07684$, $d = 1.117$ GeV^2, $\alpha_{\mathcal{R}} = 0.415$, $c = 2.5489$ GeV^2. Also, this parameterisation predicts unlimited growth of the cross section.

2.6.7 Saturation Model

In [49] Golec-Biernat and Wüsthoff introduced a concept of small-x saturation. Their approach exploits the fact that the photon splits up into a quark-anti-quark pair which subsequently scatters off the proton target. The interaction of the $q\bar{q}$ pair with a proton is described by the dipole cross section, $\hat{\sigma}(x, r)$, which for small values of the separation distance between the quark and anti-quark, r, behaves like r^2 (color transparency) while for large r it flattens off and approaches a constant (saturation). An important element of the model is that the saturation radius, R_0, is x-dependent and

$$R_0(x) = \frac{1}{Q_0}\left(\frac{x}{x_0}\right)^{\lambda/2}$$

with $Q_0 = 1$ GeV. It scales the quark-anti-quark separation in the dipole cross section

$$\hat{\sigma}(x, r) = \sigma_0 \, g\left(\hat{r} = \frac{r}{R_0(x)}\right).$$

As the function g they use

$$g = 1 - e^{-\hat{r}^2}.$$

This function has properties mentioned above. However, one should note that the exact functional form of function g is not completely constrained [49] within the model. The parameters of the model σ_0, λ and x_0 are obtained from the fit to the inclusive DIS data with $x < 0.01$. The authors assume 140 MeV for a common mass of light quarks. For this value a reasonable description of the photoproduction data is obtained. The total photoproduction cross section increases logarithmically with decreasing quark mass and diverges in the limit of vanishing quark mass. In that sense the light quark mass can be used as a regulator of the photoproduction cross section. In particular the model predicts a logarithmic energy dependence of the photoproduction cross section

$$\sigma^{\gamma p} \sim log(W^2).$$

The effective pomeron intercept $\alpha_{\mathcal{P}}$ increases with increasing value of Q^2. Another consequence of the model is the geometric scaling

$$\sigma^{\gamma^* p}(x, Q^2) = \sigma(\tau)$$

with $\tau = Q^2 R_0^2(x)$. This feature is well supported by the data for $x < 0.01$ and in a wide Q^2 domain [51]. Also the proton structure function $F_2(x, Q^2)$ data [52, 53, 54] are well described. The saturation model was also applied to the diffractive deep inelastic scattering [55]. The free parameters were taken from the analysis of the inclusive ep scattering data without any further adjustments. It was found that the model well describes the shapes and the normalisation of the HERA diffractive data [56, 57]. The model predicts also an almost constant ratio of the diffractive to the total cross sections in accordance with the measurements [57].

Chapter 3

Photoproduction

Experiments show that the photoproduction from nucleons has features similar to hadron–hadron collisions [26]. The energy dependence of the total cross section resembles that of the pion–nucleon scattering (see Fig. 3.1). For low energies the resonance structure is observed. Above about 3 GeV it initially decreases and for larger centre-of-mass energies it increases slowly with energy. The Compton scattering, $\gamma p \rightarrow \gamma p$, shows a forward diffraction peak [58]
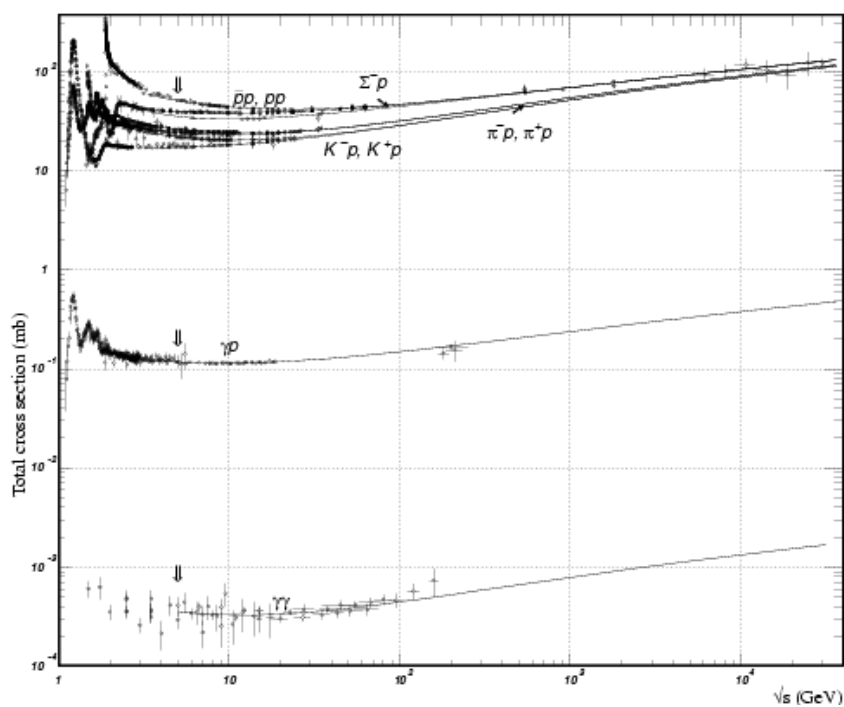

Figure 3.1: Comparison of the hadronic, γp and $\gamma\gamma$ total cross sections as a function of the centre-of-mass energy. From [38]. The solid curves represent the fits of [7].
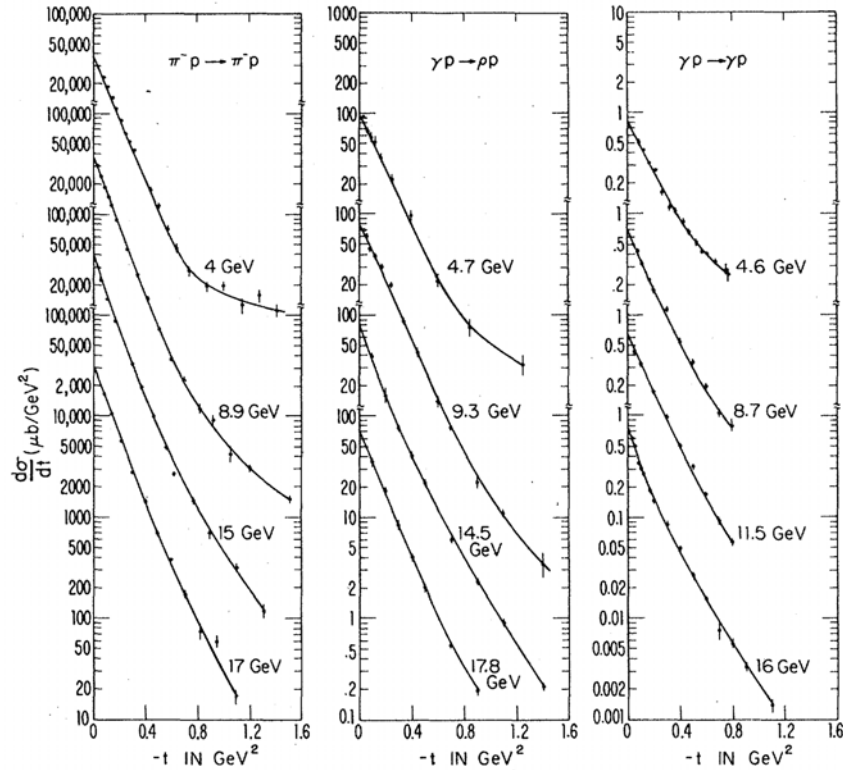
Figure 3.2: Comparison of the elastic cross section, $d\sigma/dt$, for three reactions: (a) $\pi^- p \to \pi^- p$, (b) $\gamma p \to \rho^0 p$, and (c) $\gamma p \to \gamma p$. From [26].

(see Fig. 3.2) and its amplitude is predominantly imaginary [59]. As can be observed from Fig. 3.2 the elastic cross section, $d\sigma/dt$, for the three reactions: $\pi^- p \to \pi^- p$, $\gamma p \to \rho^0 p$ and $\gamma p \to \gamma p$, follows similar behaviour with comparable values of the nuclear slope parameter, b. A copious production of the neutral vector mesons is one of the most striking features of the photoproduction.

The photon hadronic interactions can be understood bearing in mind that a photon can quantum-mechanically fluctuate into a state with photon quantum numbers ($J^{PC} = 1^{--}, Q = S = B = 0$). Thus the photon wave function can be decomposed into appropriate Fock states

$$|\gamma> = c_l|l^+l^-> + c_q|q\bar{q}> + c_b|\gamma_b>$$

where the coefficients c_l, c_q and c_b are introduced to achieve a proper normalisation.

The first term in the above relation gives the fluctuations into a pair of charged leptons and is described by QED. This is by far the largest part of the photon–matter interaction cross section. It is about two orders of magnitude larger than the sum of the two other terms for photons with energy above about 1 MeV.

Since this work concentrates on the high energy hadronic interactions of a photon then the part responsible for the lepton pair creation is neglected in the following.

23

The second and the third term are responsible for hadronic interaction of the photon in which a photon behaves as a $q\bar{q}$ pair or as a "bare", point-like, state, respectively.

If the fluctuation time [60] is large compared to the interaction time, t_i, then the interaction between the $q\bar{q}$ pair and the proton will occur. From the uncertainty principle, in the proton rest frame, the fluctuation time is given by

$$t_f = \frac{2E_\gamma}{m_{q\bar{q}}^2}$$

where E_γ is the photon energy in the proton rest frame and $m_{q\bar{q}}$ is the effective mass of the fluctuation. The interaction time is of the order of the proton radius, $t_i \approx 1$ fermi. For interactions of 10 GeV photons with a proton at rest, assuming that the $q\bar{q}$-pair is the ρ meson $t_f \approx 7$ fermi so the condition $t_f \gg t_i$ holds. For a virtual photon the fluctuation time is

$$t_f = \frac{2E_\gamma}{m_{q\bar{q}}^2 + Q^2}$$

where Q^2 is the photon virtuality. As Q^2 increases the fluctuation time gets smaller (for fixed $m_{q\bar{q}}$) and the photon does not have enough time to develop hadronic fluctuation.

This picture is often used for the photon–proton scattering subprocesses classification [61]. The $q\bar{q}$ fluctuations can have different virtualities characterised by a common transverse momentum, p_T, of the $q\bar{q}$ system with respect to the photon direction. Small virtualities result long lived fluctuations for which there is enough time to develop a gluon cloud around the $q\bar{q}$ pair and to interact as a hadronic object. This is the domain of non-perturbative QCD physics. Usually it is described by a sum over low mass vector mesons in the vector meson dominance model. The high-p_T part should be perturbatively calculable.

Summarising the photon can appear in three states: the "bare", point-like photon, the vector meson state or the perturbative $q\bar{q}$ pair. This leads to the division of γp interactions into three classes:

- the VDM class where a photon turns into a vector meson which subsequently interacts with the proton. This class contains all known from hadron induced reactions types of interaction: the elastic and diffractive scattering, and low and high-p$_t$ non-diffractive interactions,

- the direct class where a "bare" photon undergoes a point-like interaction with a parton from the proton,

- the anomalous class where the photon branches into a cascade of partons and one of these partons interacts with a parton from the proton.

Experimentally the high-p$_t$ non-diffractive interaction of the VDM class and the anomalous processes are joined into the resolved processes.

The measurements performed at HERA by the H1 and ZEUS Collaborations support the above picture.

Recent reviews of the experimental data and theoretical ideas can be found in [62, 63].

3.1 Elastic Vector Meson Production

Elastic vector meson production is the process

$$\gamma p \to V p$$

where V denotes one of the vector mesons. This reaction was extensively studied with real and virtual photons for W below 20 GeV. It exhibits features which are also characteristic for the hadronic, diffractive reactions. The energy dependence of the cross section is weak and the dependence on t, the four-momentum transfer at the proton vertex, is approximately exponential i.e. $d\sigma/dt \sim e^{-b|t|}$. This similarity can be explained on the grounds of the VDM where the photon fluctuates into a long lived vector meson state. The Regge theory predicts that the high energy part of the energy dependence of the cross section for the elastic ρ, ω and ϕ photoproduction is

$$\sigma_{\gamma p \to V p} \approx \frac{W^\delta}{b(W)}.$$

The energy dependence of the cross sections for elastic vector meson production is shown in Fig. 3.3 together with the HERA measurements [64, 65, 66, 67]. Also the data on the total photoproduction cross section are presented in this figure. Indeed the total cross section and that for the lowest lying vector mesons show a similar dependence with $\delta \approx 0.22$.

For a linear pomeron trajectory the Regge prediction for the energy dependence of the slope parameter, $b(W)$, is

$$b(W) = b_0 + 2\alpha'_{I\!P} ln\frac{W^2}{W_0^2}$$

where $\alpha'_{I\!P}$ is the pomeron trajectory slope and b_0 and W_0 are constants.
A compilation of the HERA [64, 67, 68] and low energy data [69] on the slope, b, in the case of the elastic reaction $\gamma p \to \rho p$ is presented in Fig. 3.4. A fit of the above formula is also depicted in the figure as a solid line while the fit extrapolation to lower energies is marked with the dashed line. The value of b rises with increasing W suggesting the shrinkage of the t-distribution forward peak with energy. The growth of the slope with energy is compatible with Regge prediction. The ZEUS Collaboration finds $\alpha'_{I\!P} = 0.23 \pm 0.15(stat.)^{+0.10}_{-0.07}(syst.)$ GeV^{-2} consistent with the value of 0.25 GeV^{-2} obtained [2] from hadron–hadron elastic scattering.

The photoproduction of J/Ψ was measured [71, 72, 73] at HERA. As can be seen from Fig. 3.3 its photoproduction cross section has much stronger energy dependence with $\delta \approx 0.7$. This experimental observation can be explained by perturbative QCD. The pQCD relates [74] the steep increase of the cross section to the rise of the gluon density. However, the normalisation is not predicted correctly [75]. In particular, perturbative QCD states that the cross section is proportional to the square of the gluon density function of the proton, i.e.

$$\sigma \sim [\hat{x}g(\hat{x}, \hat{q}^2)]^2$$

with $\hat{q}^2 = (Q^2 + m^2_{J/\Psi} + |t|)/4$ and $\hat{x} = (Q^2 + m^2_{J/\Psi} + |t|)/W^2$. The mass of the J/Ψ mesons delivers the scale large enough, $\hat{q}^2 \simeq 2.5$ GeV^2, for the perturbative QCD calculations to be valid. The effective pomeron trajectory was determined by both HERA collaborations from the fit to the
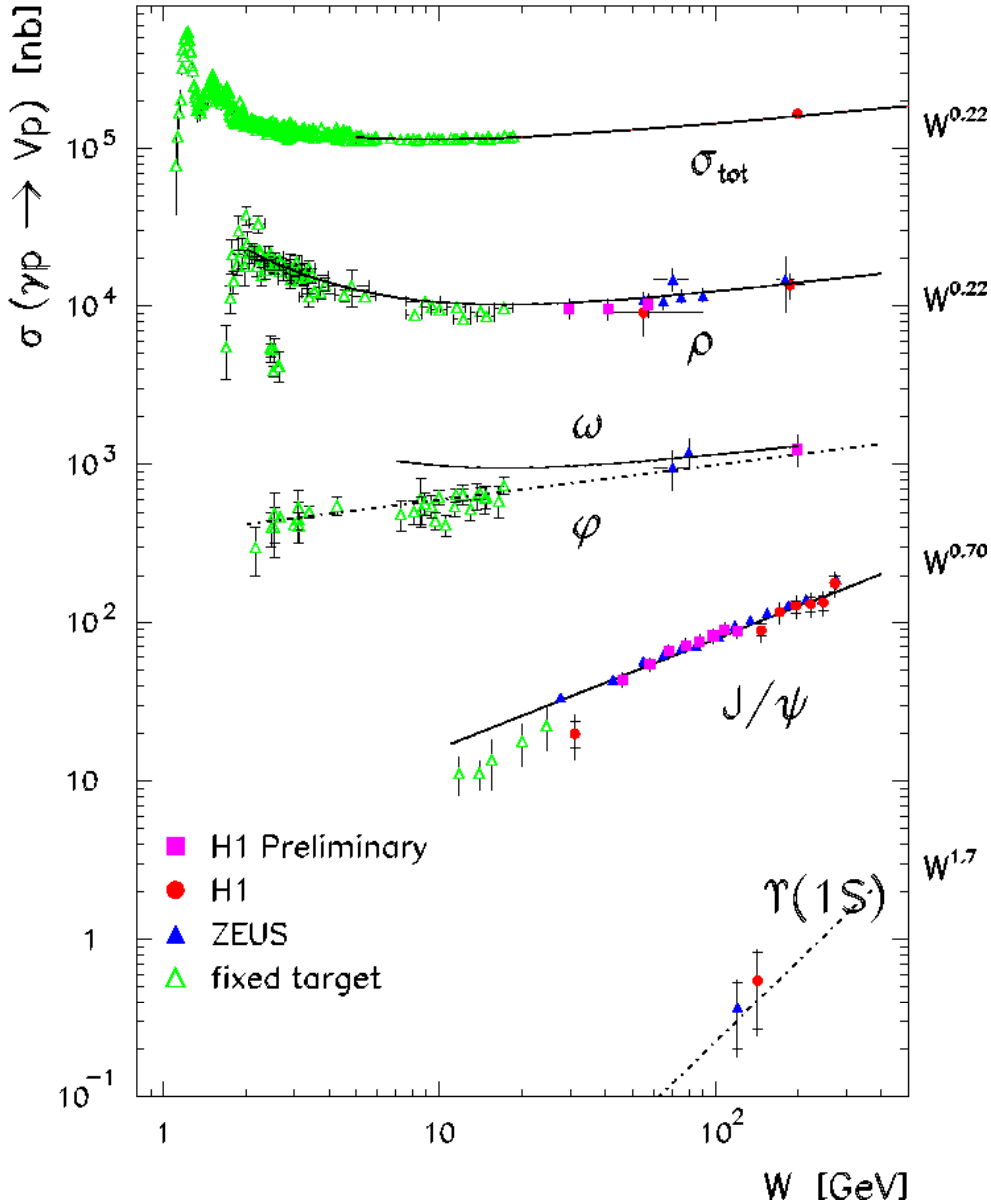
Figure 3.3: The photoproduction cross sections for various vector mesons as a function of W. Lines show W^{δ} dependence with δ values indicated. From [70].

energy dependence of the slope parameter. The fitted pomeron trajectories are compatible within the errors. The H1 Collab. measures [72] $\alpha_{I\!P}(0) = (1.20\pm0.02)$, $\alpha'_{I\!P} = (0.15\pm0.06)$ GeV^{-2} while the ZEUS Collab. [73] finds $\alpha_{I\!P}(0) = (1.200 \pm 0.009)$, $\alpha'_{I\!P} = (0.115 \pm 0.018(stat.)^{+0.008}_{-0.015}(syst.))$ GeV^{-2} in a similar kinematic range. These values are inconsistent with parameters of the soft-pomeron trajectory: $\alpha_{I\!P}(t) = 1.08 + 0.25 \cdot t$ [2].

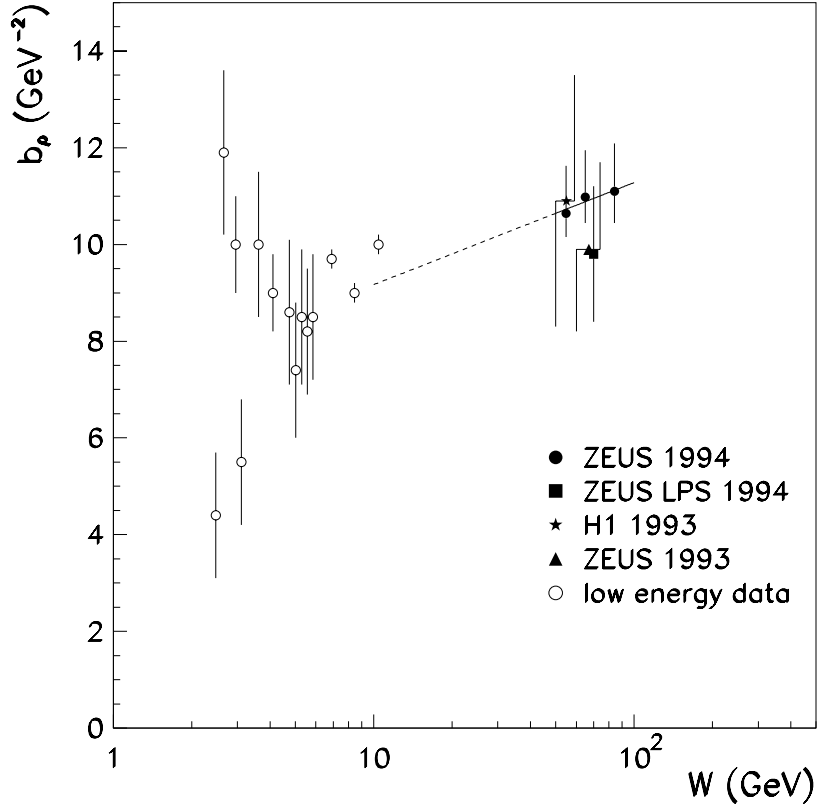The photoproduction of the Υ meson was measured [71, 76] via its decay into the $\mu^{+}\mu^{-}$

Figure 3.4: The slope parameter, b, for the elastic reaction $\gamma p \to \rho p$ in the kinematic region $50 < W < 100$ GeV and $|t| < 0.5$ GeV^2 as a function of W together with the low energy [69] and HERA [64, 67, 68] results. The fit of the energy dependence is indicated with the solid line and its extrapolation to lower energies is marked with the dashed line. From [64].

pair. No distinction for Υ, Υ' and Υ'' was made due to limited experimental resolution. The Υ photoproduction cross section was deducted using known branching ratios. The cross section for elastic Υ photoproduction was found to be small and below 1 nb. It is reasonably well described by the pQCD calculations. These calculations are either based on the leading vector meson cross section including corrections [77] or use the parton–hadron duality hypothesis to obtain the production of Υ from the $b\bar{b}$ cross sections [78].

3.2 Diffractive Scattering

A photon can also dissociate into a multiparticle hadronic state (X) of mass M_X in the process of inclusive diffraction:

$$\gamma p \to X p$$

27

if the coherence condition $M_X^2/W^2 \ll 1$ is satisfied. The inclusive diffractive dissociation was studied [79] by the E-612 experiment at Fermilab in the scattering of real photons off protons in the kinematic range $75 < E_\gamma < 148$ GeV, $0.02 < |t| < 0.1$ GeV^2 and $M_X^2/s < 0.1$. At low mass the cross section is dominated by the ρ production. The t-distribution in the ρ mass region is exponential with the slope $b = 10.6 \pm 1.0$ GeV^{-2}. At larger masses the slope of the t-distribution is roughly half of that for the ρ region. At high values of M_X^2 a dominant $1/M_X^2$ behaviour was observed.

The diffractive events were characterised by the lack of activity between the photon system X and the proton fragmentation region. This feature of the diffractive final state is called Large Rapidity Gap (LRG).

The photon inclusive diffractive dissociation was studied by H1 [80] and ZEUS [81] Collaborations using the LRG signature. Experimentally, the events were selected requiring a pseudorapidity gap between the most forward hadron (with pseudorapidity of η_{max}) and the final state proton. The H1 carried out the measurements at $W = 187$ GeV and $W = 231$ GeV. They found that the energy and M_X^2 dependencies of their and the low energy data [79] are well described by the triple-Regge mechanism. The extracted effective intercept of the pomeron trajectory is $\alpha_{I\!P}(0) = 1.068 \pm 0.016(stat.) \pm 0.022(syst.) \pm 0.041(model)$ and agrees well with the one obtained for the hadron-hadron scattering.

The ZEUS preformed the study of the M_X^2 distribution at $W \approx 200$ GeV and found that for larger masses $(8 < M_X^2 < 24$ GeV$^2)$ the triple-Regge mechanism provides a good description of the data. The effective intercept of the pomeron trajectory was found to be $\alpha_{I\!P}(0) = 1.12 \pm 0.04(stat.) \pm 0.07(syst.)$ which is consistent with H1 findings within the errors. The ZEUS Collab. measured the ratio of the single diffractive photon dissociation to the total cross section to be $(13.3 \pm 0.5(stat.) \pm 3.6(syst.))\%$.

The presence of the LRG events with weak W dependence is typical for diffractive scattering and is interpreted as due to the exchange of the colour-neutral pomeron. This is in contrast to the "usual" DIS events where the hadronic activity is connected to the production of partons in the color field stretched between the proton remnant and the struck quark. One should note that the presence of the LRG events in DIS leads to the partonic interpretation and the measurement of the pomeron partonic structure function. An important conclusion was that a sizable fraction of the pomeron is due to the gluon content.

In photoproduction, the LRG signature is also observed in events with production of jets. The large rapidity gap can be observed between the jets and the target particle as in the Ingelman–Schlein model [82]. In this case the four-momentum transfer is small and the target particle preserves its identity. Bjorken proposed to study events in which the gap separates the jets. In such events the four-momentum transfer is large.

Both ZEUS and H1 analysed events with production of jets and the LRG in the proton fragmentation region [84, 85]. Figure 3.5 shows the η_{max} distribution for such events. A clear excess of data over the non-diffractive Monte Carlo is observed for $\eta_{max} < 2$. The sum of the non-diffractive and diffractive Pythia MC well describes the data. The ZEUS Collab. concludes [84] that the gluon content of the pomeron should be 30-80% to describe the data with the help of the Ingelman–Schlein model.

The measured cross sections for the diffractive dijet photoproduction [86, 87] show a steep fall-off with the jet transverse energy, E_T^{jet}, as expected for the parton–parton scattering. Re-
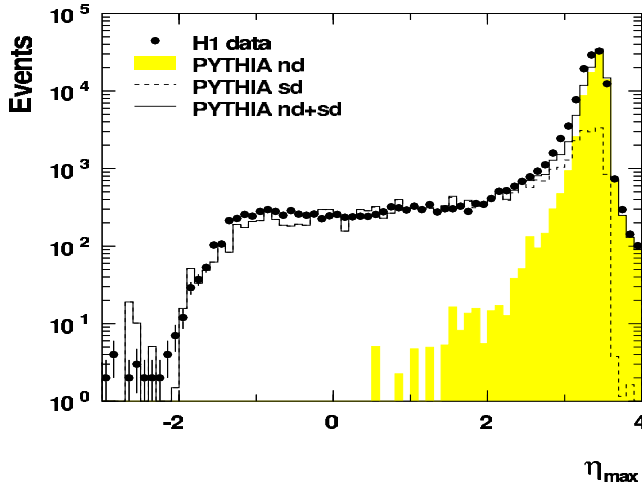
Figure 3.5: The η_{max} distribution for photoproduction events containing jets of $E_T > 5$ GeV and $-1.5 < \eta_{jet} < 2.5$ compared to the Pythia MC predictions. The non-diffractive Pythia is depicted by the shaded histogram, diffractive is marked by the dashed line and the sum of both by the solid line. From [85].

cently, the H1 Collab. published an analysis of the diffractively produced jets in tagged photoproduction [88]. They found that the Monte Carlo prediction, based on the H1 2002 QCD fit, well describes the shapes of the differential cross sections. However, the magnitude is overestimated by a factor of about 1.3. The shape of the differential cross section is well represented if in the Monte Carlo model the pomeron intercept of $\alpha_0 = 1.17$ or $\alpha_0 = 1.08$ is used while the choice of $\alpha_0 = 1.4$ is disfavoured.

Events with a large rapidity gap between the jets were studied by ZEUS [89] and H1 [90] collaborations. Such events can be due to the exchange of a colour singlet object. The exchange of the electroweak boson or strongly interacting colour singlet can lead to similar soft gluon emission patterns [91]. However, their rates can be different. If the jets have large transverse energies then the four-momentum transfer is large and the process can be perturbatively calculated. Bjorken [83] estimated that the ratio of the colour singlet two-gluon exchange to the the single gluon exchange is about 0.1.

The gap fraction, $f(\Delta\eta)$, is defined as a number of dijet events with a certain gap size $\Delta\eta$ to the total number of dijet events for which the distance between the jets is $\Delta\eta$. The ZEUS Collaboration used events with at least two jets of $E_T > 6$ GeV and separated in pseudorapidity by at least two units. The region between the jet cones with no particle of the transverse energy $E_T^{part.} > 250$ MeV is called a gap. The data and MC predictions are compared in Fig. 3.6. A clear excess of the events for large values of $\Delta\eta$ is observed. The gap fraction for the colour singlet is found to be about $0.07 \pm 0.02^{+0.01}_{-0.02}$. It is larger than the values measured at Tevatron ~ 0.01 [92, 93]. H1 used events with at least two jets with $E_T^{j1} > 6$ GeV and $E_T^{j2} > 5$ GeV and separated by at least 2.5 pseudorapidity units. In addition, H1 measures the total activity between the jets as E_T^{gap} which is the sum of the transverse energies observed in the region between two highest E_T jets. For the lowest value of $E_T^{gap} < 0.5$ GeV and $3.5 < \Delta\eta < 4.0$ the gap fraction is approximately 10% in good agreement with the ZEUS result.

The ZEUS Collab. studied the proton-dissociative diffractive production of vector mesons at large momentum transfer [94]. The cross sections for the ρ, ϕ and J/Ψ as a function of t are well described by the pQCD BFKL calculation [95]. The ratio of the differential cross section for ϕ production to that for the ρ production rises with t increasing up to 4 GeV and for higher t values it approaches the SU(4) value (ignoring the mass difference the couplings strengths of
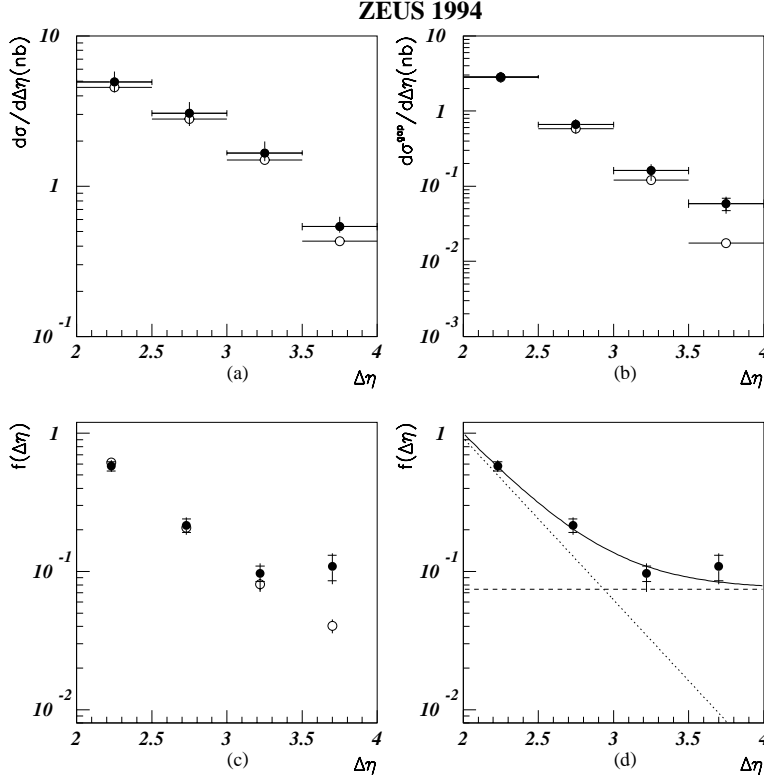
29

ZEUS 1994

Figure 3.6: Inclusive cross sections as a function of the pseudorapidity distance $\Delta\eta$ between the jets (a) and for events with the LRG signature (b). ZEUS data - black circles. The Pythia prediction for non-singlet exchange - open circles. The gap fraction as a function of $\Delta\eta$ is depicted in (c) and in (d) where also the result of the fit (solid line) to a sum of an exponential and a constant (dotted line) is shown. From [89].

the photon to ρ, ω, ϕ and J/Ψ mesons should be as 9:1:2:8). This ratio for $J/\Psi/\rho$ increases with t however it is significantly smaller than the predicted value of 8:9. The effective slope of the pomeron trajectory was found to be consistent with 0, $\alpha'_{I\!P}(0) = -0.02 \pm 0.05(stat.)^{+0.04}_{-0.08}(syst.)$ and $\alpha'_{I\!P}(0) = -0.06 \pm 0.12(stat.)^{+0.05}_{-0.09}(syst.)$ for the ρ and ϕ meson, respectively. These values are in agreement with the pQCD expectations [96] and smaller than $\alpha' = 0.25$ characteristic for soft processes at $-t < 0.5$ GeV^2 and also smaller than those measured for $-t < 1.5$ GeV^2 [97]. The analysis of the angular distributions of the mesons decay products was used to determine the ρ and ϕ spin-density matrix elements [94]. They are r^{04}_{00} and r^{04}_{10} related to the single helicity flip amplitudes and r^{04}_{1-1} related to the double helicity flip amplitudes. The study was performed in the meson rest frame with the quantisation axis taken as the meson direction in the γp cms– the s-channel helicity frame. Following the pQCD predictions and contrary to soft diffractive processes in which the helicity is conserved (SCHC hypothesis), all these matrix elements are significantly different from zero: r^{04}_{00} and $\mathcal{R}e(r^{04}_{10}) \approx 0.05$ and $r^{04}_{1-1} \approx -0.15$ in the whole $|t|$-range considered [94]. These observations are semi-quantitatively reproduced in the BFKL framework [98].

30

3.3 Hard Jets in Photoproduction

The photoproduction of jets at a large scale provided by the jet transverse energy, E_T, can be computed in perturbative QCD. Examples of the leading order QCD diagrams for inclusive jet photoproduction are shown in Fig. 3.7. In LO QCD such processes are divided into two classes. In the first one, the direct process, the photon interacts via the boson-gluon fusion or QCD Compton scattering and acts as a point-like particle with $x_\gamma \approx 1$ where x_γ is the fraction of the photon momentum participating in the scattering. In the second one, called the resolved process, the photon acts as a source of partons and $x_\gamma < 1$. Both classes lead to the production of jets. However, they differ in the jet topology. The resolved events events contain the photon remnant jet (see Fig. 3.7). A review of the theoretical ideas connected to the hard photoproduction can be found in [99].

Jet cross sections are sensitive to the photon and the proton structures and to the dynamics of the hard sub-process. For large E_T values the influence of not so well understood soft processes
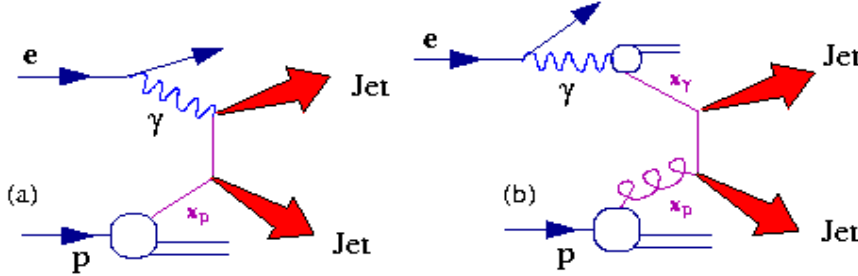

Figure 3.7: Examples of the LO QCD diagrams for inclusive jet photoproduction in direct (a) and resolved (b) processes.

is reduced.

The jet photon–proton cross section, $d\sigma_{\gamma p}$, can be written as

$$d\sigma_{\gamma p} = \sum_{ab} \int_{x_\gamma} \int_{x_p} dx_p dx_\gamma f_p(x_p, \mu^2) f_\gamma(x_\gamma, \mu^2) d\hat{\sigma}_{ab}(x_p, x_\gamma, \mu^2) \cdot (1 + \delta_{hadr})$$

where f_p is the proton parton density function (PDF), f_γ is the photon PDF, $\hat{\sigma}_{ab}$ describes the hard partonic cross section and μ represents both the factorisation and renormalisation scales. The hadronisation correction, δ_{hadr}, takes into account non-perturbative effects. It can be estimated using the Monte Carlo models for the parton cascade and fragmentation. For the direct component the photon PDF is reduced to the Dirac δ-function at $x_\gamma = 1$.

The cross sections for the inclusive jet photoproduction were measured by H1 [101] and ZEUS [102] Collaborations. Figure 3.8 shows the H1 measurement. The LO QCD calculations fail to reproduce the data. The next-to-leading order QCD predictions deliver a good description of
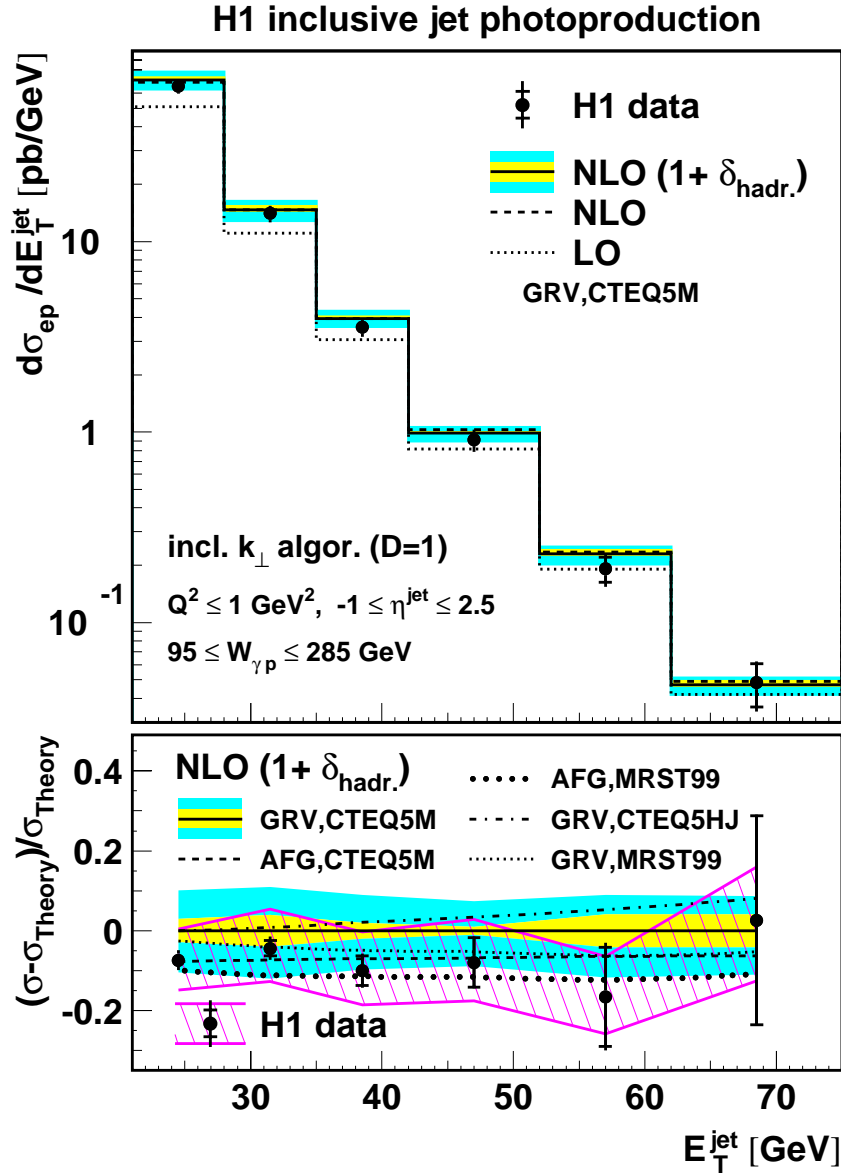
Figure 3.8: Top: differential e^+p cross section for inclusive jet photoproduction as a function of E_T^{jet} compared to LO and NLO QCD calculations using GRV and CTEQ5M PDFs for the photon and proton, respectively. Bottom: relative difference between the data and different NLO calculations. The calorimeter energy scale uncertainty is show as the hatched band. The shaded band depicts the uncertainty on the NLO QCD predictions. From [101].

the measured distribution. The cross section calculated with the GRV [103] photon PDF gives values which are 5-10% larger than those obtained with AFG [104]. Different parameterisations of the proton PDF have a small effect at low values of E_T^{jet}. With increasing jet transverse energy the differences appear when CTEQ5M [105] based calculations are compared to those

obtained with MRST99 [106] or CTEQ5HJ [105].

The ZEUS Collab. measured the scaled invariant cross section, $(E_T^{jet})^4 (E^{jet} d^3\sigma/dp_X^{jet} p_Y^{jet} p_Z^{jet})$ where E_T^{jet} is the jet transverse energy and E^{jet} is the jet energy and p^{jet} is the jet momentum. The measurement was performed for jets with the pseudorapidity $-2 < \eta_{\gamma p}^{jet} < 0$ measured in the photon–proton centre-of-mass frame at the two values of photon–proton centre-of-mass energy $W = 180$ GeV and $W = 255$ GeV. The ratio of the scaled invariant cross sections when plotted as a function of variable $x_T = 2E_T^{jet}/W$ shows the scaling violation. This is depicted in Fig. 3.9.
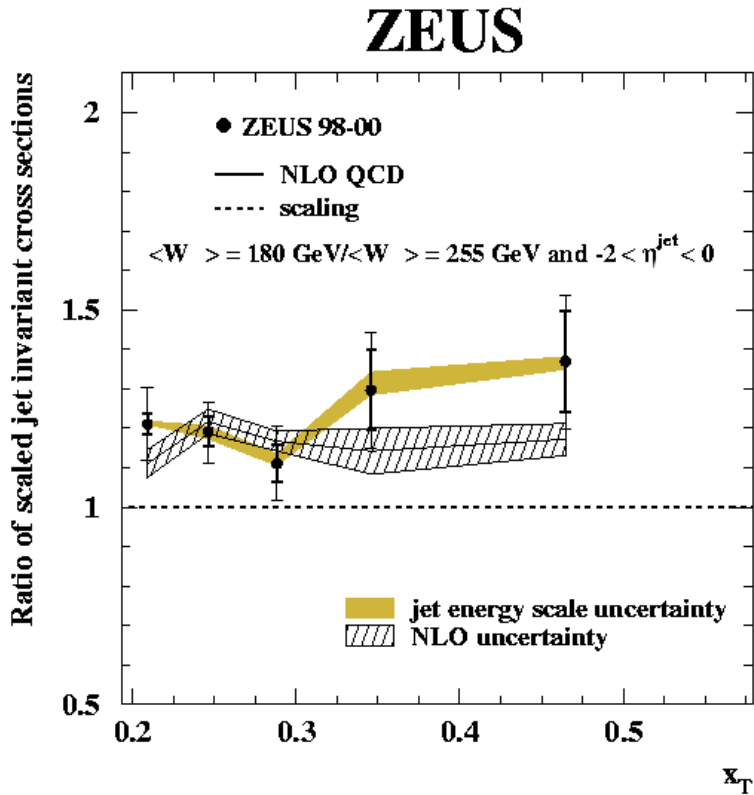

Figure 3.9: Measured ratio of the scaled jet invariant cross sections at two W values as a function of x_T. From [102].

The inclusive jet cross section can be used to determine the strong coupling constant value at the Z boson mass scale, $\alpha_s(M_Z)$. The measured value

$$\alpha_s(M_Z) = 0.1224 \pm 0.0001(stat.)^{+0.0022}_{-0.0019}(exp.)^{+0.0054}_{-0.042}(th.)$$

is consistent with the world average of $\alpha_s(M_Z) = 0.1183 \pm 0.0027$ [107] (see Fig. 3.10a) and the measurements [108, 109] in NC DIS and the $p\bar{p}$ interactions [110]. When plotted as a function of the jet transverse energy α_s shows (see Figs. 3.10b and 3.10c) a clear running behaviour.
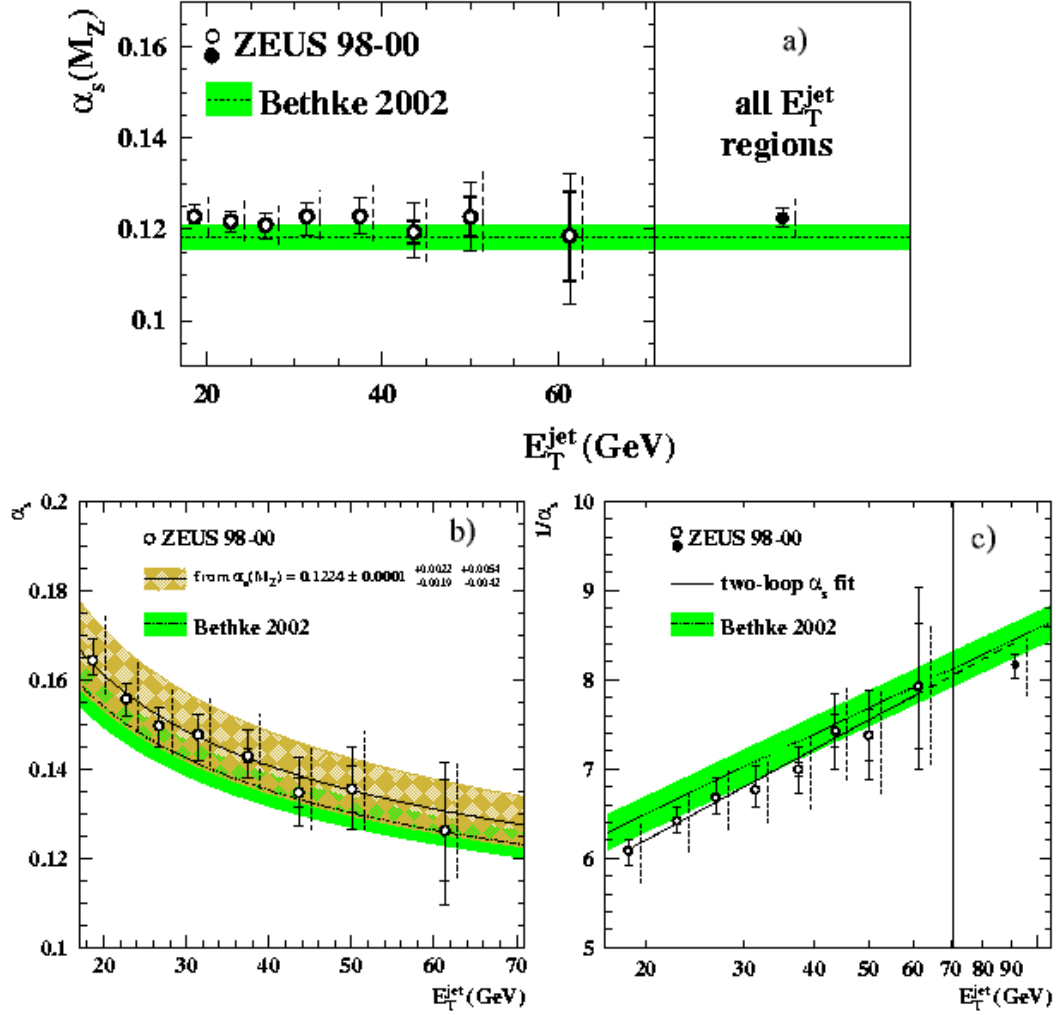
Figure 3.10: (a) The $\alpha_s(M_Z)$ values (open circles) as a function of E_T^{jet}. The combined result using all the E_T^{jet} intervals is shown as a filled circle. (b) The value $\alpha_s(E_T^{jet})$ as a function of E_T^{jet} (open circles). The solid line represents the predictions for the central value of $\alpha_s(M_Z)$ measured by the ZEUS Collab. with the uncertainty given by the light-shaded band. (c) The value $1/\alpha_s(E_T^{jet})$ as a function of E_T^{jet} (open circles). The solid line represents the result of the two-loop α_s fit to the measured values. The dashed line shows the extrapolation to $E_T^{jet} = M_Z$. In all figures the inner error bars show the statistical uncertainty and outer error bars represent the statistical and systematic uncertainties added in quadrature. The dashed error bars show the theoretical uncertainties. The world average (dotted line) and its uncertainty (shaded band) are displayed. From [102].
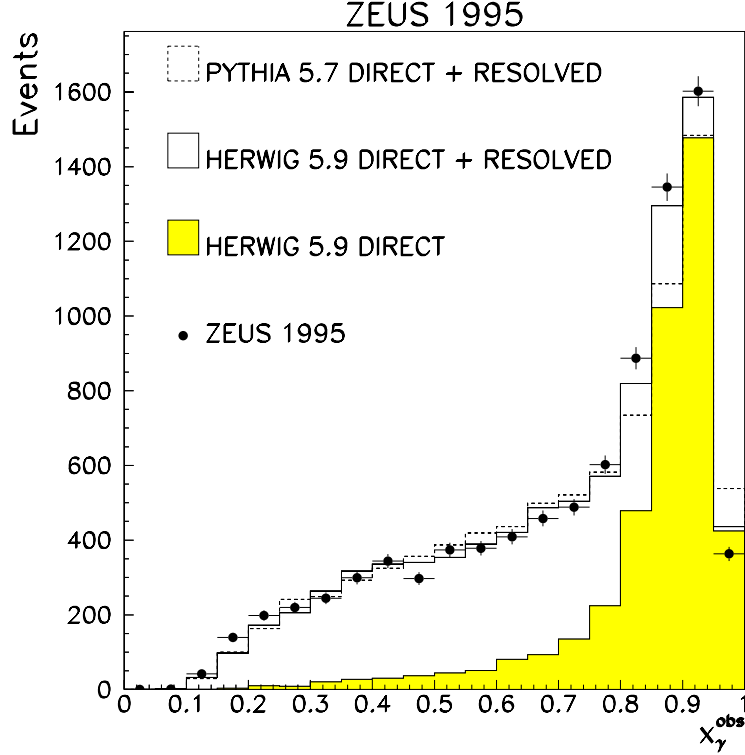
Figure 3.11: The x_γ^{obs} distribution for data [113] compared to MC predictions [140, 141]. The simulated distributions were fitted to the data.

For the dijet photoproduction x_γ is estimated with x_γ^{obs} which measures the fraction of the photon energy participating in the production of the two highest energy jets [111]

$$x_\gamma^{obs} = \frac{E_T^{jet1} e^{-\eta_{jet1}} + E_T^{jet2} e^{-\eta_{jet2}}}{2\, y\, E_e}$$

where $E_T^{jet1,2}$ are the transverse energies of the jets in the laboratory frame, $\eta_{jet1,2}$ are the jets' pseudorapidities and y is the fraction of the incident lepton energy carried by the photon in the proton rest frame. In leading order QCD $x_\gamma = x_\gamma^{obs}$. The distribution of x_γ^{obs} is shown in Fig. 3.11. The resolved component dominates below $x_\gamma^{obs} \approx 0.8$ while above this value the direct processes are more important [112, 113]. The distribution of angle, $\Theta^\star$, between the jets in parton–parton cms can be used to test the dijet photoproduction dynamics. For two-to-two massless parton scattering

$$cos\Theta^\star = \tanh\left(\frac{\eta^{jet1} - \eta^{jet2}}{2}\right).$$

QCD predicts different dijet angular distributions for the resolved and direct components. For the latter, mediated mainly by the quark, the distribution is $d\sigma/d|cos\Theta^\star| \sim (1 - |cos\Theta^\star|)^{-2}$. If the process is mediated by the gluon exchange, like in the case of the resolved component, the distribution is $d\sigma/d|cos\Theta^\star| \sim (1 - |cos\Theta^\star|)^{-1}$. The dijet photoproduction cross sections were measured by both H1 and ZEUS Collaborations [112, 113]. The ZEUS measurement of

$d\sigma/d|cos\Theta^\star|$ is presented in Fig. 3.12.
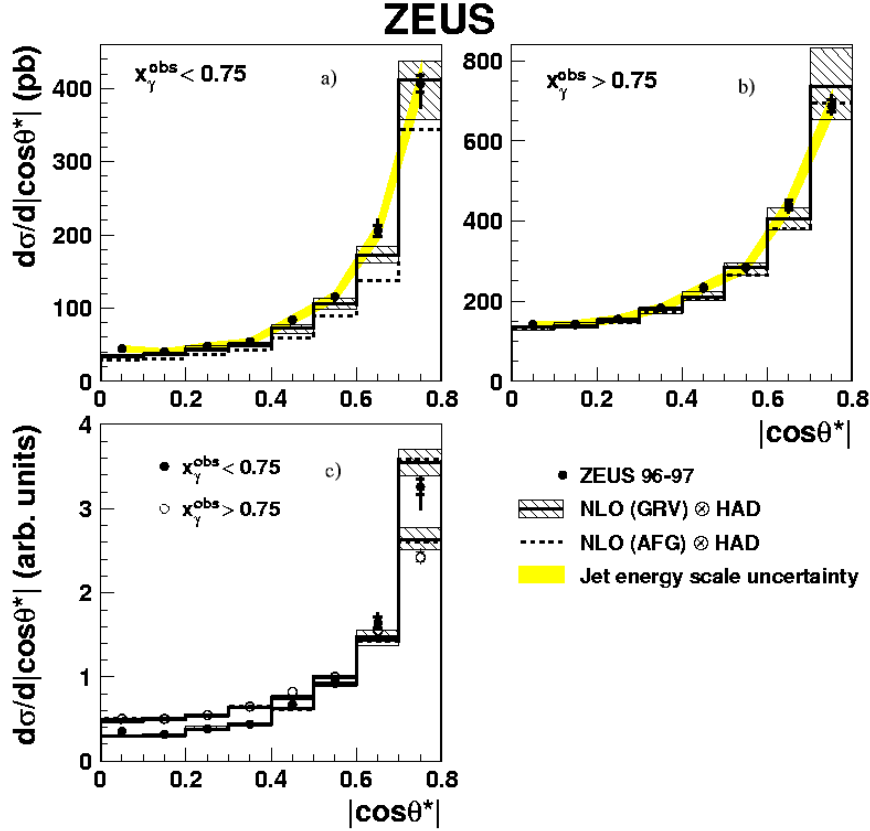

Figure 3.12: Measured cross sections as a function of $|cos\Theta^\star|$ for $x_\gamma^{obs} < 0.75$ (a) and $x_\gamma^{obs} > 0.75$ (b) compared to NLO predictions obtained using GRV-HO and CTEQ5M1 PDFs for the photon and proton respectively. Hatched band represents theoretical uncertainties. Shaded band shows the jet energy uncertainty. Predictions using AFG-HO are depicted as the dashed line. In (c) the cross sections are area normalised and the data for $x_\gamma^{obs} < 0.75$ (solid circles) and for $x_\gamma^{obs} > 0.75$ (open circles) are shown. From [113].

For $x_\gamma^{obs} < 0.75$, the region enriched in the resolved component, the measured cross section lies above the NLO QCD predictions using GRV-HO for the photon PDF. Given the theoretical and experimental uncertainties the NLO QCD calculations [114] reasonably well describe the data. The calculations using AFG-HO are below those that use GRV-HO. For $x_\gamma^{obs} > 0.75$, in the direct region, the NLO QCD predictions are in agreement with measured cross section.

The shapes of the data and the NLO distributions are compared in Fig. 3.12c. For $x_\gamma^{obs} < 0.75$ the data rise more rapidly with $|cos\Theta^\star|$ than those in the direct component dominated region. This is consistent with a difference in the dominant propagators. A similar observation was made in [112].

The agreement between the data and the NLO QCD calculations at high x_γ^{obs} and high transverse energy, where the dependence on the photon structure is small, show a consistency between the data and the gluon distribution in the proton extracted from DIS data. Further discrimination between the photon PDFs is difficult due to large uncertainties in the theory at low transverse energies and both the theoretical and experimental uncertainties at higher transverse energies. Further constraints of the parton densities in the photon can be made more stringent by including the higher-order or re-summed calculations.

Chapter 4

ZEUS $\sigma_{ToT}^{\gamma^\star p}$ Analysis

The measurement of the total cross section for photoproduction is based on the counting of the number of events in which the very low virtuality photon emitted by the positron undergoes the interaction with a proton. The final state hadrons are registered in the central detector and form the "hadronic part" of the trigger. The measurement of the scattered positron is twofold. On one hand it gives the photoproduction event signature and on the other its energy was used to establish the photon energy. The data used for the determination of the total cross section for photoproduction were taken under controlled systematic conditions. In the following the accelerator and the experiment description and the experimental procedure are outlined.

4.1 HERA Accelerator

The HERA (Hadron-Elektron Ring Anlage) [115] at DESY laboratory is a unique storage ring that allows the study the interactions of protons with electrons or positrons. The accelerator was designed in the 80-ties and started its operations in 1992. The system of DESY accelerators is shown in Fig. 4.1. HERA is housed in the underground tunnel of about 6.4 km circumference. Two separate storage rings for leptons and protons are placed in the tunnel. The energy of the lepton beam is 27.5 GeV. (Only at the beginning of the operation leptons had the energy of about 26.6 GeV.) The protons beam energy was 820 GeV and was increased to 920 GeV in 1998.

Four experimental halls are placed on four straight sections of the HERA tunnel. Two main experiments, devoted to the study of the ep interactions, ZEUS and H1 are placed in the South and North halls, respectively. In the East hall the HERMES experiment which uses the longitudinally polarised lepton beam to study the nucleon spin structure is housed. The West hall is occupied by the HERA-B experiment which aims to study the CP symmetry violation in the $B^0\overline{B}^0$ system and the production and rare decays of J/Ψ.

Both HERA beams are structured. They are divided into bunches. Each bunch is stored in one of 220 "buckets". This results in 96 ns crossing time of the beams. In reality only up to 210 buckets are filled. The proton beam is obtained from the H^- source. The protons are accelerated in the liniac and stored in the DESY III storage ring where they are bunched and
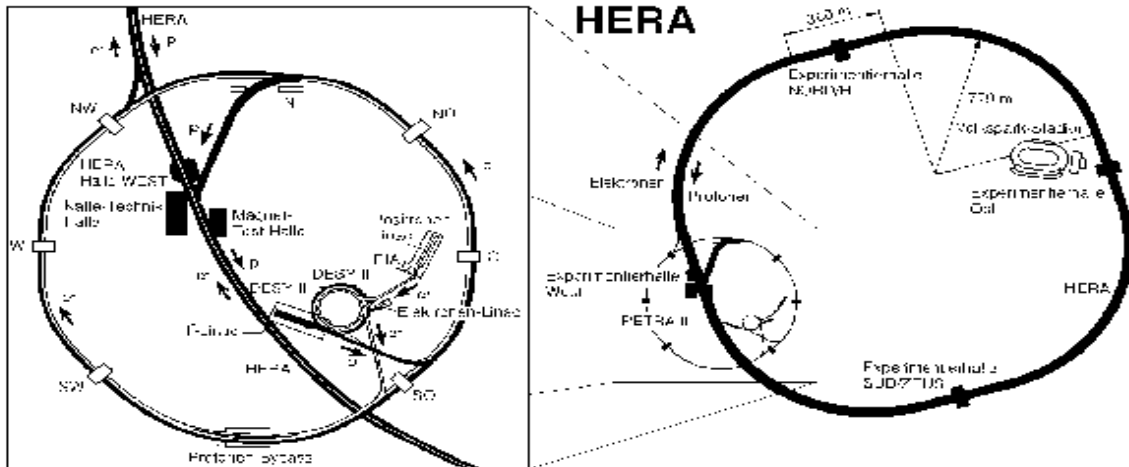
Figure 4.1: Accelerator complex at DESY.

accelerated to 7.5 GeV. Later the bunches are injected into PETRA (Positron-Elektron Tandem Ring Anlage) where the next acceleration step is performed. Later protons of 40 GeV energy are transfered into the HERA proton ring where they are accelerated to the maximum energy. The typical lifetime of the proton beam is a few days.

The electrons (positrons) are accelerated to 250 MeV (450 MeV) in the LINIAC I (LINIAC II). Then they are transfered to the liniac accumulator PIA where a single bunch (about 60 mA) is created. Later this bunch is injected into DESY II and accelerated to 7.5 GeV energy. In PETRA II the beam is restructured into the HERA bunch structure, accelerated to 12 GeV and injected into the HERA lepton ring for final acceleration. The typical life-time of the lepton beam is several hours.

It should be mentioned that the beam structure is such that some bunches collide with "empty" bunches in the other beam. These bunches are called the "pilot bunches" and are used in the studies of the background processes coming from the beam – residual gas interactions.

4.2   ZEUS Detector

The ZEUS detector [116] at HERA was built as a general purpose magnetic detector to study aspects of the *ep* scattering. The detector cross sections (valid for 1992-2000) are shown in Figs. 4.2 and 4.3.   The detector is a hermetic one and covers almost full solid angle with the exception of the area surrounding the interaction beam-pipe.

The detector is built concentrically around the IP. Closest to the beam-pipe was the Vertex Detector (VDX) removed during the 1995 winter shutdown. Next to it a cylindrical drift chamber (CTD) being a heart of the central tracking system is installed. In the forward and backward directions additional tracking detectors are installed: FTD and RTD. The FTD consists of three drift chambers spaced with transition radiation detectors (TRD). The RTD is a single drift
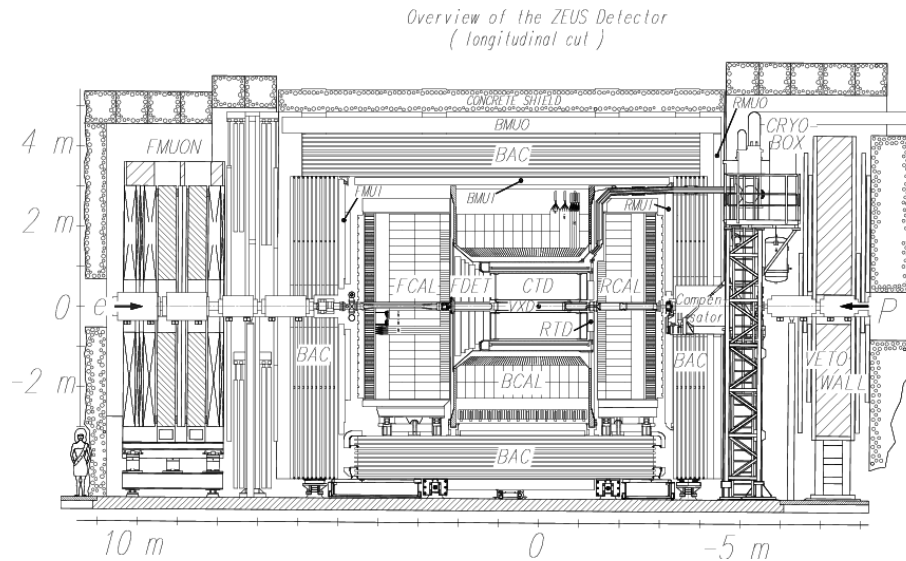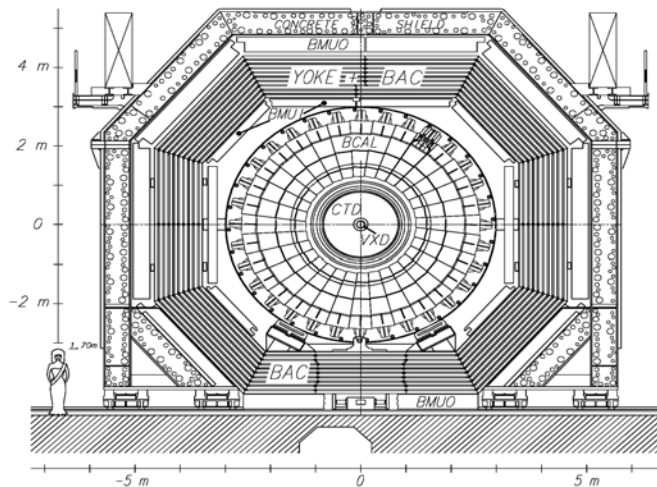
39

Figure 4.2: Side view of the ZEUS detector.

Figure 4.3: The $\mathcal{R} - \phi$ view of the ZEUS detector.

chamber similar to those of the FTD. The tracking system is located inside the superconducting solenoid which delivers an axial magnetic field of 1.43 T. The tracking system provides information on the momentum and directions of produced particles. The TRD and dE/dx measurement within the CTD deliver some means of the particle identification.

The tracking system is surrounded by a high resolution uranium calorimeter (UCAL). This is a basic device to measure the energy of hadrons and leptons. The calorimeter is divided into three parts: the forward (FCAL), the barrel (BCAL) and the rear (RCAL) calorimeter. In front of the FCAL and RCAL the presampler detectors (FPRES and RPRES) made out of single scintillator sheets are mounted. The presamplers are used to distinguish leptons and hadrons. Also a small angle rear tracking detector (SRTD) is installed in front of the RCAL to measure precisely the energy of electrons scattered at small angles.

The UCAL is surrounded by the backing calorimeter (BAC) which is intended to measure the

energy leakage from UCAL. The BAC consists of the iron yoke which provides a return path for the solenoidal field instrumented with proportional chambers. Since muons can traverse both calorimeters the muon chambers were installed. They are divided into forward, barrel and rear section. The muon detectors are positioned outside (FMUO, BMUO and RMUO) and inside (FMUI, BMUI and RMUI) the yoke. A compact beam-pipe calorimeter (BPC) accompanied by the tracking system (BPT) is used to study events with a small momentum transfer between the lepton and the proton.

At z = -7.3 m an iron/scintillator Veto Wall is positioned and is used to discriminate against beam-related background. The proton-remnant tagger (PRT) is installed in the forward direction. The ZEUS detector is also equipped with remote components. These are: the leading proton spectrometer (LPS) at z between 26 and 96 m and the forward neutron counter at z = 106 m. The former consists of six silicon strip detector stations and measures forward scattered protons with transverse momentum $p_t < 1$ GeV. The latter measures energy of the very forward produced neutrons. In the other direction there are two lead/scintillator calorimeters placed at $z = -107$ m and $z = -35$ m which form the Luminosity Monitor (LUMI). Two small electron calorimeters are placed at $z = -8$ m and $z = -44$ m. These parts of the apparatus are used to measure the energy of bremsstrahlung and radiative photons or the energy of electrons produced in photoproduction events.

For the current analysis the most important ZEUS components are the CTD, the UCAL, the Luminosity Monitor and the 35m electron tagger.

4.2.1   Central Tracking Detector

The central-tracking detector [117] provides a high precision measurement of the particle momentum and directions, and delivers information about the event vertex. It measures also the energy loss dE/dx which can be used for particle identification. The CTD is a cylindrical drift chamber. Its active volume is 205 cm long and extends between 18.2 cm and 79.4 cm in radius. It covers the polar angle range of $15^o < \Theta < 164^o$. A schematic view of the CTD octant is depicted in Fig. 4.4. The CTD is a multi-cell super-layer chamber. It has nine super-layers. The wires in even super-layers are tilted by about $\pm 5^o$ w.r.t. to the beam axis and deliver $z - by - stereo$ information. Three super-layers are equipped with the $z - by - timing$ information. The CTD allows a precise reconstruction of the hit position (about 200 μm) in the plane perpendicular to the beam axis. This corresponds to the transverse momentum resolution of:

$$\frac{\Delta p_t}{p_t} = 0.0058 \cdot p_t \oplus 0.0065 \oplus 0.0014/p_t$$

with p_t in GeV. A typical resolution of the interaction vertex position along and transverse to the beam axis are 0.4 and 0.1 cm, respectively.

4.2.2   Uranium Calorimeter

The UCAL [118] is a sampling calorimeter. The 3.3 mm thick absorber plates are made of stainless steel clad depleted uranium and are interleaved with 2.6 mm thick scintillator plates.
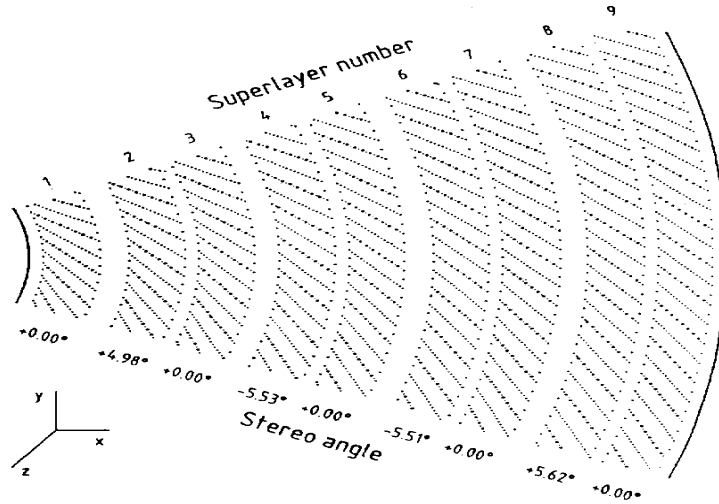
Figure 4.4: A schematic view of the CTD octant.

The calorimeter is the compensating one. It gives equal response to electrons and hadrons (e/h = 1.00±0.02). Under the test conditions the energy resolution was found to be

$$\sigma_E/E = 0.35/\sqrt{E} \oplus 0.02$$

for hadrons and

$$0.18/\sqrt{E} \oplus 0.01$$

for electrons, where E is the incident particle energy in GeV.As was mentioned the UCAL is divided into three parts: FCAL, BCAL and RCAL. They cover polar angle regions (see Fig. 4.5): 2.2^o to 39.9^o, 36.7^o to 129.1^o and 128.1^o to 176.5^o, respectively. The respective angular ranges correspond to the intervals of the pseudorapidity, $\eta = -\log \tan \Theta/2$, of $4 > \eta > 1$ for FCAL, $1.1 > \eta > -0.74$ for BCAL and $-0.72 > \eta > 3.49$ for RCAL.

The calorimeter parts are subdivided into modules which are further subdivided transversally into towers of dimensions 20 by 20 cm^2. The towers are segmented longitudinally into electromagnetic (EMC) and hadronic (HAC) sections. Every EMC section has four 5 by 20 cm^2 cells (two 10 by 20 cm^2 in the RCAL). The cells are read out on two sides by the photomultipliers. The cell energy is a sum of the two channels. Hence it does not depend on the particle entry position into the cell. Moreover, a comparison of the two channels allows a reconstruction of the particle position within the cell. The UCAL modules have non-projective geometry. Only in the barrel region the EMC sections are projective in the polar angle.

The asymmetry of the ep final state is reflected by the calorimeter depth which in case of the FCAL is 7 interaction lengths (λ) while the RCAL is 4 λ deep.

The UCAL timing provides a powerful tool to reject backgrounds at the trigger level.The timing resolution for a single cell is better than $\sigma_t = 1.5/\sqrt{E} \oplus 0.5$ ns if the cell energy is above 3 GeV. Besides its compensating effect, U^{238} natural radiation serves as a valuable source of the calibration and monitoring. The calibration is monitored to a precision better than 0.2%.
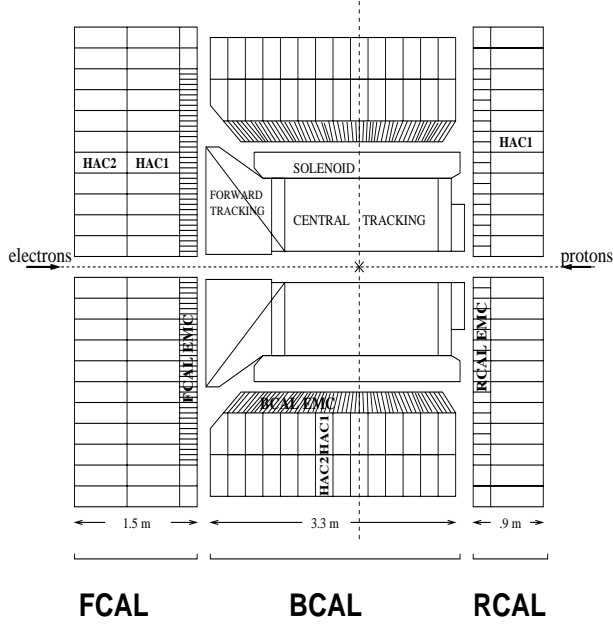
42

Figure 4.5: Side view of the uranium calorimeter.

4.2.3 Luminosity Monitor

The luminosity, $\mathcal{L}$, is one of the crucial parameters of any accelerator. It is defined as by the following relation

$$\mathcal{R} = \sigma \cdot \mathcal{L}$$

where $\mathcal{R}$ is the rate of a chosen process with cross section σ. The luminosity is measured in $cm^{-2}s^{-1}$. A precise determination of the luminosity is an indispensable ingredient for any direct measurement of the cross section. It is clear that the higher the luminosity the larger is the rate of a selected process and hence the smaller are the statistical errors.

In the ZEUS experiment, the HERA luminosity is measured by the rate of the bremsstrahlung photons from the Bethe-Heitler process [119]

$$e + p \rightarrow \gamma e' p.$$

The photons are emitted at small angles. The average angle is $< \Theta_\gamma > = m_e/E \approx 20$ μrad and to a good approximation the photon follows the direction of the initial state lepton. The cross section for this process is well understood and the theoretical predictions give the value to an accuracy of 0.5% [120]. Moreover, it has a very simple signature and its high cross section yields high counting rates.

Neglecting the proton recoil the energy conservation gives:

$$E_\gamma + E_{e'} \approx E_e.$$

In the bremsstrahlung events both the photon and the electron could be measured in the electromagnetic calorimeters [121] if their emission angles were $\Theta_\gamma \leq 0.5$ mrad and $\Theta_{e'} \leq 6$ mrad,
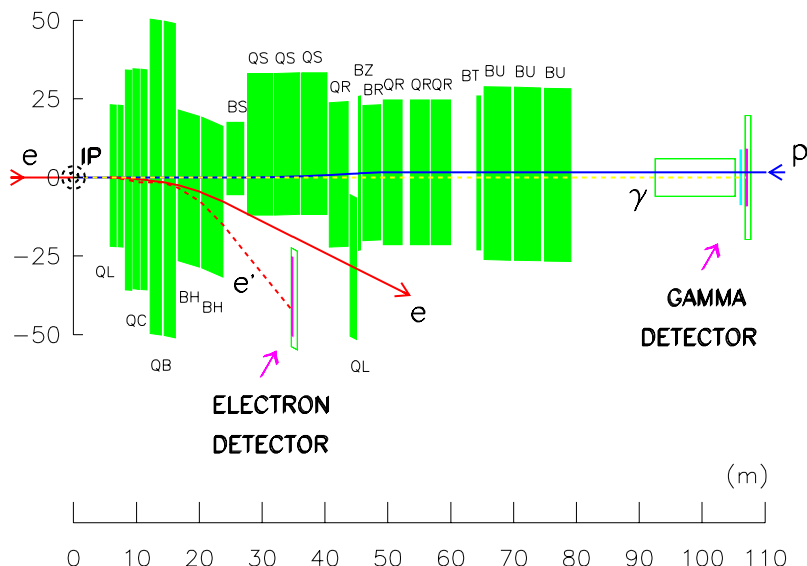
Figure 4.6: Diagram showing the 35m tagger and LUMI photon detector in the beam-line. The boxes labeled Q are quadrupole magnets, and the boxes labeled B are bending (dipole) magnets.

respectively (see Fig. 4.6). A coincidence measurement of the photon and electron energies was used for the luminosity measurement at ZEUS at the very beginning of the running period (H1 used coincidences all the time). Later the luminosity measurement was based on the measurement of the bremsstrahlung photon energy. This was possible because the photon calorimeter acceptance was very high ($\approx 97\%$) and the photon energy independent.

Experimentally, the luminosity is calculated as:

$$\mathcal{L} = \frac{R^{ep}}{\sigma^{obs}}$$

where R^{ep} is the rate of the BH events and the σ^{obs} the *observed* cross section i.e the cross section calculated for the requested range of the photon energies and corrected for the photon calorimeter acceptance, $\mathcal{A}_\gamma$. The bremsstrahlung photon acceptance is calculated using Monte Carlo methods. The calculation takes into account geometrical properties of the electron beam: the angular spread and its tilts at the IP, the geometrical description of the beam-pipe traversed by photons and the detailed description of the photon measuring device. Also the correction due to the small transverse size of the beams – the beam size effect [122] is taken into account. The rate of the BH events, R^{ep}, is corrected for the effect of the event pile-up and for the background beam-gas bremsstrahlung. The latter is removed using the measured rate of the beam-gas interactions from the electron pilot bunches. To minimize the systematic effects due to the photon energy measurement the luminosity was measured for different intervals of the photon energy. A typical accuracy of the luminosity measurement was about 1%.

The bremsstrahlung photons emitted at $\Theta_\gamma < 0.5$ mrad exit the proton beam-pipe through a copper-beryllium window at $z = -92.5$m. After passing the carbon filter (2 - 2.5 X_0) they are registered in the lead/scintillator sandwich calorimeter [121] placed at $z = -107$m. The calorimeter is 22 radiation lengths (X_0) deep. Its energy resolution is $0.19/\sqrt{E(GeV)}$ under the

44

test-beam conditions. A carbon filter shields the detector against synchrotron radiation but also deteriorates the energy resolution to about $0.23/\sqrt{E(GeV)}$. At the depth of 7 X_0 a position detector is mounted inside the calorimeter. It consists of the horizontally and vertically positioned scintillators - "fingers". The position detector provides means of the incoming photon position reconstruction with the resolution of about 0.3 cm in both x and y.

The photon detector can be used for the tagging of the initial-state-radiation (ISR) photons and can also serve as the lepton beam diagnostic tool measuring the lepton beam tilts and angular spreads at the IP. This feature was extensively used in the following analysis.

The construction, the maintenance and running of the luminosity detector is a responsibility of the ZEUS Cracow Group. The author took an active part in this work.

4.2.4   35m Electron Tagger

The 35m electron tagger is used to detect electrons with energies between 5 and 22 GeV scattered at angles smaller than about 6 mrad. Such electrons are deflected gradually in the HERA magnets and leave the beam-pipe at $z = -27$m through a steel exit window. Later they are registered in the calorimeter located at $z = -35$ m. This detector is a 23 radiation lengths deep lead/scintillator calorimeter with resolution of about $0.20/\sqrt{E(GeV)}$. It is also equipped with a position detector placed at the depth of 7 X_0 inside the calorimeter. This position detector has a construction and resolution similar to the one mounted in the photon calorimeter.

Additional calorimeters placed at $z = -8$m and $z = -44$m allow the measurement of electrons scattered at different energies. Thus they extend the kinematic range for tagging the photoproduction events.

4.2.5   Trigger and DAQ

The HERA bunch separation time is 96 ns which corresponds to a rate of 10.4 MHz. The total rate is dominated by the proton - residual gas interactions with a rate of 10 - 100 kHz. Other sources of background are the beam halo, the synchrotron radiation, the electron - gas and the cosmic rays interactions. An efficient trigger is needed to filter out interesting events coming with a rate of only a few Hz.

ZEUS has a three-level triggering system [123]. Fig. 4.7 shows a schematic view of the ZEUS trigger and the data acquisition system. To avoid the dead-time problems the ZEUS components' read out and the first-level-trigger (FLT) are pipelined. Each component has its own, local FLT which takes 25 bunch crossings to analyse the data. The decision is based on global properties of an event. The local decisions are sent to the global-first-level-trigger (GFLT) where they are compiled. In case of a positive decision the component data are read out and processed further. The GFLT reduces the rate to below 1 kHz.

The second-level-trigger (SLT) is a software trigger run on a network of transputers. The global-second-level-trigger (GSLT) combines the components' SLT information and issues the final decision. It reduces the rate to below 100 Hz and mainly rejects background events by means of the energy deposits and timing information from the UCAL. Once an event is accepted by the GSLT the components' data are sent to the Eventbuilder (EVB) to combine them into a single
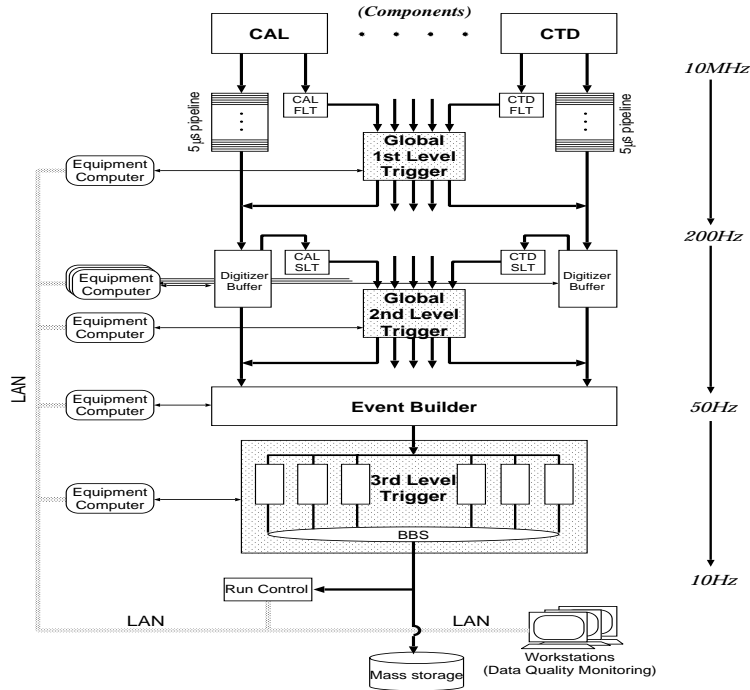
Figure 4.7: The scheme of the ZEUS trigger and data acquisition system.

event. The EVB passes events to the third-level-trigger (TLT). The TLT is a software trigger running on a processor farm. It uses a part of the off-line reconstruction code to extract events that pass physics requirements and reduces the rate below a few Hz. Accepted events are stored on "tape".

4.2.6 Event Reconstruction

Raw data stored by the TLT are passed to the reconstruction chain. The event reconstruction transforms them into useful, physical quantities. The reconstruction is performed for each ZEUS component separately and uses a detailed information about a given component behaviour and the raw data calibration method. Obviously responses of different ZEUS sub-detectors are also correlated which gives better understanding of an event. At the final stage of the reconstruction a Mini Data Summary Tape (MDST) is created. It contains events that passed additional quality requirements. These requirements were the check on the working conditions of the crucial, for the data taking, ZEUS components.

The events stored on the MDST are subsequently used in the physics analyses. It is worth noting that both the reconstruction and analysis chains are the same for the real and the Monte Carlo simulated data.

4.3 Experimental Methods of $\sigma_{tot}^{\gamma p}$ Measurement

Early experiments on the photon–nucleon and photon–nucleus interactions concentrated on the Compton scattering at low, typically hundreds of MeV, photon energies. In the fifties and sixties the photon beam energy was considerably increased and reached a few GeV. For a review of results see [26].

The total cross section for photoproduction was measured in interactions of real photons with nucleons for the incident photon energies between 0.275 and 180 GeV. The measurement is difficult since the electromagnetic interactions consist a majority of the cross section. For the photon energies above about 1 MeV the electron–positron pair creation is by far the largest part of the total cross section. This large background makes virtually impossible to use the attenuation method of the cross section measurement. The way out is to use a tagged photon beam together with a geometrical method to separate hadronic and electromagnetic components.

The photon beam is produced via the Bethe-Heitler process. Usually, a mono-energetic electron or positron beam passes a thin radiator. A photon produced in the bremsstrahlung process follows the lepton direction towards the target and the measuring device. The scattered lepton is deflected in a dipole magnetic field and then reaches a system of counters which registers both the lepton energy and its position. This information is used to calculated the photon energy. The above method implies that the radiator thickness is a compromise between the rate of bremsstrahlung photons and the background events as for example double bremsstrahlungs. Usually, a veto system is placed in the radiator vicinity to reject these backgrounds. An important ingredient is a "clean" primary lepton beam i.e. without the halo and the low energy components.

An example of the experimental apparatus used in [125] is shown in Figs. 4.8 and 4.9. The photon tagging system is depicted in Fig. 4.8. A weak electron beam bombards the radiator R where the bremsstrahlung process takes place. The photon tagging is achieved by the tagging of the electron from the bremsstrahlung process in one of the 64 electron counters E joined in groups of four, with the backing counter B. The electrons are deflected in the magnetic field of the magnet M. In Fig. 4.9 a schematic view of the detection system is presented. The photon beam enters from the right through the collimator, the veto counter V_1 and interacts in the liquid hydrogen target T. The hadronic interaction products are registered in the scintillator box S_1 and the π^0 in S'. The lead converters are marked with L and L'. Forward-going electromagnetic events are rejected by the shower counter V_1 and electron counters C.

The geometrical method relies on two facts. On one hand, the electromagnetically produced pair of leptons is confined to a tiny angular cone ($\Theta \sim m_e/E$). On the other hand, the hadrons produced in the photon–nucleon interaction have a broad angular distribution. This leads to a simple solution for the experimental apparatus. Namely, the hadronic counter with a hole is largely insensitive to the lepton pair creation events. A total absorption shower counter placed at zero angle with respect to the photon beam is applied. It is used to check whether the incident photon energy disappeared from the beam. Such a check uses the fact that the counter gives an equal response to a photon and to a lepton pair. In addition the counter is used to veto the pair production events in which the energy sharing between the leptons is very asymmetric. The low energy lepton can be produced at a large angle and can be mistaken with a hadron.
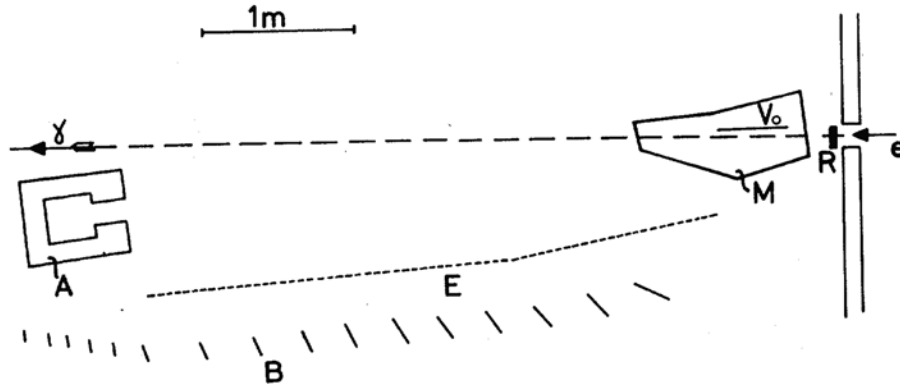
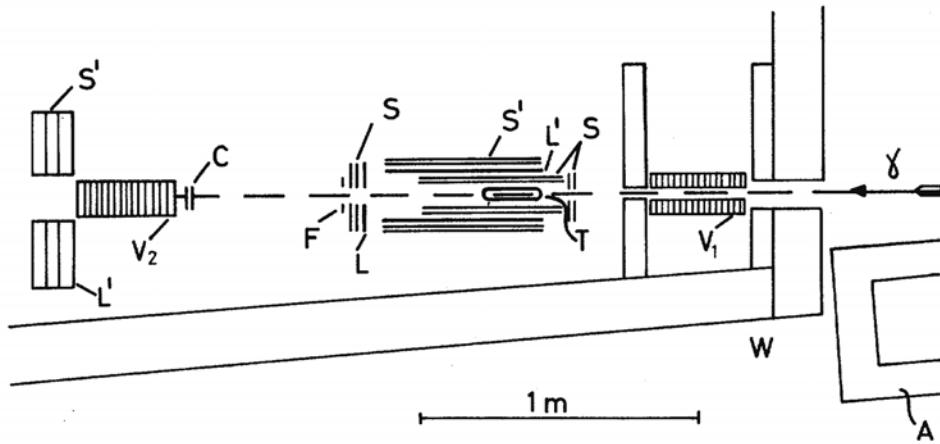Figure 4.8: The photon beam tagging system. From [125].

Figure 4.9: Schematic view of the detection system. From [125].

Its partner which takes most of the energy is produced in the forward direction and reaches the total absorption counter giving a "beam event" signature.

There exist two other methods to produce a monochromatic beam of photons. In one the photons are produced by a positron annihilation. The layout of the bubble chamber experiment [126] applying this method of the beam creation is shown in Fig. 4.10. In the second method a monochromatic beam is produced by the backward Compton scattering of laser light off a high-energy electron beam. The resulting photon spectrum [127] is related to the Compton cross section and depends on the laser photon–electron centre-of-mass energy, $s_{\gamma e}$, through the parameter $X = s_{\gamma e}/(m_e^2 - 1)$ (m_e is the electron mass). If the value of $X \approx 4.83$ [128] then the photon spectrum is peaked close to the kinematic limit so an almost monochromatic photon beam is delivered. The experimental setup using the laser light backscattering to produce an intense photon beam is shown in Fig. 4.11. The photoproduction events were observed in the

48
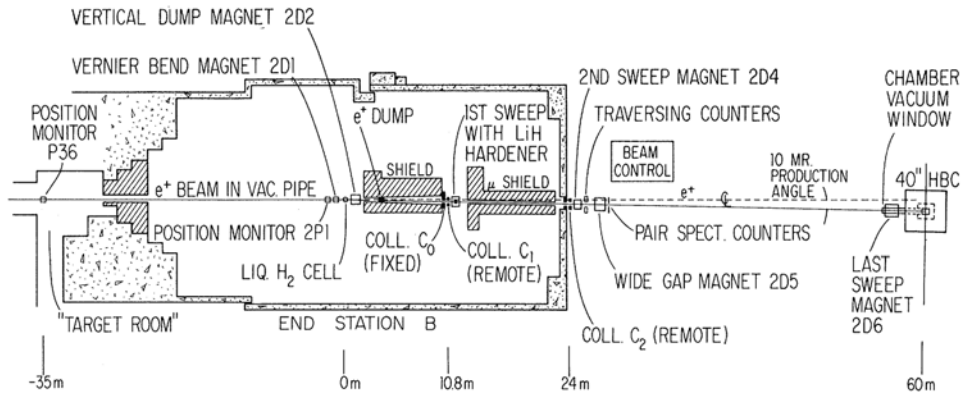
Figure 4.10: Schematic view of the positron annihilation beam layout. From [126].

SLAC hydrogen bubble chamber. A similar setup was used in the photoproduction study in [130, 131].

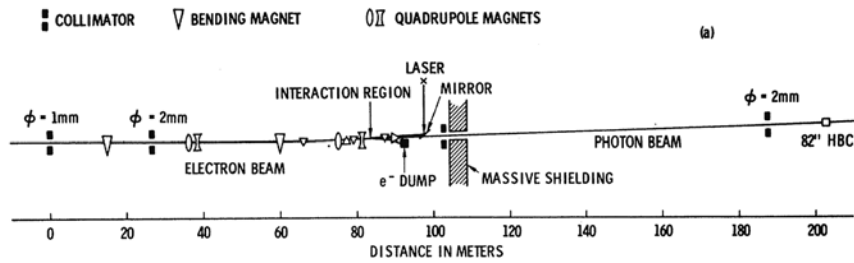Figure 4.11: Schematic view of the apparatus used by the SLAC experiment. The photon beam was produced via the backscattering of the laser light off the electron beam. From [129].

4.4   Comparison of Fixed Target and Storage Ring Methods

The photoproduction measurement in fixed target experiments was performed with real photons in the following manner:

- photon beam creation,
- photon energy tagging,

- registration of the hadronic interaction,

- registration of the pair creation events.

As was mentioned earlier the photon beam was created in one of the three methods:

- bremsstrahlung process of electrons in a thin radiator,

- backscattering of the laser light off the electron beam,

- electron – positron annihilation.

The last two methods gave a monochromatic photon beam. In the first one the photon energy was deducted from the measurement of the electron. This measurement was performed with the help of the magnetic (typically dipole) field and a system of counters - the hodoscope. A system of veto counters was used to reject events with early conversions or due to low energy photons.

The hadronic system was registered in the calorimeter or a bubble chamber using properties of its angular distribution. In the case of a calorimetric measurement a special, dedicated calorimeter was used to register e^+e^--pair creation events. The measurement of pair conversion events was used to calculate the total cross section for photoproduction. Typically, the agreement between the reconstructed and calculated bremsstrahlung spectra (the incident photon spectrum) was found to be within 1%.

Details of the storage ring measurement of the total cross section for photoproduction will be given later. Here only the main points will be outlined.
In the storage ring experiment as at HERA one deals with the interactions of electrons and protons coming from two colliding bunches. So, in principle, one measures the electron–proton cross section which has to be converted into the photon–proton cross section.
Creation of an intense beam of real photons as in the fixed target experiments is impossible. A radiator placed in the vicinity of the interaction point would be an obstacle for the protons [1] leading to a large rate of unwanted proton–nucleus events. On the other hand even if such a photon beam were created then one would need to bring it to an interaction with a proton. This would make the machine design very difficult if possible at all. The problem can be overcome by using the electron beam as a source of almost real photons i.e. photons with small virtuality. Obviously, one has to perform an extrapolation of the measured cross section from a small $Q^2 \neq 0$ down to the photoproduction limit, $Q^2 = 0$.
In principle two measurement methods are possible. In the first one the electron scattered at very small angles is registered in the electron tagging system placed downstream the accelerator beam-pipe at a large distance from the interaction point (IP). Hence, this method is called the electron tag method. In this case the photon is nearly real and its energy can be inferred from the measurement of the scattered electron energy. The extrapolation of the measurement is performed over a limited Q^2 interval. This method was used to obtain the result presented in the following. In the second method, it is required that the scattered electron is not "visible" in the central detector. This means that the limiting Q^2 value is defined by the size of the central

---

[1]One should be aware that the gaseous or thin inner targets are used quite often in specific applications. This leads to the smaller centre-of-mass system energies accessible and requires a dedicated apparatus.

detector opening in the electron beam direction. It is much larger than in the first method hence the extrapolation is much more important and difficult. Such selection is called the "untagged" method. In the ZEUS experiment environment the first method limits the Q^2 to values of the order of 0.01 GeV^2 while for the untagged method events with Q^2 reaching up to ≈ 3 GeV^2 can be observed.

In the first approximation the magnetic field of a storage ring can be treated as a dipole field. Its role is analogous to the role of the magnetic field in the fixed target experiment. The scattered electron is deflected in the magnetic field of the accelerator and eventually leaves the beam-pipe. In the HERA case also the quadrupole magnets are used for the electron beam "bending". This makes the tracking of the scattered electrons through the magnetic structures of HERA difficult and is one of the sources of systematic effects. For practical reasons the electron registration can be performed in localised places along the beam-pipe and hence the scattered electron inelasticity range is limited. Such a place is a compromise between the device acceptance and the accelerator structure.

One should also note that in the beam steering the transverse representation is used. This means that in the actual case it is a closed orbit which matters. This leads to another source of the systematic effects which is the interaction vertex location.

The HERA luminosity was measured via the rate of the bremsstrahlung events registered by a dedicated photon counter placed downstream the electron beam-pipe.

The trigger required an electron tag and the hadronic energy deposit in the main calorimeter.

The lepton pair creation does not constitute an important source of the background since the pairs are produced predominantly in the lepton beam direction and are restricted to a small angular region so they escape the registration via the central detector opening. These leptons are later extracted from the beam by the machine magnets as the off-beam momentum particles. This is a sort of an "automatic" realisation of the hadronic calorimeter beam hole idea used in the fixed target experimental setup and hence the geometric separation of events belonging to the hadronic or electromagnetic final states. In case of the asymmetric energy division within the pair one of the leptons is identified via its energy deposit in the electromagnetic part of the central detector or the measurement in the tracking detector.

Summarising, the use of the beam of virtual photons in the storage ring measurement is the main feature which is different from the fixed target measurement. The similarities are:

- the use of the magnetic field for the scattered lepton deflection,

- the scattered lepton measurement – the interacting photon energy determination,

- the normalisation is obtained via the luminosity measurement or the lepton pair creation events counting,

- a geometric separation of the electromagnetic and hadronic final states,

- the trigger requires both the electron tag and the hadronic energy deposit in the calorimeter.

4.5 From e^+p to γp Cross Section

The equivalent photon approximation relates the ep cross section to the cross sections for interactions between the proton and the longitudinally and transversely polarised photons as

$$\frac{d^2\sigma_{tot}^{ep}(y,Q^2)}{dy\,dQ^2} = \frac{\alpha}{2\pi}\frac{1}{Q^2}\left[\left(\frac{1+(1-y)^2}{y} - \frac{2(1-y)}{y}\frac{Q_{min}^2}{Q^2}\right)\cdot\sigma_T^{\gamma^\star p}(y,Q^2)\right.$$
$$\left. + \frac{2(1-y)}{y}\cdot\sigma_L^{\gamma^\star p}(y,Q^2)\right]. \qquad (4.1)$$

In the photoproduction limit $Q^2 \to 0$

$$\lim_{Q^2\to 0}\sigma_T^{\gamma^\star p} = \sigma^{\gamma p}(W)$$

and

$$\lim_{Q^2\to 0}\sigma_L^{\gamma^\star p} = 0.$$

In the present measurement tagged photoproduction events were used. This means that the scattered lepton was measured in the 35m tagger (see sec. 4.2.4). Due to limited tagger acceptance the measurement was performed over a small range of the photon virtuality $Q_{min.}^2 < Q^2 < Q_{max.}^2$. The $Q_{max.}^2$ is of the order of 0.01 GeV^2 (see sec. 4.11) while $Q_{min.}^2$ is of the order of the electron mass squared. Therefore to obtain the value of $\sigma_{TOT}^{\gamma p}$ one should extrapolate $\sigma_T^{\gamma^\star p}$ to $Q^2 = 0$. Since Q^2 is not directly measured then experimental extrapolation is not possible. The correction can be estimated as in [132].

The Taylor expansion of the cross sections up to linear terms in Q^2 gives

$$\sigma_T^{\gamma^\star p}(y,Q^2) = \sigma_T^0 + \sigma_T^1\cdot Q^2$$

and

$$\sigma_L^{\gamma^\star p}(y,Q^2) = \sigma_L^1\cdot Q^2$$

where σ_T^0 is the total cross section for photoproduction $\sigma_T^0 = \sigma_T^{\gamma^\star p}(y,Q^2=0) = \sigma_{TOT}^{\gamma p}(y)$, σ_T^1 and σ_L^1 are derivatives and $\sigma_T^1 = d\sigma_T^{\gamma^\star p}/dQ^2(y,Q^2=0)$ and $\sigma_L^1 = d\sigma_L^{\gamma^\star p}/dQ^2(y,Q^2=0)$. Integration of Eqn. 4.1 from Q_{min}^2 to Q_{max}^2 after substituting the above relations gives

$$\frac{d\sigma_{tot}^{ep}(y)}{dy} = \frac{\alpha}{2\pi}\left[\left(\frac{1+(1-y)^2}{y}\ln\frac{Q_{max}^2}{Q_{min}^2} - \frac{2(1-y)}{y}\right)\cdot\sigma_T^0\right.$$
$$+ \frac{1+(1-y)^2}{y}Q_{max}^2\cdot\sigma_T^1$$
$$\left. + \frac{2(1-y)}{y}Q_{max}^2\cdot\sigma_L^1\right] \qquad (4.2)$$

if the terms proportional to $Q_{min}^2 \approx m_e^2 \ll Q_{max}^2$ are neglected. Denoting the contributions to the ep cross section due to σ_T^0, σ_T^1 and σ_L^1 as $\sigma_{ep}^{T,0}$, $\sigma_{ep}^{T,1}$ and $\sigma_{ep}^{L,1}$, respectively, the relative contributions can be approximated by:

$$\frac{\sigma_{ep}^{T,0}}{\sigma_{ep}^{T,1}} = \frac{1}{Q_{min}^2}\ln\frac{Q_{max}^2}{Q_{min}^2}\frac{\sigma_T^0}{\sigma_T^1}$$

and

$$\frac{\sigma_{ep}^{L,1}}{\sigma_{ep}^{T,1}} \approx \frac{\sigma_L^1}{\sigma_T^1}$$

which gives

$$\frac{\sigma_{ep}^{T,1} + \sigma_{ep}^{L,1}}{\sigma_{ep}^{T,0}} \approx 0.001 \frac{\sigma_T^1 + \sigma_L^1}{\sigma_T^0} \tag{4.3}$$

when Q_{min}^2 and Q_{max}^2 are substituted with m_e^2 and 0.01 GeV^2, respectively.

Using Eqns. 2.5 and 2.6 and the ρ dominance [26] the right hand side of formula 4.3 takes the form

$$\frac{\sigma_T^1 + \sigma_L^1}{\sigma_T^0} \approx \frac{-\frac{2\sigma_\rho}{m_\rho^2} + \frac{\xi\sigma_\rho}{m_\rho^2}}{\sigma_\rho}.$$

Thus assuming $\xi = 1$ the Eqn. 4.3 leads to the following numerical result

$$\frac{\sigma_{ep}^{T,1} + \sigma_{ep}^{L,1}}{\sigma_{ep}^{T,0}} \approx -0.002.$$

The correction is very small and can be neglected. A similar numerical result was obtained in [133] on grounds of the GVD.

Neglecting then the Q^2 dependence of $\sigma_T^{\gamma^\star p}$ and the longitudinal component the integration of Eqn. 4.1 in the allowed Q^2 range gives

$$\frac{d\sigma_{tot}^{ep}(y)}{dy} = \frac{\alpha}{2\pi} \left[\frac{1 + (1-y)^2}{y} \ln \frac{Q_{\max}^2}{Q_{\min}^2} - \frac{2(1-y)}{y} \left(1 - \frac{Q_{\min}^2}{Q_{\max}^2} \right) \right] \sigma_{TOT}^{\gamma p}(y) \tag{4.4}$$

$$\frac{d\sigma_{tot}^{ep}(y)}{dy} = F_\gamma(y)\sigma_{TOT}^{\gamma p}(y) \tag{4.5}$$

$$\sigma_{TOT}^{ep} = \int_{y_1}^{y_2} F_\gamma(y)\sigma_{TOT}^{\gamma p}(y)\, dy = f_\gamma \sigma_{TOT}^{\gamma p}$$

The term f_γ is referred to as the photon flux factor, and has been determined by numerical integration of F_γ over y. Note that the y-dependence of $Q_{\min}^2$ has been taken into account in the calculation.

From the experimental point of view the measurement of the total γp cross section involves counting of the number of events measured, N, by the detector. The events are collected during the measuring period in which the integrated luminosity, $\mathcal{L}$, was collected. The ratio of the number of events to the integrated luminosity yields the single differential cross section which later divided by the photon flux gives the total cross section. Since the data are taken with an apparatus of finite resolution and angular coverage then the cross section has to be corrected for the detector acceptance $\mathcal{A}(y)$. One can write the total γp cross section as

$$\sigma_{TOT}^{\gamma p} = \frac{\mathcal{N}}{\mathcal{L}} \frac{1}{f_\gamma} \frac{1}{\mathcal{A}(y)}$$

In the present measurement the detector acceptance depends on the acceptance of two devices the 35m tagger which measured scattered positrons and that of the UCAL used for the hadronic

final state measurement. These acceptances are assumed to be independent. Moreover, the experimental apparatus registered events of a special, pre-defined type. Hence, the cross sections has to be corrected for the finite trigger efficiency, Δ_{trig}. In the HERA environment the bremsstrahlung cross section is the largest cross section observed. This leads to events in which bremsstrahlung occurs simultaneously with the event of other type. Since the bremsstrahlung events rejected in the analysis then genuine photoproduction events with bremsstrahlung overlays were also removed from the sample. However, the remnant contribution of these events has to be corrected for with Δ_{BSO} factor. At this moment one should note that photon-removal is not 100% efficient since the the photon calorimeter acceptance is not 100%. This is corrected with the correction factor $\Delta_{\gamma acc.}$. Eventually, the photoproduction cross section is corrected to the Born level with the factor Δ_{RAD}.

Finally, the photoproduction cross section is

$$\sigma_{tot}^{\gamma p} = \frac{N(y)}{\mathcal{L}} \frac{1}{f_\gamma} \frac{1}{A_{35m}} \ \frac{1}{A_{UCAL}} \Delta_{TRIG} \ \Delta_{RAD} \Delta_{\gamma acc.} \Delta_{BSO}. \tag{4.6}$$

In the following sections, the determination of particular terms in the above formula will be discussed.

4.6 Event Selection

The data used to measure the total cross section for photoproduction were taken in a series of four runs. The total cross section dedicated runs were taken over a limited period of time. This was done to limit systematic variations. The variation of the energy calibration of the 35m tagger and the LUMI-photon calorimeter, the drifts of the x-vertex and the positron beam x-tilt were of main concern.

For the photoproduction total cross section runs a special trigger configuration was used. Most of the ZEUS triggers used in normal running were switched off. It was required that the interacting photon energy is known. This was achieved by tagging scattered positrons in the 35m tagger.

The FLT requested at least 5 GeV deposited in the 35m tagger. For events with $W_{\gamma p} \approx 200$ GeV the photons emitted by the tagged positrons scatter in the RCAL. Therefore events with the 35m tagger energy above 5 GeV were taken if the RCAL energy was greater than one of the two thresholds. The following thresholds were used:

   $REMC$: the sum of all the RCAL cells excluding 8 cells around the beam-pipe,

   $REMCth$: the sum of all the RCAL cells.

The requirement was:

$$(REMC > 464 \ MeV).or.(REMCth > 1250 \ MeV)$$

The SLT was used to reduce the beam-gas background. A timing cut was applied to events passing the FLT. The timing was assigned to the energy deposit in the first two rings of the

FCAL and RCAL cells around the beam-pipe. A time was calculated based on the time of the signal peak relative to the proton-positron bunch crossing time. An event was rejected if the difference between the time calculated from the RCAL deposit and the bunch crossing time was more than 8 ns. It was also rejected if the difference of RCAL and FCAL times was more than 8 ns. If there was no valid timing information an event was accepted. Also a cut on the $\Sigma_{CALcells}(E - p_z) < 100$ GeV was applied to reject beam-gas events. One should note that $\Sigma_{CALcells}(E - p_z)$ is a conserved quantity, and in the case of HERA for fully measured event $E - p_z \approx 55$ GeV.

The TLT was not used to reduce the rate for the total cross section runs. The TLT noise, FCAL and RCAL time, up-down time and cosmic and halo muons vetoes were left on. They rejected 2.4% of the events that were passed to the TLT. The calorimeter cell is defined "noisy" if there is large imbalance between its two PMTs, $E_{RL} = \frac{|E_R - E_L|}{E_R + E_L} > 0.9$ and $E_L + E_R > 1.5$ where E_L (E_R) is the left (right) PMT energy. Five events out of 600 000 were rejected by this requirement.

At the trigger stage the calorimeter time is used to reject beam-gas, cosmic and halo muon events. The algorithm uses the energy weighted average time. The time is calculated for RCAL (t_{RCAL}), FCAL (t_{FCAL}) and the entire UCAL (t_{global}) using cells with the energy deposit above 200 MeV. An event was rejected if $|t_{RCAL}| > 6$ ns or $|t_{FCAL}| > 8$ ns or $|t_{RCAL} - t_{FCAL}| > 8$ ns or $|t_{global}| > 8$ ns.

It is worth pointing out that the above timing information is different from that used by the SLT (timing from pre-selected cells around the beam-pipe). The cosmic and halo muon events are removed on the basis of the correlation between the time and position of the energy deposits in the UCAL. Also the barrel muon chamber information, the SLT VETO results and TLT track and vertex information is used [124].

After the selection procedure the number of events was

$$\mathcal{N} = 22533 \pm 162. \tag{4.7}$$

4.7 Running Condition Stability

During empty bunch crossing the light-test triggers provided a stable source for monitoring any calibration drifts of the luminosity detector. Also the average pedestals of the PMT channels provided a mean for the stability control. The measurements for both the 35m tagger and the photon-calorimeter showed a very stable performance of the luminosity detector.

Also the stability of the x-vertex and the positron beam x-tilt has been checked The x-vertex stability was checked by plotting the x-vertex as determined by the CTD as a function of the event number. Since the x-tilt is equivalent to the most probable position measured by the LUMI-photon calorimeter this value was plotted against the event number. No systematic variations were found. The average x and y position measured by the LUMI-photon calorimeter are listed in Table 4.1 for four photoproduction runs.

4.8 Special Bremsstrahlung Runs

Owing to the small bremsstrahlung photon emission angles ($< \Theta_\gamma >= m_e/E \approx 20$ μrad), a large and well known distance between the calorimeter and the IP and the photon position

Table 4.1: Average photon position measured by the LUMI-photon calorimeter

run number	$< x_{photon} >$ cm	$< y_{photon} >$ cm
22781 – nominal	-1.4	0.0
22783 – negative x-tilt	-3.2	0.3
22785 – positive x-tilt	0.5	0.1
22787 – positive y-tilt	-1.4	2.3
22789 – negative y-tilt	-1.5	-3.2

detector the lepton beam angles (beam tilts) at the IP could be precisely determined. This feature was exploited in a series of the dedicated bremsstrahlung runs. These runs were taken with the nominal value of the positron beam tilt and also for different x and y tilts. The goal was twofold. On one hand the runs were intended to check stability. On the other to find the positron energy interval for which the result is least dependent on the positron beam tilt.

The tilt distributions were measured with the help of the photon-calorimeter position detector. To reconstruct the photon position a clustering algorithm [134] was applied. This algorithm was also used for the positron position reconstruction within the 35m tagger.

The algorithm searched for a cluster and determined its "quality" on the basis of the number of the position detector fingers belonging to the cluster, and the cluster position w.r.t. the calorimeter fiducial volume. A "good" cluster meant that at least to fingers belong to it, while a "very good" cluster had at least three fingers' and was located away from the calorimeter edges. For the energy spectra a "good" cluster flag was requested while for all position related distributions a "very good" cluster flag was required.

In addition the x and y of the vertex and the tilt distributions can be calculated from the beam position monitors' (BPM) measurements. The HERA BPMs are placed symmetrically with respect to the IP at the distances of 7, 54 and 68 meters. They are equipped with four pick-up electrodes paired for the x and y readout. These devices measure the beam position with a precision of about 0.1 mm [135]. However, their position within HERA is known to about 1 mm. Moreover, the presence of both beams in the machine may distort the measurements. Therefore their absolute measurements were not used.

Figs. 4.12 and 4.13 show the vertex and tilts as measured by the 7m BPMs. Both, the beam tilt and vertex position are stable.

To find the best interval of the positron energy for the total cross section measurement the experimental 35m tagger acceptance for the bremsstrahlung events was defined as follows

$$A(E_{beam} - E_\gamma) = \frac{\#\text{events}(E_\gamma > 5 \text{ GeV}, E'_e > 5 \text{ GeV})}{\#\text{events}(E_\gamma > 5 \text{ GeV})} \ . \tag{4.8}$$

The distribution of A is shown in Fig. 4.14 as a function of $E_{beam} - E_\gamma$, the anticipated scattered positron energy for x and y tilted runs. The acceptance very weakly depends on the y-tilt. The horizontal tilt plays an important role. As can be observed from the figure the positron energy interval of 12 to 16 GeV is the least sensitive to the positron beam tilt. This interval was chosen for the photoproduction total cross section measurement.
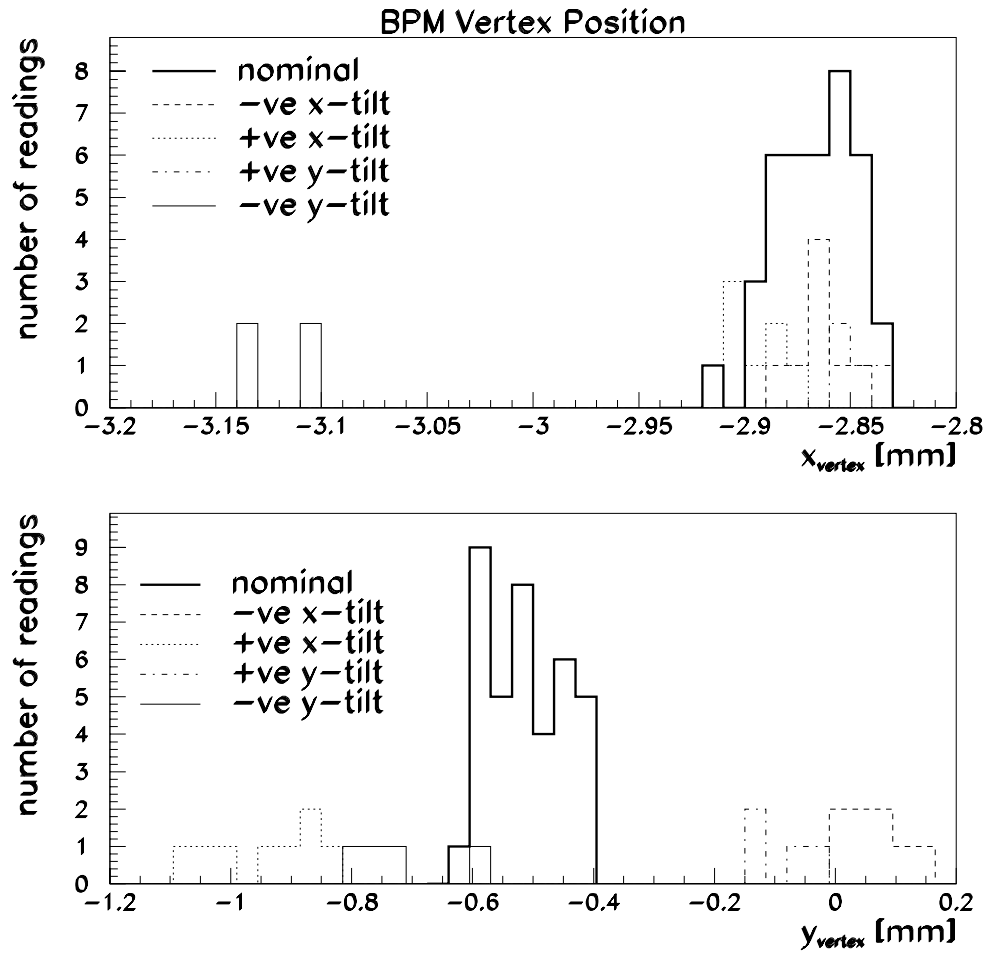
56

Figure 4.12: Distribution of the vertex x and y coordinates calculated from the measurements of the BPMs located at ± 7m.
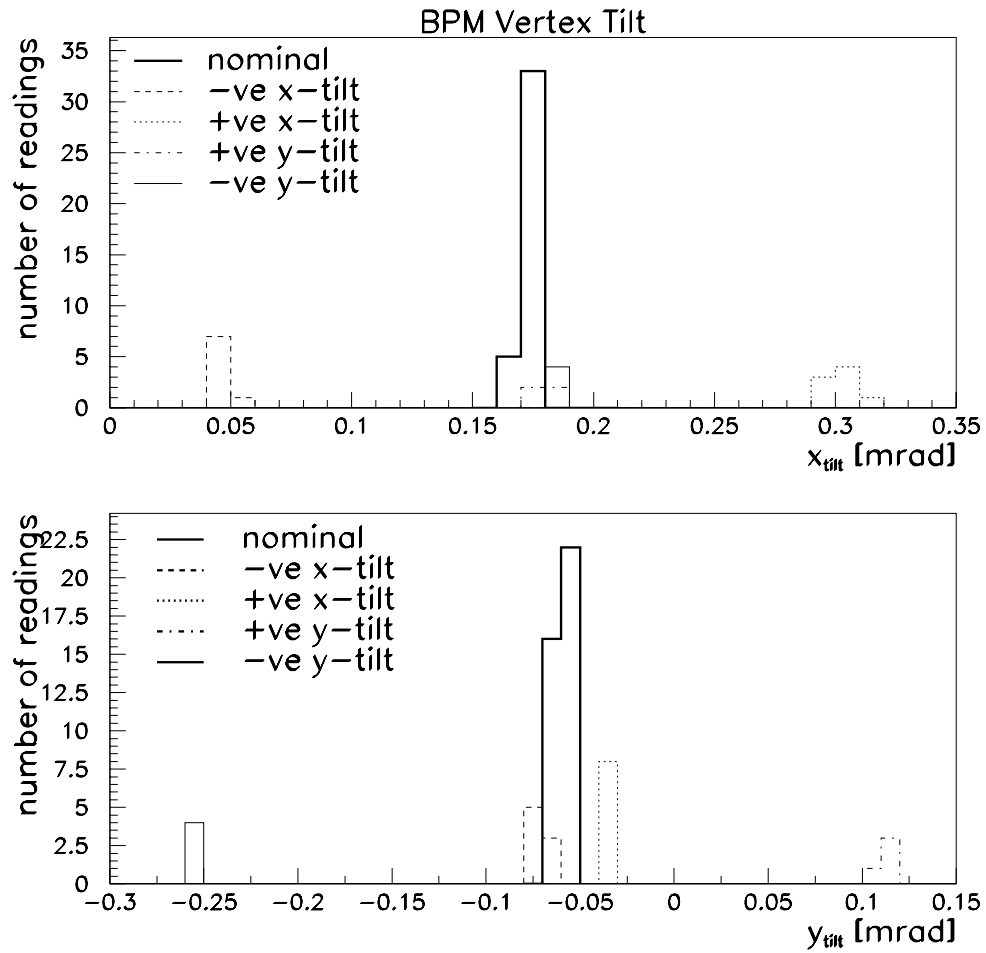
Figure 4.13: Distribution of the positron beam x and y tilts calculated from the measurements of the BPMs located at ± 7m.
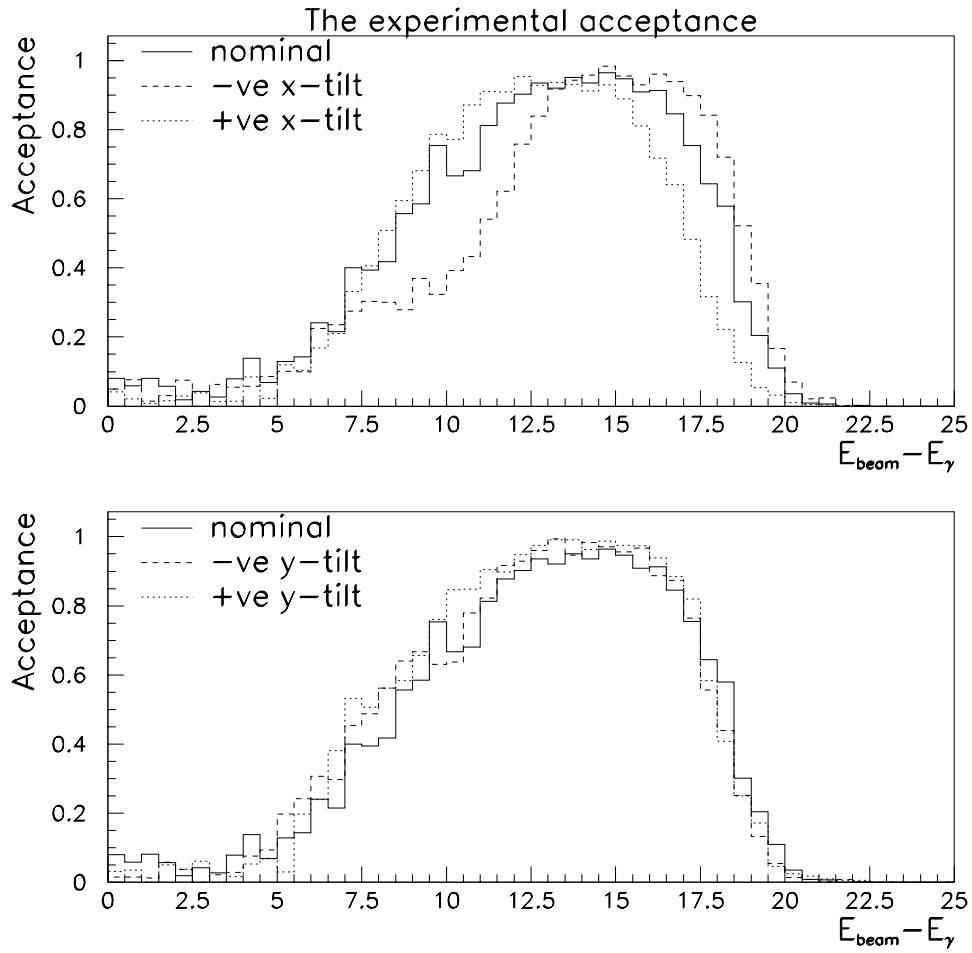
Figure 4.14: Experimental 35m tagger bremsstrahlung acceptance of Eqn. 4.8 for the x- and y-tilted bremsstrahlung runs.

4.9 Monte Carlo Simulations

4.9.1 Bremsstrahlung Simulation

The Bethe-Heitler process has been simulated using the BREMGE Monte Carlo [136]. It includes event pileup effects.

4.9.2 Photoproduction Simulation

The Heracles Monte Carlo and Hector programs were used to simulate the outgoing positron and radiative effects.

Heracles 4.6 [137] is an event generator which simulates the $e^{\pm}p$ charged and neutral current interactions. It includes radiation from both the quark and lepton lines, the interference of lepton and quark radiation, as well as the complete one–loop weak corrections. The generator is capable of integrating the cross section over a phase space region defined by the W, x, y and Q^2 kinematic variables. The latter three are defined by the outgoing lepton energy and the scattering angle. The program performs event generation for such defined regions. Moreover, Heracles 4.6 allows for a separate treatment of the Born and the QED correction subparts and is interfaced to other MC codes. These features make it possible to study the influence of higher-order QED processes on measured observables.
The Heracles 4.6 results can be compared to the Hector 1.11 [138] analytical calculations. Hector includes the full set of virtual electroweak, QCD (up to next–to–leading order), and lowest- and leading-higher-order QED corrections. The calculations can be performed for limited phase space regions, defined in terms of kinematic variables, and for a particular selection of the angular and energy ranges of emitted radiation. In the present work, a branch of Hector 1.11 named TERADLOW was used, which calculates the double differential photoproduction cross section in lepton variables.

Both Heracles and Hector allow the use of different nucleon structure functions and low Q^2 parameterisation of the cross section. The radiative corrections calculated with both programs agree within 1–2 % [139], depending on the correction and process type, parameterisations used, and the phase space region of interest.

4.9.3 Hadronic Final State in Photoproduction Simulation

Two independent Monte Carlo generators were used to simulate the hadronic final state for photoproduction. The first one, Pythia 5.7 [140], was used to generate elastic, dissociative, non-diffractive and hard processes. It includes the radiative processes and corrections as calculated by Heracles 4.6. For the elastic, dissociative, and non-diffractive processes, Pythia has been set to inclusive mode, in which all of these processes are generated at the same time. The second generator, Herwig 5.9 [141], was used to generate the minimum bias and hard photoproduction samples. Figure 4.15 shows diagrams of all the subprocesses.

Dominant processes

• Soft photoproduction via VDM

Elastic

Proton Dissociative

Photon Dissociative

Double Dissociative

Minbias

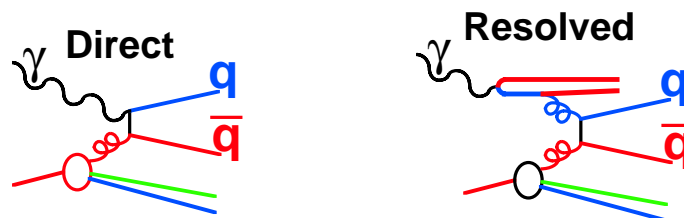## • Hard photoproduction

Direct

Resolved
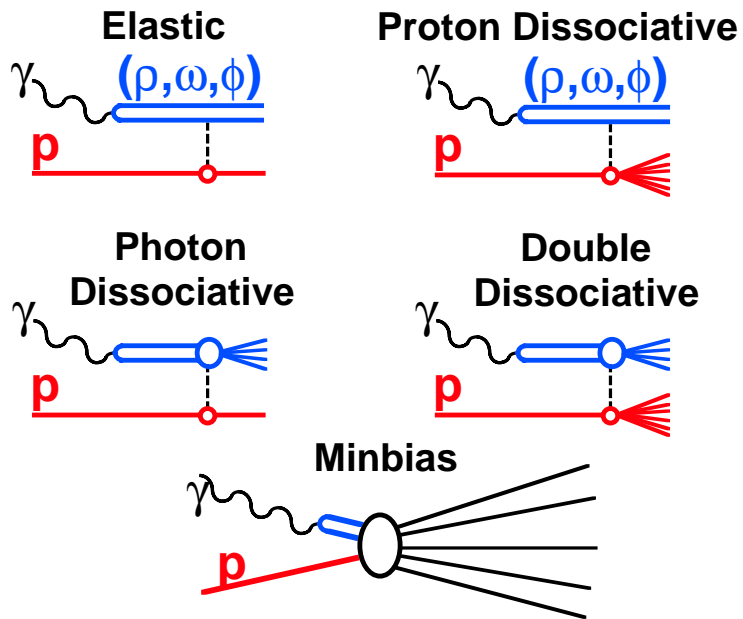
Figure 4.15: The dominant γp subprocesses.

Pythia Monte Carlo

Pythia uses the following model [61] for the photoproduction. The photon has three components:

$$|\gamma> = \sqrt{Z_3}|\gamma_B> + \sum_{V=\rho,\omega,\phi} \frac{e}{f_V}|V> + \frac{e}{f_{q\bar{q}}}|q\bar{q}>$$

where

$$Z_3 = 1 - \sum_{V=\rho,\omega,\phi} \left(\frac{e}{f_V}\right) - \left(\frac{e}{f_{q\bar{q}}}\right).$$

This components correspond to the interactions of the "bare", "VDM-like" and "anomalous" photon. The bare photon leads to direct events. The photon interacts directly with a parton from a proton. Typically the event contains two high-p_t jets and a proton remnant. The VDM events are characterised by a fluctuation of the photon into a vector meson. Subsequently the meson interacts with the proton. The coefficients $f_V^2/4\pi$ are assumed to be energy independent. This class contains elastic, diffractive low-p_t and high-p_t events. For the latter the photon also generates a beam remnant. In the anomalous component the photon fluctuates into a $q\bar{q}$ with a virtuality larger than for VDM class. This process is perturbatively calculable. It leads to high-p_t jet production. At the level of the cross sections

$$\sigma_{tot}^{\gamma p} = \sigma_{dir}^{\gamma p} + \sigma_{VDM}^{\gamma p} + \sigma_{anom}^{\gamma p}.$$

The so-called resolved high-p_t events contain a contribution from the anomalous and the VDM classes.

The total cross section is parameterised as in [2]. The total VDM cross section is based on the additive quark model [13] and the fits [2] to πp and Kp data. As was mentioned above in the VDM class the events' types known from the hadron-hadron collisions may occur. These are outlined below.

Elastic scattering

The elastic scattering process is $\gamma^* p \to Vp$, where $V = \rho^0, \omega, \phi, J/\Psi$. Note that the truly elastic (Compton) process $\gamma^* p \to \gamma p$ is negligible above the threshold for vector-meson production and has been ignored. The probability for the transition $\gamma \to V$ is given by $(f_V^2/4\pi)^{-1}$. The t-distribution is steeply falling

$$\frac{d\sigma^{Vp}}{dt} = \frac{(\sigma_{tot}^{Vp})^2}{16\pi} exp(-b_{elas}t)$$

The coupling constants are: $f_V^2/4\pi = 2.2(\rho)$, $23.6(\omega)$, and $18.4(\phi)$. The t-slope is given by

$$b_{elas} = 12.7 \text{ GeV}^{-2} = 2b_V + 2b_p + 4W^{2(0.0808)} - 4.2$$

where $b_{\rho^0,\omega,\phi} = 1.4 \text{ GeV}^{-2}$, $b_{J/\Psi} = 0.23 \text{ GeV}^{-2}$ and $b_p = 2.3 \text{ GeV}^{-2}$. The momentum transfer is generated in the range $-W^2/2 < t < 0 \text{ GeV}^2$.

Photon-dissociative Scattering

In the photon dissociative process the photon dissociates into a higher mass state, $\gamma^* p \to Xp$. The photon dissociative system is generated with

$$\frac{d\sigma_{Xp}}{dtdM_X^2} = \frac{g_{3\mathbb{P}}}{16\pi}\beta_{\gamma\mathbb{P}}\beta_{p\mathbb{P}}^2\frac{1}{M_X^2}exp(-b_{Xp}|t|)F_{Xp}$$

$$b_{\mathrm{Xp}} = 2b_p + 2\alpha'_{\mathbb{P}}\ln\frac{W^2}{M_X^2}$$

where $b_p = 2.3$ GeV^{-2}, $\alpha'_{\mathbb{P}} = 0.25$, and $g_{3\mathbb{P}} = 0.318\sqrt{\text{mb}}$. The dissociative mass is generated in the range $2m_\pi < M_X < W^2/2$ GeV. The term F_{Xp} is introduced explicitly to suppress production close to the kinematic limit.

Proton-dissociative Scattering

Proton dissociative events are those events in which the proton is excited into a higher mass state, $\gamma^* p \to VN$.
The proton dissociative system is generated with

$$\frac{d\sigma_{\gamma N}}{dtdM_N^2} = \frac{g_{3\mathbb{P}}}{16\pi}\beta_{\gamma\mathbb{P}}\beta_{p\mathbb{P}}^2\frac{1}{M_N^2}exp(b_{\gamma N}t)F_{\gamma N}$$

$$b_{\gamma N} = 2b_V + 2\alpha'_{\mathbb{P}}\ln\frac{W^2}{M_N^2}.$$

The dissociative mass is generated in the range $2m_\pi < M_X < \sqrt{s}$ GeV. The term $F_{\gamma N}$ suppresses explicitly production close to the kinematic limit.

Double-dissociative Scattering

The double dissociative processes contain events in which both the proton and the photon dissociate into higher mass states, $\gamma^* p \to XY$. These events were generated with

$$\frac{d\sigma_{dd}}{dtdM_X^2 dM_Y^2} = \frac{g_{3\mathbb{P}}^2}{16\pi}\beta_{\gamma\mathbb{P}}\beta_{p\mathbb{P}}\frac{1}{M_X^2 M_Y^2}exp(b_{dd}t)F_{dd}$$

$$b_{\mathrm{dd}} = 2\alpha'_{\mathbb{P}}\ln\left(e^4 + \frac{W^2}{M_X^2 M_Y^2 \alpha'_{\mathbb{P}}}\right).$$

The dissociative mass is generated in the range $2m_\pi < M_X + M_Y < \sqrt{s}$ GeV. The term F_{dd} is introduced explicitly to suppress production close to the kinematic limit and to suppress configurations where the two diffractive systems overlap in rapidity space.

Soft Scattering

The non-diffractive soft part consists of events with small transverse momentum. These events are neither dissociative nor elastic. Since the soft scattering is not calculable in perturbative QCD these processes are modeled using the parameterisations based on previous measurements.

Hard Scattering

Hard scattering is described by the direct and resolved (hard VDM and anomalous) processes. In the former the photon directly couples to the parton of the proton. Its full energy is involved in the interaction. Two mechanisms dominate: the QCD Compton where the photon is absorbed a quark and a gluon is emitted, and the boson-gluon fusion where the photon combines with a gluon and creates a quark-anti-quark pair. The event contains two high-p_t jets and the proton remnant. The cross section is

$$\sigma_{dir}(p_0) \sim \int_{p_j^2}^{W/4} \frac{D(F_2^p)}{p_t^2} dp_t^2$$

where D depends on the proton structure function F_2^P and p_0 is a parameter which is set to $m_\phi/2$ in Pythia.

In resolved processes the photon is a source of quarks and gluons. In the interaction this structure can be resolved and the partons from the photon and the proton can interact in hard scattering. The event contains two jets and both the proton and photon remnant. The cross section is given by

$$\sigma_{dir}(p_t^{min}) \sim \int_{(p_t^{min})^2)}^{W/4} \frac{H(F_2^p, F_2^\gamma)}{p_t^4} dp_t^2$$

where $H(F_2^p, F_2^\gamma)$ depends on both the proton (F_2^p) and the photon (F_2^γ) structure functions. The parameter p_t^{min} has a value of 1-2 GeV and was estimated from the data [142].

Herwig

The Herwig Monte Carlo [141] was used to generate non-diffractive and hard photoproduction samples. Herwig makes use of the parton cluster model. The partons of the incident hadrons develop a parton shower. The perturbative showering is terminated at a low scale, $Q_0 < 1$ GeV. All the outgoing gluons are split non-perturbatively into $q\bar{q}$ pairs. The pre-confinement [143] property is used to create colour-singlet clusters [144]. These clusters decay into the observed hadrons. The remnant of incoming particles is modeled by soft minimum bias hadron-hadron interactions.

Minimum Bias Processes

The model used is based on the minimum-bias pp generator of UA5 [145]. The generator starts with negative binomial distribution of the charged multiplicity. Because the nominal

Herwig average charged multiplicity parameterization is based on pp data, for the current event generation, the parametrization has been changed, according to a study [146] of the ZEUS 1993 $\sigma_{TOT}^{\gamma p}$ data, to be

$$\langle n \rangle = 8.96 \cdot W_{\gamma p}^{(0.23)} - 10.61.$$

The Donnachie and Landshoff parameterisation of the total cross section is used to calculate the event weight. The non-diffractive cross section is assumed to be 70% of the total. For the lepton beam a photon is first generated with Equivalent Photon Approximation and then on-shell photon cross section is used. The beam clusters for colliding particles are created. Then additional clusters are created until the required multiplicity is reached. The clusters' momenta are selected according to a flat rapidity distribution with a Gaussian falloff at the ends. The beam clusters occupy the ends of the distribution.

Hard Photoproduction

The resolved processes are generated using possible binary processes. The direct photoproduction is extended from the heavy quark production. It includes all quark pair creation as well as QCD Compton events.

Hard photoproduction events are generated using Pythia and Herwig at leading order. Both Monte Carlo samples used in this analysis used the proton structure function CTEQ 4L LO [147] and the photon structure function GRV G LO [103]. The events were generated with $p_t^{min} = 2.5$ GeV/c. Direct and resolved processes were generated separately.

4.10   Monte Carlo Tuning of Beam-line Parameters

The Monte Carlo acceptance calculations rely on the proper description of the apparatus. In particular, the 35m tagger acceptance requires a detailed description of the HERA beam line and the luminosity detector setup. The Geant 3.13 MC [148] description of the beam line was checked against the machine database for the magnet type, field and geometry. The simulated beam energy and the positron beam orbit were compared to the ones delivered by the HERA machine group [149]. A good match between the two was found. In addition, the MC description of the LUMI setup was checked for materials, geometry and for its calibration.
The luminosity detector is calibrated in the way described in [121]. The LUMI-photon calorimeter is calibrated with bremsstrahlung events. The maximum energy of the bremsstrahlung photons equals to the positron beam energy. Therefore, constraining the position of the high energy edge of the photon energy spectrum yields the energy calibration of the calorimeter. The 35m tagger energy calibration is based on the energy conservation in the bremsstrahlung events $E_e + E_\gamma \approx E_{beam}$ and uses the LUMI-photon calorimeter calibration. In Fig. 4.16 the experimental bremsstrahlung photon spectrum measured by the LUMI-photon calorimeter is compared to the results of the Monte Carlo simulations. The bremsstrahlung MC [136] describes data well, except that a difference in the E_γ resolution is seen for $E_\gamma \approx E_{beam}$. During the generation the event pile-up was taken into account. An average of 0.25 bremsstrahlung
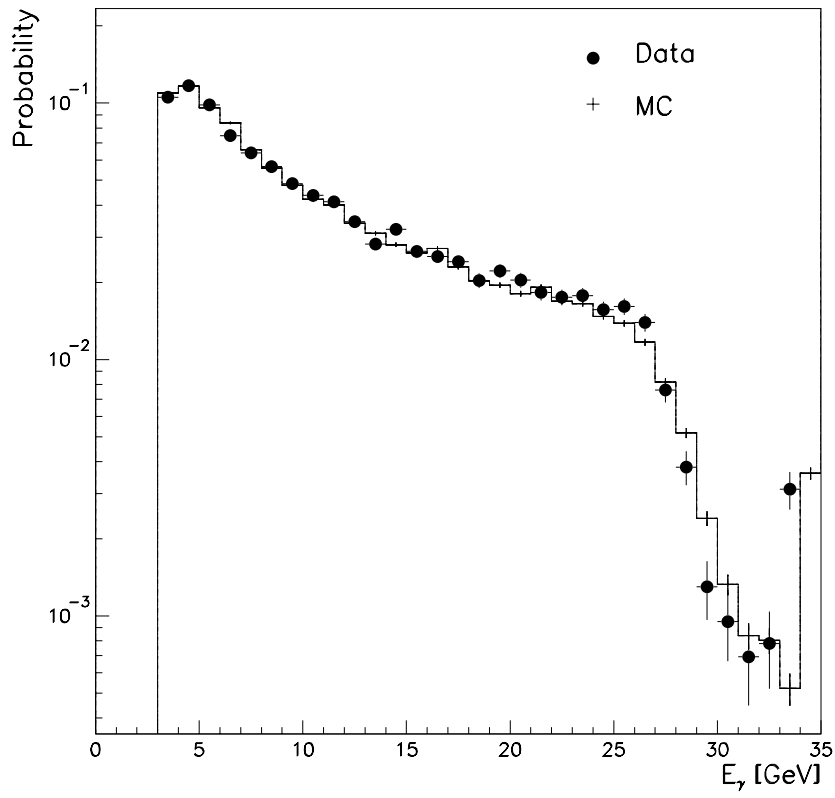
Figure 4.16: The comparison of the bremsstrahlung photon energy spectra measured by the LUMI-photon calorimeter (black dots) and the results of the MC apparatus simulation (histogram). Both data and MC are normalised to the total number of events.
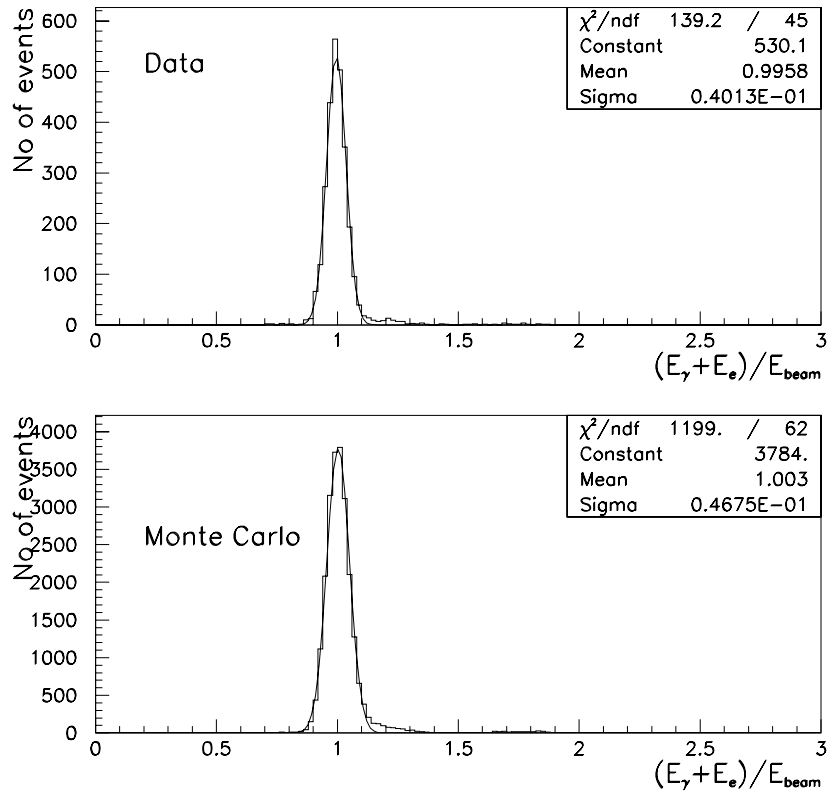
Figure 4.17: Comparison of the ratio $(E_e + E_\gamma)/E_{beam}$ for the bremsstrahlung data and Monte Carlo (histograms). The positron energy E_e is in rage 10–18 GeV and photon energy $E_\gamma > 3$ GeV. A Gaussian fit is depicted with the solid line.

67

events per bunch crossing [150] with the photon energy above 100 MeV was assumed. In Fig. 4.17 the distribution of $(E_e + E_\gamma)/E_{beam}$ is depicted for positron energies between 10 and 18 GeV and $E_\gamma > 3$ GeV. The energy calibration of the 35m tagger and the MC calculation agree to within about 1%. However, the Monte Carlo shows worse resolution than that in the data. This difference was investigated by changing various parameters of the MC. No explanation for this small discrepancy was found in the MC description of the LUMI detectors.

Since the 35m tagger bremsstrahlung acceptance was found to be primarily sensitive to variations in the horizontal plane then the MC tuning was restricted to the x coordinate of the vertex position (x-vertex) and the positron beam tilt in the $x - z$ plane (x-tilt). The tuning was performed as follows. For a given x-tilt and x-vertex a set of bremsstrahlung events including event pile-up effect was generated. The events were requested to have at least 3 GeV of energy carried by photons. The sample was run through the standard ZEUS simulation, calibration and reconstruction chain. Four distributions were used for comparison between the data and MC: the photon and the positron energy spectra, the experimental acceptance A of Eqn. 4.8 and the correlation between the electron energy and position. A global χ^2 was defined as a sum of the χ^2s calculated for each distribution. Then whole procedure was repeated for a number of x-vertex and x-tilt values. The optimal x-vertex and x-tilt were selected as those for which the global χ^2 calculated on the basis of the four distributions was minimum. These were x-vertex = 0.13 cm and x-tilt = -0.15 mrad. Figure 4.18 shows the $\chi^2/d.o.f.$ calculated for the photon spectrum and the correlation between the positron position and energy. Intrinsic resolution of the clustering algorithm is neither shown nor was used during the χ^2 calculations. Fig. 4.19 shows the comparison of the data and MC for the final x-vertex and x-tilt values. The agreement is reasonable. The position-energy correlation is very well reproduced in the region of interest.

The final check was to compare the four distributions for tilted runs. These comparisons are shown in Figs. 4.20 and 4.21. The agreement is reasonable. However, it is significantly worse for the run with positron beam x-tilt of -0.42 mrad. This is attributed to the following:

- this run was taken with the positron beam "aiming" at the edge of the photon exit window, i.e. the acceptance edge,

- the Geant description of the beam-pipe is only approximate due to limited set of possible geometrical volume shapes that can be used.

These factors lead to problems in the tracking of extreme energy and wide angle scattered positrons and photons. Hence, the discrepancies between the data and MC.

4.11   Positron Calorimeter Acceptance

The 35m tagger acceptance was estimated for the the tilt and vertex position optimised as described in section 4.10. The acceptance is defined as

$$\mathcal{A}_{35m} = \frac{\#recon.\ events(12 < E'_e < 16 \otimes \text{``good positron''} \otimes \overline{(E_{\gamma\ recon.} > 1)})}{\#gen.\ events(12 < E_e < 16 \otimes \overline{(E_{\gamma\ gen.} > 1 \otimes \Theta_\gamma < \Theta_{lumi})})} \qquad (4.9)$$
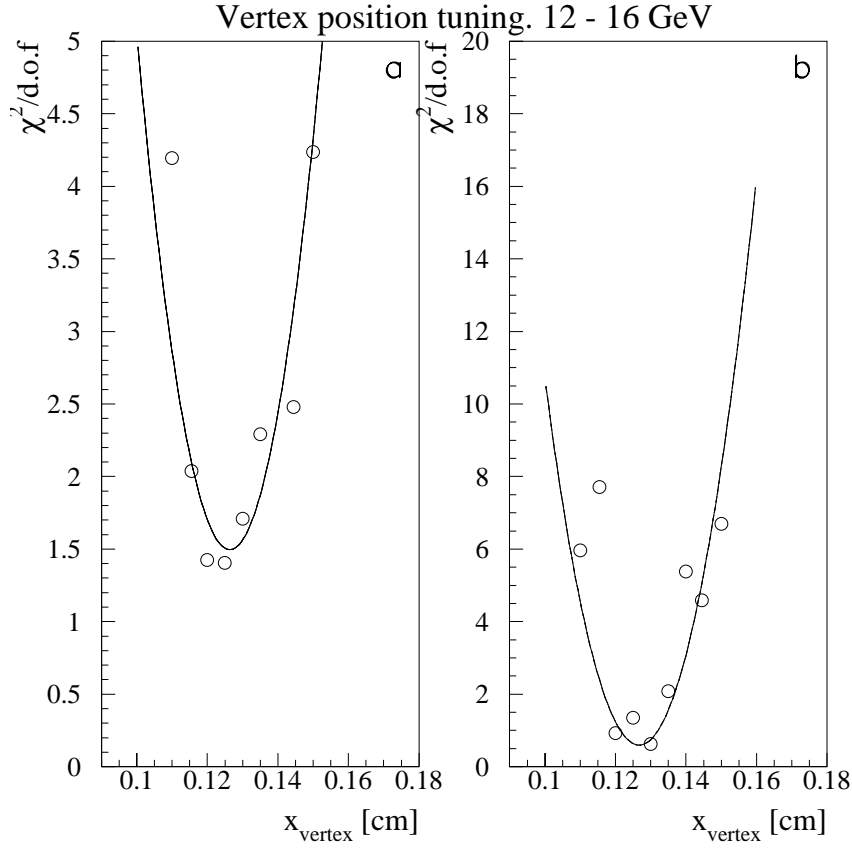
Figure 4.18: The χ^2 plots for the vertex position tuning. (a) The $\chi^2/d.o.f.$ values calculated from the bremsstrahlung photon energy spectra comparison as a function of the x-vertex position. (b) The $\chi^2/d.o.f.$ values calculated for the scattered positron energy–position correlation as a function of the x-vertex position. The curves are drawn to guide the eye.
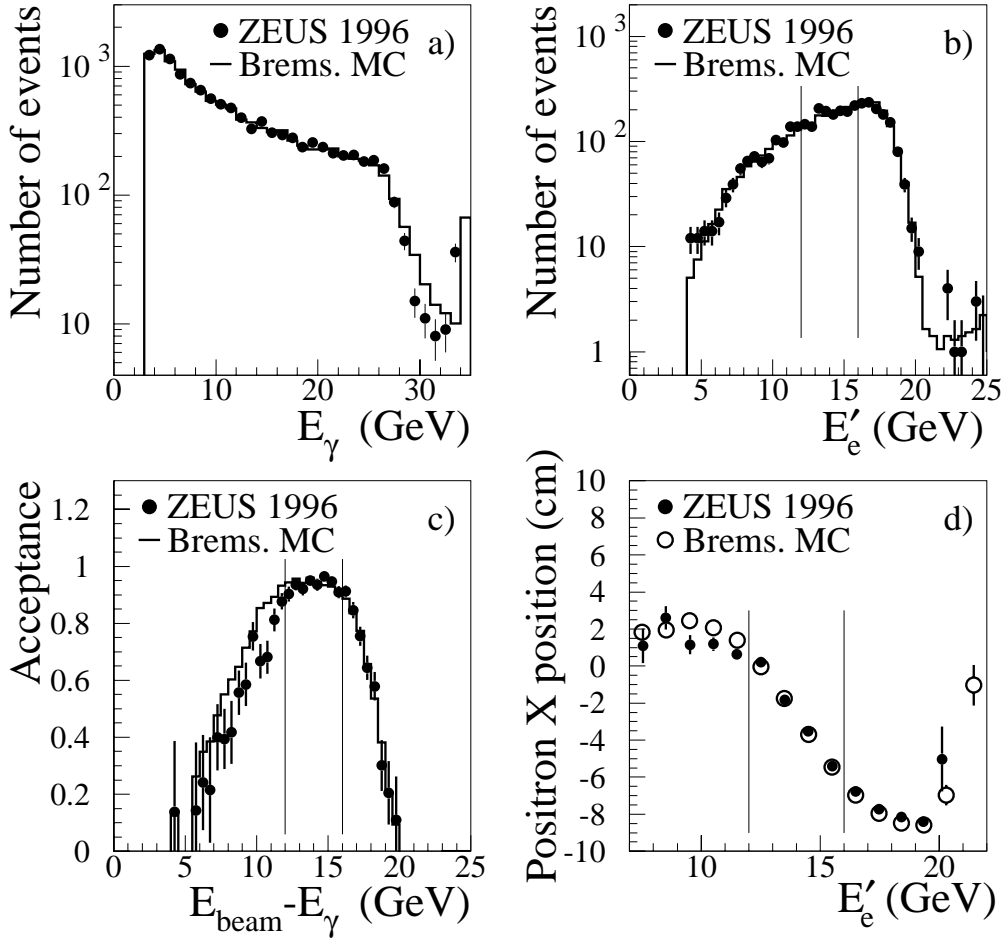
ZEUS

Figure 4.19: Comparison of the BS Monte Carlo to the nominal-tilt data for the optimised positron beam x-tilt of -0.15 mrad and x-vertex of 0.13 cm. (a) The bremsstrahlung photon energy, (b) the scattered positron energy, (c) the experimental acceptance of Eqn. 4.8, (d) the correlation between the positron position and energy. The vertical lines mark the scattered positron energy region used for the measurement.
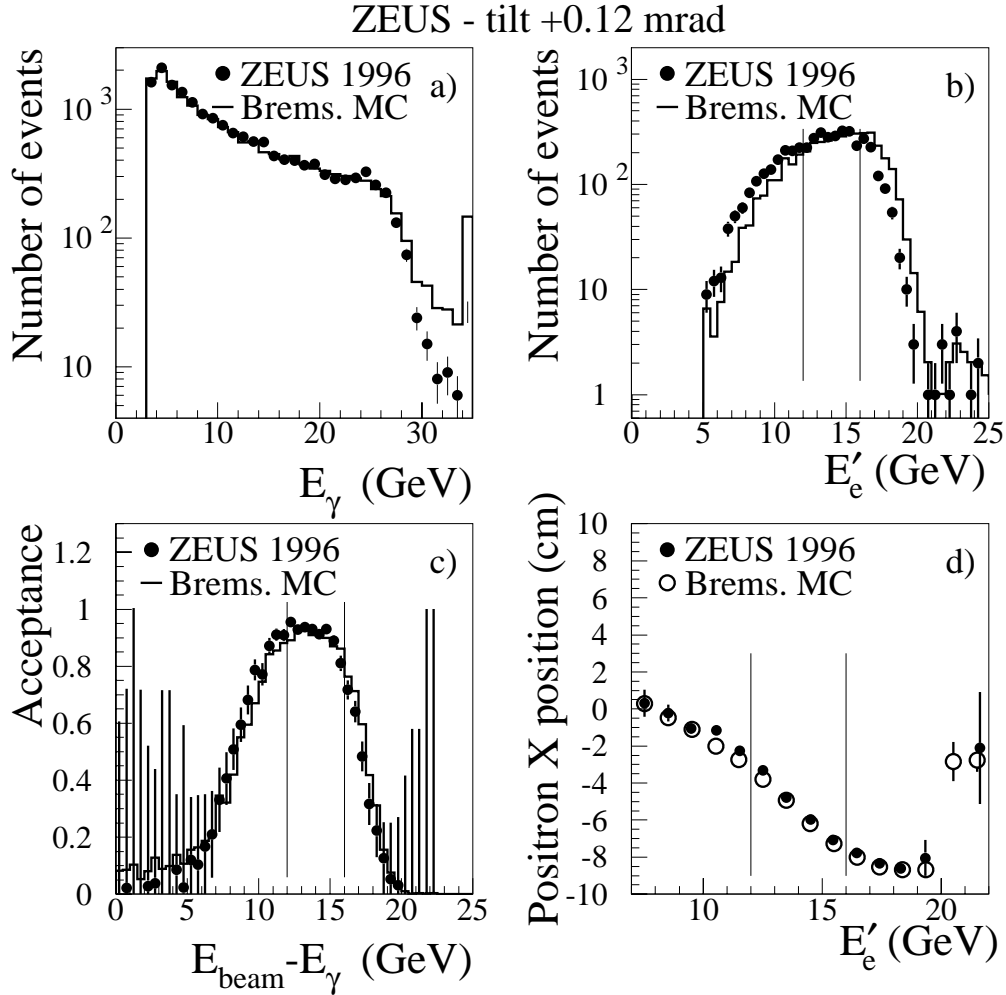
Figure 4.20: Comparison of the BS Monte Carlo to the data for the positron beam x-tilt of +0.12 mrad. (a) The bremsstrahlung photon energy, (b) the scattered positron energy, (c) the experimental acceptance of Eqn. 4.8, (d) the correlation between the positron position and energy. The vertical lines mark the scattered positron energy region used for the measurement.
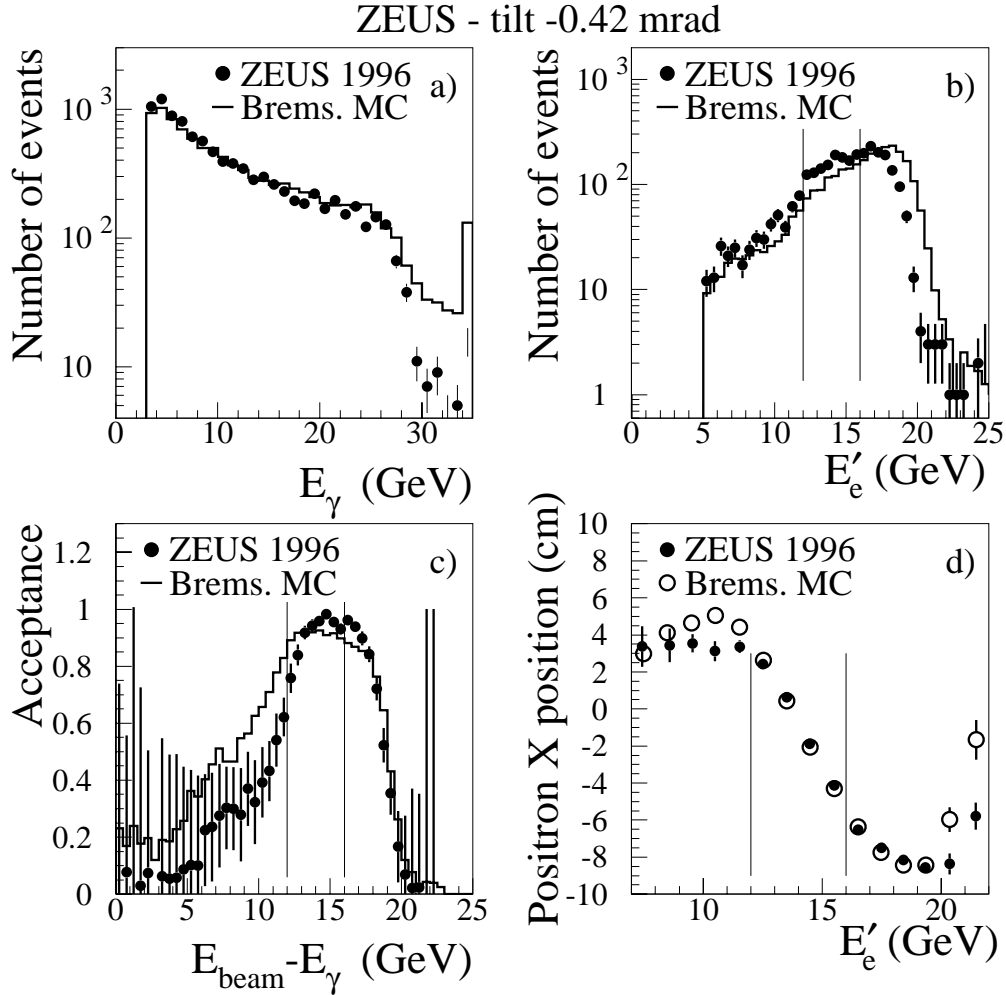
Figure 4.21: Comparison of the BS Monte Carlo to the data for the positron beam x-tilt of -0.42 mrad. (a) The bremsstrahlung photon energy, (b) the scattered positron energy, (c) the experimental acceptance of Eqn. 4.8, (d) the correlation between the positron position and energy. The vertical lines mark the scattered positron energy region used for the measurement.

where E'_e (E_e) is the reconstructed (generated) positron energy, "good positron" means the positron cluster finding quality flag, $E_{\gamma\ recon.}$ ($E_{\gamma\ gen.}$) is the photon measured (generated) energy and Θ_{lumi} is the polar angle acceptance of the photon exit window. The horizontal line over the condition means the condition negation.
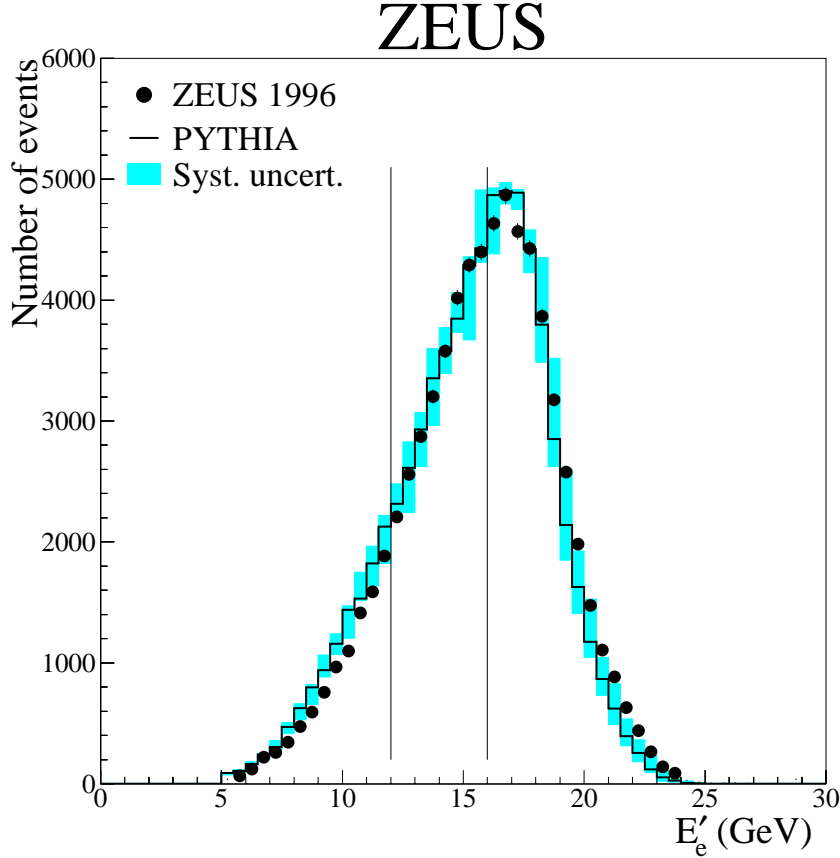

Figure 4.22: The positron energy spectrum for photoproduction data (full circles) and tuned MC events (histogram with systematic uncertainty band). The selected region, $12 < E'_e < 16$ GeV, is shown by the vertical lines.

To calculate the acceptance PYTHIA MC [140] was used. The radiative corrections were calculated with the HERACLES 4.6 Monte Carlo [137] interfaced to PYTHIA. The low Q^2 cross section behaviour was parameterised according to the ALLM [39] parameterisation. The positron energy distribution for photoproduction data (full circles) and tuned MC events (histogram with systematic uncertainty band) is shown in Fig. 4.22. The region selected for the cross section measurement, $12 < E'_e < 16$ GeV, is depicted by the vertical lines. The data are reasonably well described by the PYTHIA MC.

Fig. 4.23 shows the comparison of the simulated and measured correlation between the position and energy of the scattered positron. The photoproduction data are marked with full circles

while the open circles depict the prediction of the PYTHIA MC. The region selected for the cross section measurement, $12 < E'_e < 16$ GeV, is depicted by the vertical lines. The agreement between the data and the PYTHIA MC simulated events is very good.
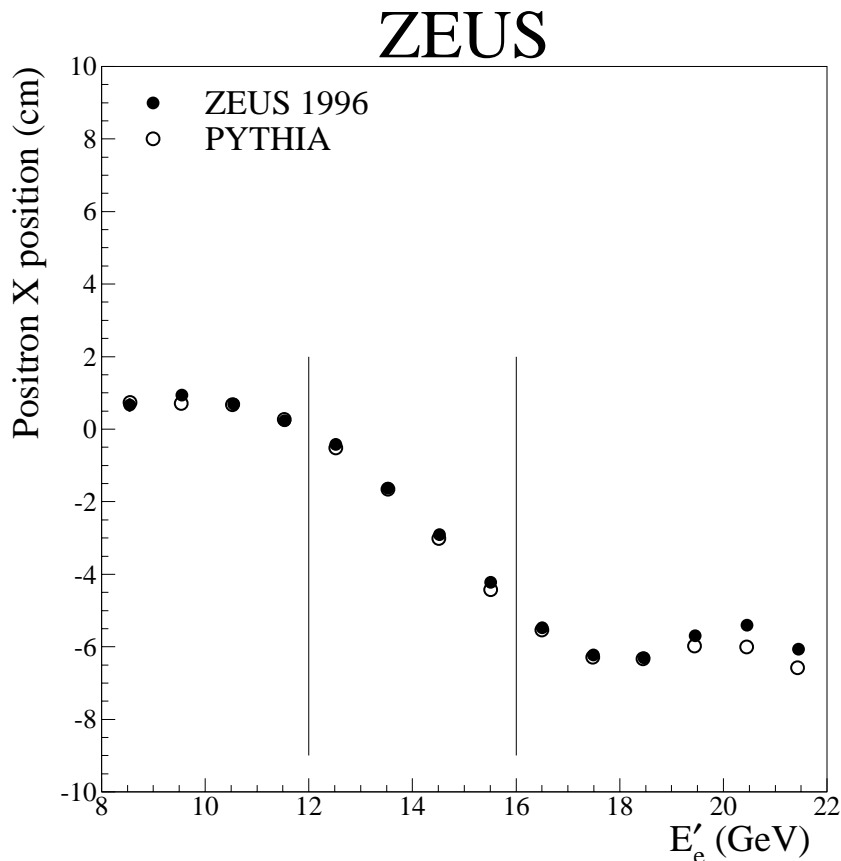

Figure 4.23: The correlation between the position and energy of the scattered positron for photoproduction data (filled circles) and tuned MC events (open circles). The selected region, $12 < E'_e < 16$ GeV, is shown by the vertical lines.

The acceptance of the 35m tagger for photoproduction events was found to be

$$\mathcal{A}_{35m} = 0.693 \pm 0.050(syst.) \tag{4.10}$$

for the scattered positron energy range of $12 < E'_e < 16$ GeV.

The calculation showed also that the 35m tagger acceptance vanishes for $Q^2 > 0.02$ GeV^2. The Q^2-dependence of the 35m tagger acceptance is depicted in Fig. 4.24. One should note that due to the definition of Eqn. 4.9 the acceptance can exceed 100%. Such values are explained by the migration effects. The migration effects are due to the resolution of the positron calorimeter and the rapid fall of the positron energy spectrum with decreasing positron energy. This effect was
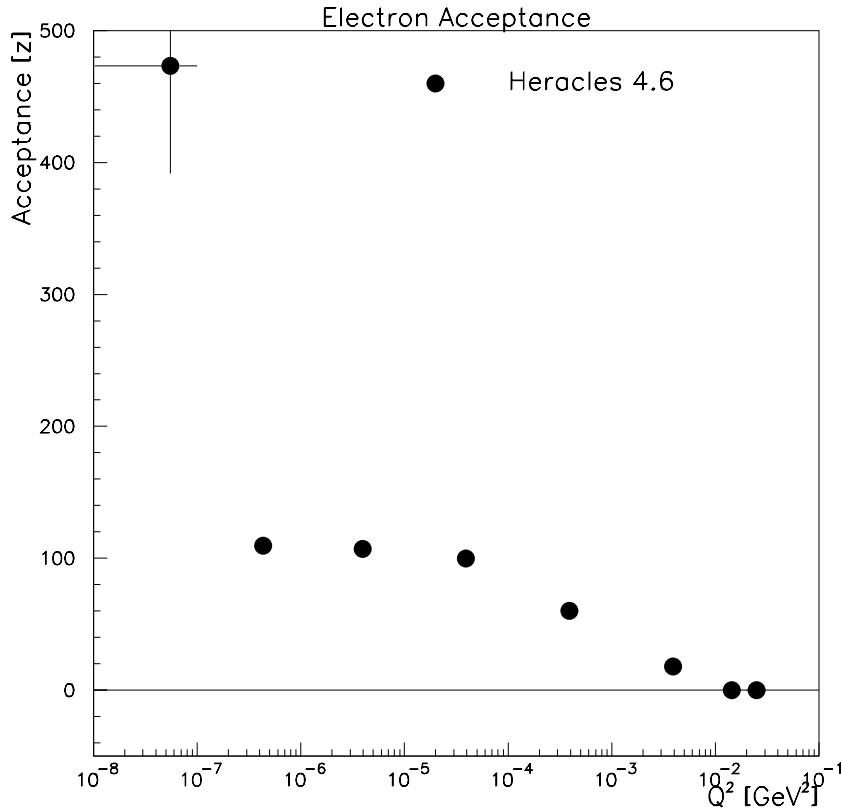
74

Figure 4.24: The 35m tagger acceptance of Eqn. 4.9 in percents for photoproduction events as a function of the four-momentum transfer, Q^2. Events were generated with the HERACLES 4.6 MC interfaced to PYTHIA MC.

particularly strong for $Q^2 < 10^{-7}$ GeV^2. The systematic errors on the 35m tagger acceptance are divided into two classes. The first one takes into account effects of the beams' parameters. Errors due these parameters are treated independently. The second class deals with the positron and photon calorimeter setup and calibration. These errors are correlated. The largest contributions were due to the uncertainty in modeling the scattered positron trajectories and the uncertainty on the energy calibration of the photon detector and its energy nonlinearity.

The 35m tagger acceptance calculation was checked using an event sample with two or more jets in the UCAL. This sample was taken with a trigger independent of the positron calorimeter. The inelasticity of these events can be determined from the UCAL energies alone. Finally for these events the probability to have a positron registered in the LUMI-positron calorimeter was compared to that derived from the tuned photoproduction simulation. The real and simulated data were found to be consistent within the errors.

Table 4.2: UCAL acceptance and fractions for various subprocess for PYTHIA MC. The fractions without listed uncertainty were fixed in the fitting procedure.

Process	$\mathcal{A}_i$	Fraction
elastic $\gamma p \rightarrow V p$	0.477±0.009	0.091
proton dissociative $\gamma p \rightarrow V p$	0.531±0.012	0.045
photon dissociative $\gamma p \rightarrow G p$	0.803±0.006	0.133
double dissociative $\gamma p \rightarrow G N$	0.824±0.007	0.065
hard non-diffractive $\gamma p \rightarrow X$	0.858±0.005	0.166±0.019
soft non-diffractive $\gamma p \rightarrow X$	0.832±0.003	0.498±0.058

4.12 Uranium Calorimeter Acceptance

The calorimeter was used to trigger the photoproduction events by requiring that the energy is deposited in the RCAL. The off-line values of energies were requested such that the trigger was 100% efficient. The MC generated events were passed through the standard ZEUS reconstruction chain. Each physics process has an acceptance which is defined as a fraction of events that pass the RCAL off-line cuts. A sum of subprocesses is fitted to the experimentally measured distributions such as the invariant mass of the interacting system, the transverse energy, the maximum pseudorapidity, η_{max}, of the energy deposit, the total calorimeter energy, with the fractions of subprocesses as the fit parameters. The total acceptance of the calorimeter is then calculated using fit fractions and the acceptances for each subprocess. Generated events for each photoproduction subprocess are passed through the ZEUS MOZART [151] detector simulation and the ZEUS ZGANA [152] trigger simulation.

The primary MC sample was generated using PYTHIA MC. For systematic checks also the HERWIG generated hard and soft non-diffractive photoproduction samples were used. The UCAL acceptance for each subprocess is

$$\mathcal{A}_i = \frac{N_i^{rec}}{N_i^{gen}}$$

where N_i^{gen} is the number of events generated in a certain W bin and N_i^{rec} is the number of events reconstructed in that W interval. The resulting acceptances are listed in Table 4.2. The calorimeter acceptance was obtained by fitting the Monte Carlo to the data distributions. The subprocess fractions were fit parameters.

The ZEUS measurements were used to reduce the number of fit parameters. It was found that the fraction of the photon dissociative reaction is [81]

$$\frac{\sigma(\gamma\, p \rightarrow X_V\, p)}{\sigma_{TOT}^{\gamma p}} = (13.3 \pm 0.5 \pm 3.6)\,\%,$$

and by factorization the fraction of the double diffractive events is:

$$\frac{\sigma(\gamma\, p \rightarrow X_V\, X_N)}{\sigma_{TOT}^{\gamma p}} = (6.7 \pm 0.3 \text{ (stat.)} \pm 1.8 \text{ (syst.)})\,\%,$$

at $W_{\gamma p} = 209$ GeV. For the ratio of elastic to proton dissociative (ρ^0) the measurement yields [64]:

$$\frac{\sigma(\gamma\, p \to V\, p)}{\sigma(\gamma\, p \to V\, X)} = 2.0 \pm 0.2 \text{ (stat.)} \pm 0.7 \text{ (syst.)}$$

The ratio of the direct to resolved photoproduction was fixed to the ratio of the MC reported cross sections, i.e. 1.10 for PYTHIA and 1/2.5 for HERWIG. The elastic cross section is calculated as a sum of ρ, ω and ϕ cross sections [64, 65, 66], i.e., 13.4 μb at W=70 GeV and extrapolated to the $W = 209$ GeV of the current measurement according to the measured energy dependence of the cross sections. The extrapolation yielded 15.8 ± 2.5 μb.

The above experimental constraints reduced the number of fit parameters to two: the soft and hard non-diffractive fractions.

Because data distributions were not described perfectly by the Monte Carlo, the distributions of the soft non-diffractive subprocess, which is the MC process least constrained by experiment, were re-weighted. The re-weighting function was calculated separately for the pseudorapidity distribution of the CAL cells, the total transverse and the RCAL energy distributions. Figures 4.25 and 4.26 show a comparison of the data and fitted Monte Carlo distributions for the invariant hadronic mass measured with the calorimeter M_X^{CAL} and the number of hit calorimeter cells N_{cells}, respectively. Also the subprocess contributions are shown. The estimated systematic errors are depicted as a band in the figures. As a consistency check the RCAL energy distribution, which was not fitted, is shown with the MC distributions in Fig. 4.27. The data are well described by the fitted MC samples.

The UCAL acceptance is

$$\mathcal{A}_{UCAL} = 0.781^{+0.022}_{-0.016}. \tag{4.11}$$

The largest contribution to the systematic uncertainty results from the different Monte Carlo models used to calculate the acceptance. Major contributions are also due to the RCAL and the positron calorimeter energy scale and due to the errors on the measured fractions of the subprocesses.

4.13 Correction Factors

In the following the correction factors to the total cross section are discussed.

4.13.1 Trigger Inefficiencies

The selection criteria used in the off-line data analysis are tightened after the data had been written to the tape. The cuts on the positron energy and the RCAL energy were based on studies of the RCAL and the LUMI-positron calorimeter acceptance. Cuts were placed to eliminate various background processes. Fast digitisation of the UCAL signal is done by the Calorimeter First Level Trigger (CFLT) so the decision can be issued every 96 ns. The CFLT uses a separate calibration of the calorimeter energy compared to that used by the slower main read out. One way to control the systematics in the total cross section run is to precisely calibrate the fast digitisation of the trigger.
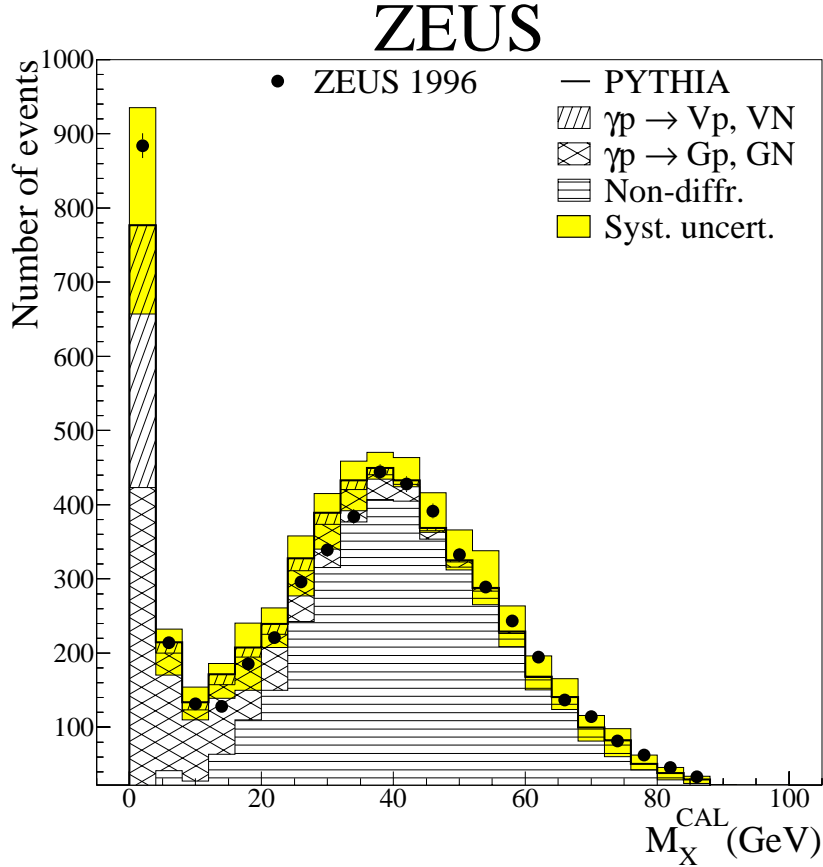
Figure 4.25: The distribution of the hadronic invariant mass, M_X^{CAL}, for data (full circles) and fitted total photoproduction sample (histogram with systematic uncertainty band). The fit is made to the M_X^{CAL} and N_{cells} distributions. Cumulative subprocess contributions are shown. The elastic and proton-dissociative, the photon-dissociative and double-dissociative, the soft and hard non-diffractive samples have been combined.

The Fast Clear first level trigger abort system reads out all the energies reported by the calorimeter trigger. These energies were compared to the energies reported by the main calorimeter readout. For the total cross section runs the following thresholds were found for RCAL cells such that the $REMC$ and $REMCTH$ (see sec. 4.6) were 100% efficient [2]:

$REMC > 600$ MeV, or

$REMCth > 1550$ MeV, or

the sum of reported calorimeter energies of any two cells was greater than 850 MeV.

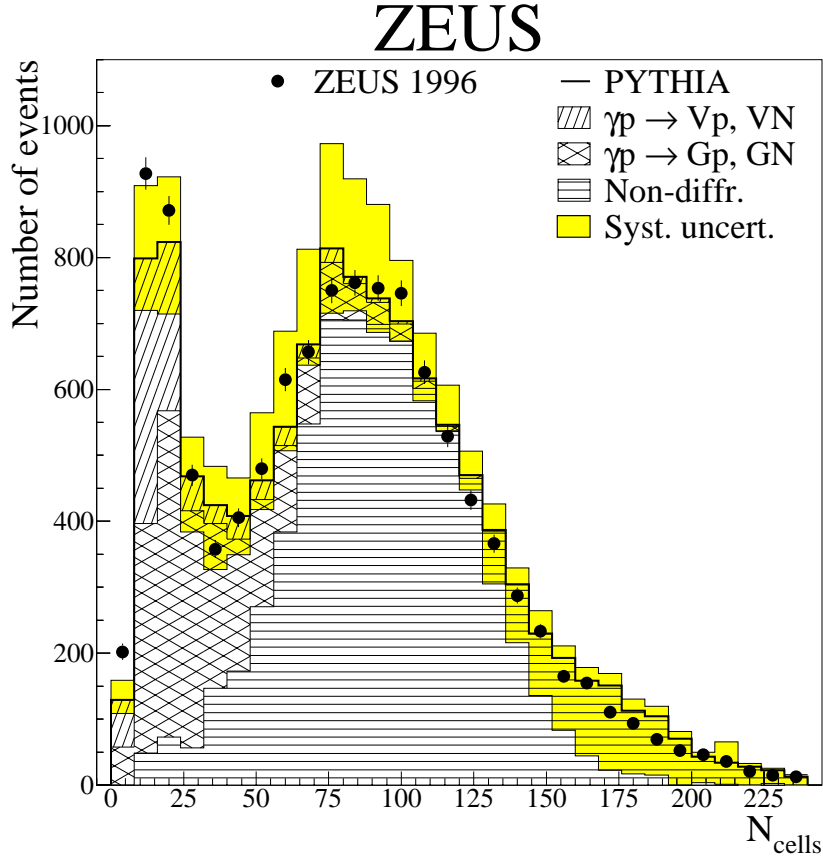
[2]This was worked out and implemented by Dirk Westphal.

Figure 4.26: The distribution of the number of hit calorimeter cells, N_{cells}, for data (full circles) and fitted total photoproduction sample (histogram with systematic uncertainty band). The fit is made to the M_X^{CAL} and N_{cells} distributions. Cumulative subprocess contributions are shown. The elastic and proton-dissociative, the photon-dissociative and double-dissociative, the soft and hard non-diffractive samples have been combined.

The error has been estimated to be 1%, giving

$$\Delta_{trigg} = 1.0^{+0.01}_{-0.00}. \tag{4.12}$$

4.13.2 Bremsstrahlung Overlays

The bremsstrahlung events comprise the largest background to photoproduction. The probability to have an event in which the bremsstrahlung event occurs simultaneously with a photoproduction event was estimated using randomly-triggered data.
The value of the correction factor is

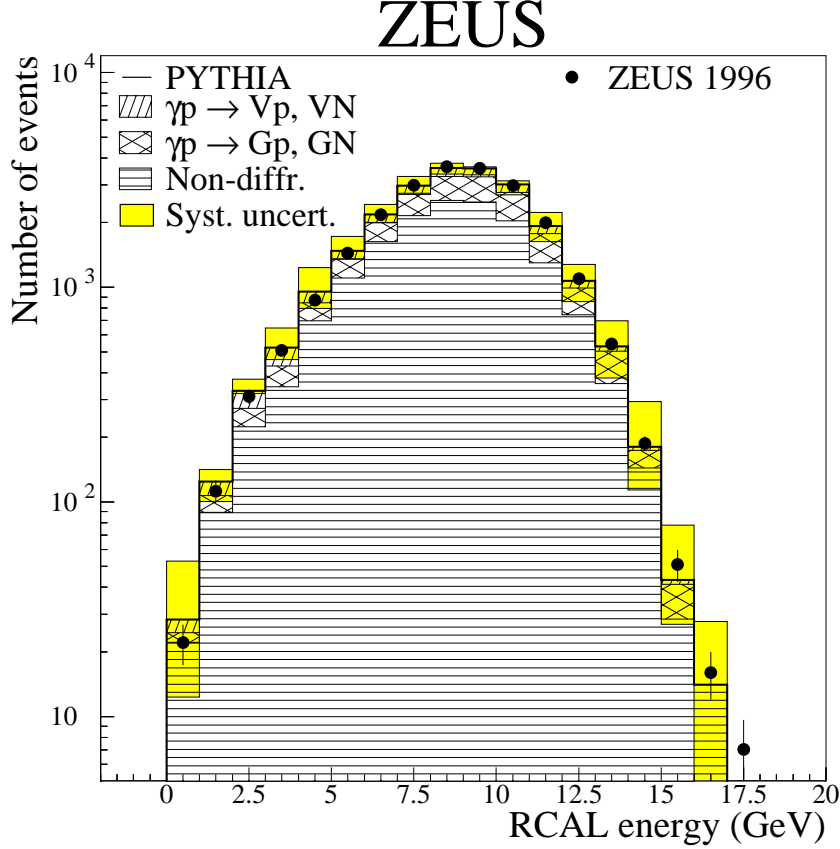$$\Delta_{BSO} = 1.043 \pm 0(stat.) \pm 0.002(syst.). \tag{4.13}$$

Figure 4.27: RCAL energy distribution for data (full circles) and fitted total photoproduction sample (histogram with systematic uncertainty band). The fit is made to the M_X^{CAL} and N_{cells} distributions. Cumulative subprocess contributions are shown. The elastic and proton-dissociative, the photon-dissociative and double-dissociative, the soft and hard non-diffractive samples have been combined.

4.13.3 LUMI-Photon Calorimeter Acceptance

An event which contains both the bremsstrahlung event and a proton–gas or a cosmic ray shower event can be treated as a genuine photoproduction event if the bremsstrahlung photon is not registered in the LUMI-photon calorimeter. This can happen since the calorimeter acceptance is 97% [153]. The effect of this background was estimated by comparing the number of bremsstrahlung events in the photoproduction sample which pass all cuts except that on the photon energy, $E_\gamma < 1$ GeV and events passing all the cuts. Since the photon energy is a rapidly falling distribution then the correction was attributed a 100% error.
The correction factor was found to be

$$\Delta_{\gamma acc} = 0.99 \pm 0.01. \tag{4.14}$$

Positron-residual gas bremsstrahlung outside the beam-pipe straight section is not expected to deposit a positron in the 35m tagger with $12 < E'_e < 16$ GeV. Therefore this process is not expected to contribute background to the data sample.

4.13.4 Radiative Corrections

The positron which initiates the γp interaction is subject to QED radiation. This radiation may occur in the initial or final state (ISR/FSR), or may lead to the initial-final state interference. These higher order QED processes change the event kinematics and thus measured cross sections. The influence of the QED radiation can be reduced by excluding events with hard initial-state photons. Since the ISR/FSR in photoproduction events is emitted predominantly at small angles with respect to the positron beam direction, the LUMI-photon calorimeter, placed at the angle $\theta = 0$ with respect to the positron beam direction, was used to veto events with hard radiation. Events with energy larger than 1 GeV in the photon calorimeter were rejected.

Residual effect of QED radiation on the measured cross section is calculated as a correction factor, Δ_{RAD}, which is the ratio of the Born ($\hat{\sigma}_{BORN}$) to the radiative ($\hat{\sigma}_{RAD}$) cross section

$$\Delta_{RAD} = \frac{\hat{\sigma}_{BORN}}{\hat{\sigma}_{RAD}}.$$

The size of the correction is measured by the deviation of Δ_{RAD} from unity. To calculate Δ_{RAD}, events without (N_{BORN}) and with (N_{RAD}) radiative effects were generated. The fraction of the Born cross section events with scattered electron energy E'_e within 12 GeV to 16 GeV is p_{BORN} and

$$\hat{\sigma}_{BORN} = p_{BORN} * \sigma_{BORN}.$$

For radiative events, the fraction p_{RAD} is calculated as a function of the upper limit on the photon energy, $E_{\gamma,cut}$, and on the photon emission angle, $\Theta_{\gamma,cut}$

$$p_{RAD}(E_{\gamma,cut}, \Theta_{\gamma,cut}) = \frac{N_{RAD}(12 < E'_e < 16, \overline{(E_\gamma > E_{\gamma,cut}, \Theta_\gamma < \Theta_{\gamma,cut}))}}{N_{RAD}}.$$

and

$$\hat{\sigma}_{RAD}(E_{\gamma,cut}, \Theta_{\gamma,cut}) = p_{RAD}(E_{\gamma,cut}, \Theta_{\gamma,cut}) * \sigma_{RAD}.$$

Finally, the radiative correction factor is

$$\Delta_{RAD}(E_{\gamma,cut}, \Theta_{\gamma,cut}) = \frac{p_{BORN} \cdot \sigma_{BORN}}{p_{RAD}(E_{\gamma,cut}, \Theta_{\gamma,cut}) \cdot \sigma_{RAD}}.$$

The correction was calculated for $E_{\gamma,cut} = 1$ GeV and for $\Theta_{\gamma,cut} = 0.54$ mrad. It was found to be

$$\Delta_{RAD} = 0.981 \pm 0.007(syst.). \tag{4.15}$$

The systematic error on the factor Δ_{RAD} was estimated taking into account the following:

- a different parameterisation of the low Q^2 cross section behaviour (the Brasse-Stein parameterisation [154]),

- different orders of the structure functions (GRV HO [155]),

- a comparison with analytic calculations of HECTOR 1.11 [138],

- variation of the photon-energy cut and the angular acceptance within the experimental uncertainties.

4.14   The Total Cross Section

The total photoproduction cross section is given by

$$\sigma_{TOT}^{\gamma p} = \frac{N(y)}{\mathcal{L}} \frac{1}{f_\gamma} \frac{1}{A_{35m}} \frac{1}{A_{UCAL}} \Delta_{TRIG} \; \Delta_{RAD} \Delta_{\gamma acc.} \Delta_{BSO}. \qquad (4.16)$$

Using the numbers obtained above the total cross section for the photoproduction at the photoproton centre–of–mass energy $W_{\gamma p} = 209$ GeV is [17]

$$\sigma_{TOT}^{\gamma p} = 174 \pm 1(stat.) \pm 13(syst.)\mu b. \qquad (4.17)$$

Figure 4.28 shows the total photoproduction cross section as a function of energy. This result is in a good agreement with the H1 measurement [15] at similar center–of–mass energy. The low energy data are also shown in the figure.

Since the present measurement was done under controlled conditions which resulted the reduction of systematic effects and is based on detailed studies of the photoproduction sub-processes it supersedes previous ZEUS measurements [16].

The ZEUS Collaboration performed an analysis of the low Q^2 data [54]. These data (BPC95) taken for $0.11 < Q^2 < 0.65$ GeV^2 were collected in a series of the shifted vertex runs in 1995. They were subsequently used in the extrapolation of the results down to $Q^2 = 0$. The extrapolation routine was based on the GVD model. The double differential cross section can be written as

$$\frac{d^2\sigma}{dydQ^2} = \Gamma \cdot (\sigma_T + \epsilon\sigma_L)$$

where $\Gamma = \alpha/2\pi(1+(1-y)^2)/(Q^2y)$ is the flux of virtual photons, $\epsilon = 2(1-y)/(1+(1-y)^2)$ is the photon polarisation and σ_T, σ_L are the cross sections for the interactions of the transverse and longitudinally polarised photons. In the case of BPC95 data ϵ ranges between 0.55 and 0.99. It should be noted that at HERA the cms energy is fixed so ϵ cannot be varied independently of x and Q^2. In other words the experiment delivers the measurement of $\sigma_T + \epsilon\sigma_L$. The extrapolation was performed using formula as in Eqn. 2.8 with ξ_V and the effective vector meson mass, M_0, determined from the data. In the extrapolation procedure the longitudinal cross section, σ_L was set to zero since on one hand the factor ξ_V is estimated [26] and measured [160] to be smaller than 1 and on the other hand the mass term in the GVD model formula for $\sigma_L^{\gamma^\star p}(W, Q^2)$ is small and about 0.2 for $Q^2 \leq 0.65$ GeV^2 and $M_0 \approx m_\rho$. The ZEUS BPC95 data were used to determine both the M_0 and the photoproduction cross section values. The total cross section at $W_{\gamma p}^2 = 212$ GeV was found to be $\sigma_{TOT}^{\gamma p} = 187 \pm 5(stat.) \pm 14(syst.)\mu b$. This value is compatible however somewhat higher than the reported direct measurement. The extrapolated cross sections for different values of $W_{\gamma p}$ are also above the Donnachie-Landshoff predictions. It
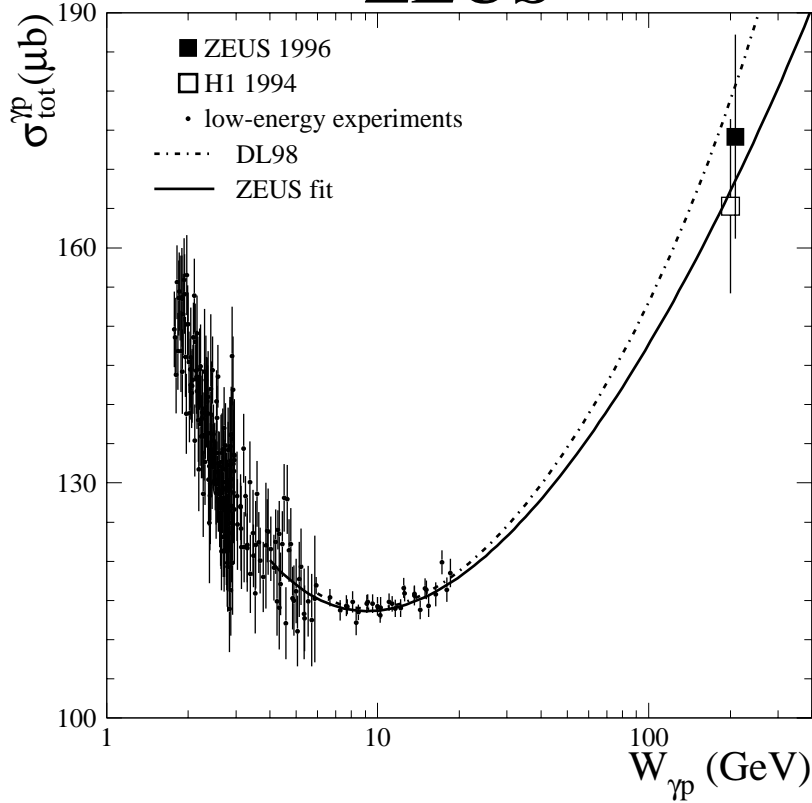
Figure 4.28: Photoproduction total cross section as a function of energy. The present measurement is shown as the full square. Also shown are low energy data (full circles), H1 published values (open squared), the DL98 (dash-dotted line) parameterisation and the ZEUS fit (solid line).

has to be stressed that the photoproduction cross sections obtained from the BPC95 data are not the measurements but the results of a phenomenologically motivated extrapolation.

As can be observed from Fig. 4.28 the ZEUS measurement at $W_{\gamma p} = 209$ GeV is also compatible with the DL98 parameterisation of the photoproduction cross section. An updated version of the Cudell et al. parameterisation [156] that uses a triple-pole term ($\log^2 s$) foresees a value of $\sigma_{TOT}^{\gamma p} = 176 \pm 4\mu b$ where the error is estimated from a variation of the fitted parameters.

The Golec-Biernat-Wüsthof model yields the value of $\sigma_{TOT}^{\gamma p} = 185\mu b$ [157] which is compatible with present measurement within the errors. This value was obtained for the quark mass of 150 MeV. If the quark mass is varied by ± 50 MeV then the GBW model predicts $174\mu b$ and $200\mu b$, respectively, for the total cross section for photoproduction.

The presented result is also compatible within the errors with a recent prediction of Pietrycki and Szczurek [158] who foresee, at $W_{\gamma p} = 209$ GeV, $\sigma_{TOT}^{\gamma p} = 188\mu b$ with the error of the order of

10%. The error was estimated taking into account possible variations within their model [159]. This model extends the GBW model to include explicitly the resolved photon component.

4.15   Interpretation of the Measurement

The energy dependence of the cross section can be parameterised in a way similar to [36] or [37]. In Figure 4.28 a fit of the form

$$\sigma_{TOT}^{\gamma p} = A \cdot W_{\gamma p}^{2\epsilon} + B \cdot W_{\gamma p}^{2\eta} \qquad (4.18)$$

is depicted as a solid line. The first term describes high energy behaviour of the cross section and is related to the pomeron intercept as $\alpha_{I\!P}(0) = 1 + \epsilon$. The second term is related to the reggeon exchange with the intercept of $\alpha_{I\!R}(0) = 1 - \epsilon$. The fit was performed to all the γp data [161] with $W_{\gamma p} > 4$ GeV and includes present measurement. In the fitting procedure the reggeon intercept was fixed to the value obtained by Cuddel et al. [37] $\eta = 0.358 \pm 0.015$. The parameters obtained in the fit are

$$A = 57 \pm 5\mu b; \qquad B = 121 \pm 13\mu b,$$

and

$$\epsilon = 0.100 \pm 0.012.$$

The resulting value of ϵ is in good agreement with $\epsilon = 0.093 \pm 0.002$ obtained in [37] from the analysis of hadronic data.

Good agreement of current $\sigma_{TOT}^{\gamma p}$ result with the parameterisations based mainly on the proton–proton and anti-proton–proton data indicates the universality of the high-energy dependence of the cross sections.

A fraction of the cross section is due to the hard non-diffractive interactions of the photon which are described by the direct and resolved photon components.

Using the optical theorem the total photoproduction cross section is, in VDM, related to the sum of the vector meson forward production amplitudes (see Eqn. 2.7). The sum of the exclusive photoproduction cross sections of ρ, ω and ϕ measured by ZEUS [64, 65, 66] is 111 ± 13 μb at the photon–proton centre–of–mass energy of 70 GeV. A dominant role of the ρ photoproduction is seen from the fact that its contribution is about 85% of the value. Interpolation between the present and the low energy measurements according to the above fit results a value of 139 ± 4 μb. Given the additional theoretical uncertainties in the VDM calculation of 111 μb these results are consistent.

As was mentioned earlier the total cross section for the photoproduction can be used to test the factorisation of the $\gamma\gamma$, γp and pp cross sections

$$\sigma_{TOT}^{\gamma\gamma} \cdot \sigma_{TOT}^{pp} = (\sigma_{TOT}^{\gamma p})^2.$$

The measurements of the $\gamma\gamma$ total cross sections was carried out by the L3 [162] and OPAL [163] Collaborations. OPAL measurements were performed at the cms energy of 68 GeV and 95 GeV and yielded $\sigma_{TOT}^{\gamma\gamma} = 439_{-41}^{+45}$ nb and $\sigma_{TOT}^{\gamma\gamma} = 464_{-62}^{+76}$ nb, respectively. The L3 measurements agree with those from OPAL for $W_{\gamma\gamma} < 100$ GeV. Using the present fit and Cuddel et al.

84

parameterisation of the *pp* cross sections one obtains values of $\sigma_{TOT}^{\gamma\gamma} = 436 \pm 26$ *nb* and $\sigma_{TOT}^{\gamma\gamma} = 468 \pm 30$ *nb* at the centre-of-mass energy of 68 and 95 GeV, respectively, in good agreement with the LEP results. This confirms the cross section factorisation.

The L3 Collaboration measured the $\gamma\gamma$ cross section also at $W_{\gamma\gamma} = 120.4$ GeV and found $\sigma_{TOT}^{\gamma\gamma} = 572.0 \pm 3.3(stat.) \pm 53.0(exp.\ syst.) \pm 89.0(MC\ syst.)$ *nb* and $\sigma_{TOT}^{\gamma\gamma} = 734.1 \pm 8.7(stat.) \pm 102.0(exp.\ syst.) \pm 202.0(MC\ syst.)$ *nb* at $W_{\gamma\gamma} = 158.7$ GeV. The luminosity measurement gives an additional uncertainty of $\pm 5\%$. The interpolation from the present $\sigma_{TOT}^{\gamma p}$ measurement yields 491 ± 35 *nb* and 521 ± 43 *nb*, respectively. The interpolation results and the L3 measurements are consistent with factorisation within the large systematic uncertainties quoted by the L3 Collaboration.

Chapter 5

Summary and Outlook

The experimental part of this thesis describes the measurement of the total photoproduction cross section done with the ZEUS detector at HERA. At present the HERA measurements are the highest centre-of-mass energy measurements of the total cross section for photoproduction. The cms energy is about one order of magnitude higher than that for the fixed target experiments. The present measurement was carried out at the photon–proton centre–of–mass energy of 209 GeV and yielded $\sigma_{TOT}^{\gamma p} = 174 \pm 1(stat.) \pm 13(syst.)$ μb.

This value agrees with the H1 Collaboration measurement and is compatible with earlier ZEUS Collaboration measurement and the ZEUS low-Q^2 data extrapolation to the photoproduction limit, $Q^2 = 0$.

The energy dependence of the total γp cross section is well reproduced by the Regge theory motivated fit with the pomeron intercept value of $\alpha_{I\!P}(0) = 1.100 \pm 0.012$. The fitted pomeron intercept value agrees with the values obtained mainly from the analysis of the pp and $\bar{p}p$ data and from the analyses of different soft processes measured at HERA. Good agreement of the present result with the different parameterisations based on hadron–hadron collision data indicates the universality of the high-energy dependence of the cross sections.

A sizable fraction of the cross section is due to hard processes calculable in perturbative QCD. The cross section when extrapolated to lower centre–of–mass energies shows a reasonable agreement with the Vector Meson Dominance model predictions.

The present result used together with the parameterisation of the pp cross sections and the measurements of the $\gamma\gamma$ cross sections shows the factorisation at the level of the cross sections.

Further studies of the photoproduction in the accelerator regime can be performed using planned extension of the RHIC complex [164, 165] by addition of an electron accelerator.

The Electron Ion Collider (EIC) is foreseen as a mean to study QCD at high densities of partons and large values of color fields. Its physics programme was extensively reviewed in a series of workshops [164, 166]. One should note that similar studies were earlier preformed for the nuclear beams option at HERA [167].

In particular, the EIC is expected to deliver relevant data on the spin and momentum distributions of partons inside hadrons, on the origin of confinement and evolution of quarks and gluons into hadrons, and on the relation between properties of atomic nuclei and their partonic content. The electron–ion collisions will allow the study of the many-body aspects of QCD such as the

saturation of partonic matter and the long range correlations between the partons. Also, the propagation of quarks through the nuclear matter and the dynamics of high-energy interactions of small colour singlet systems (for example J/Ψ) with nuclear media can be studied.

At EIC the electron beam will be collided with beams of protons or light or heavy ions. The lepton beam energy will range between 5 and 10 GeV. Also, the ion beam energy will be tunable spanning the 15 to 100 GeV/nucleon interval. The proton beam can have energy between 50 and 250 GeV. Both the electron and hadron beams can be polarised. The accelerator luminosity is foreseen to reach 10^{33} cm^{-2}s^{-1}.

A layout for the Interaction Region and a generic detector was proposed [168, 19] during the 2nd eRHIC Workshop in 2000. The design criteria took into account the following:

- a common detector for ep, eA, pp and pA collisions,

- a "whole" ep and eA reconstruction,

- a precise luminosity monitoring and control of radiative corrections,

- a good detector performance in the fragmentation regions,

- a minimal interference with the existing RHIC IR optics,

- the use of the RHIC magnet lattice in the hadron spectrometer design,

- a possibility of a polarised electron beam.

The above items lead to the design of a generic detector which is divided into three parts outlined below. The detector uses the existing RHIC magnet lattice as parts of the hadron and lepton spectrometers. An early separation of the lepton and hadron beams is achieved by means of a dedicated magnet which also play role of a spin rotator. In the proton/ion direction
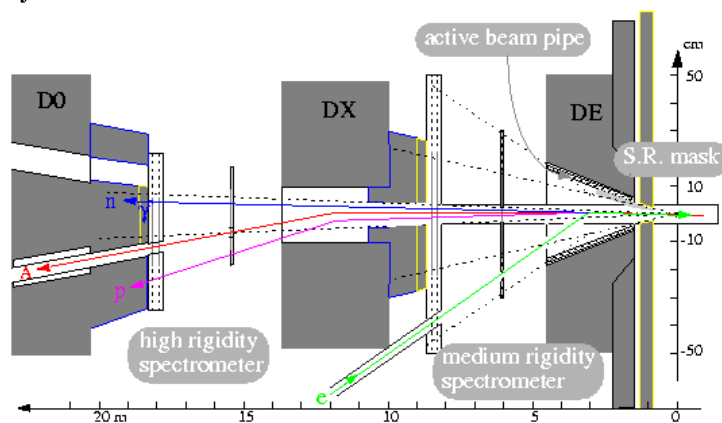

Figure 5.1: A schematic view of the proton/nucleus side of the generic detector proposed for the eRHIC. From [168].

an extended spectrometer was postulated. Its schematic view is shown in Figure 5.1. The spectrometer consists of:

- the roman pots system: to study diffractive scattering,

- the high magnetic rigidity spectrometer equipped with an electromagnetic calorimeter for the nuclear $\gamma(\pi^0)$ measurement, the hadronic calorimeter to register the nucleus evaporation neutrons, and for the identification of protons and heavier fragments, the tracking system for measuring the evaporation protons and heavier fragments,

- the medium magnetic rigidity spectrometer with an electromagnetic calorimeter, the hadronic calorimeter to measure wounded neutrons, protons and for the identification of heavier fragments, the tracking system to measure charged particles and fragments,

- the rapidity gap trigger to close the acceptance for charged particles and to tag diffractive events.

The central detector (called the "parton side" in [168]) consists of the μ-vertex detector, the tracking chamber backed by the EM calorimeter and the SpaCal [169] type end-caps. In the lepton direction a photon counter for the luminosity and radiative correction control is foreseen. It will be used as a fast electron beam monitoring and diagnostic tool. The instrumented beam-pipe will be used to tag the scattered electron.

A schematic view of the electron side is shown in Fig. 5.2. The existing RHIC magnets are DX and $D0$. The beam separation/spin rotator dipole magnet is marked by DE.
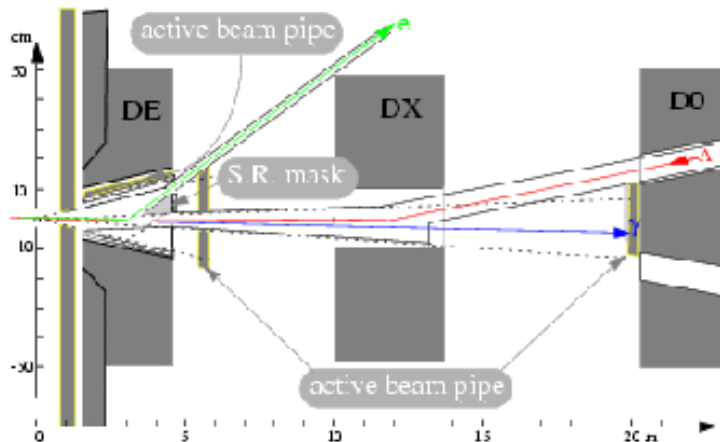

Figure 5.2: A schematic view of the electron side of the generic detector proposed for the eRHIC. From [168].

The photoproduction measurement will be based on the same principle as at HERA. This means that both methods tagged and untagged can be used. The experiment will trigger on events where the exchanged photon virtuality, Q^2, is small. In Figure 5.3 the correlation between the electron exit position and its energy in tagged photoproduction events is shown. A clear linear dependence is visible for a wide range of the electron energies. This shows the importance
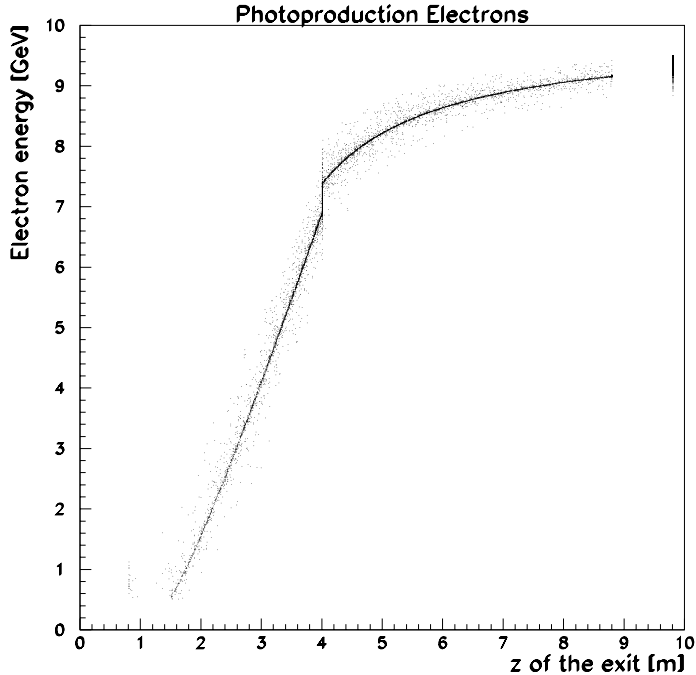
Figure 5.3: The scattered electron energy–exit position correlation. The z of the exit position is measured from the nominal IP. From [19].

of the DE magnet for the scattered electron energy analysis. The electron exit position determines its energy. The width of the correlation band is due to the variation of the vertex position. The influence of this effect can be easily diminished by imposing the cuts on the vertex position determined with the μ-vertex device and the tracking chamber. The exit position of the electron can be measured using an active beam-pipe [170]. A typical solution would be to instrument the beam-pipe with a layer of optical fibers. One should note, however, that the correlation in Fig. 5.3 will broaden in real experimental environment. This broadening will be due to the electron beam angular spread not included in the simulation shown in Fig. 5.3. Therefore, it will be worth equipping the active beam-pipe with some means of the scattered electron energy measurement (a compact calorimeter for example).

The nuclear beam option for eRHIC enables a systematic study of various aspects of γA interactions. In particular, the nucleus can serve as a femto-detector [168]. It will be interesting to distinguish experimentally between the long- and short-range components of the photon. If the photon interacts only directly with one nucleon then the presence of other nucleons should not matter. If the hadronic component is build up early enough then the interactions inside the nucleus should be shadowed. In the case of a pure short-range interaction the incident photon can interact with any nucleon with equal chance so the total cross section will be

$$\sigma(A) \sim A \cdot \sigma(1),$$

89

where $\sigma(1)$ is calculated as a weighted average of the total cross section on protons and neutrons. In the case of a long-range interaction, the primary interaction of the photon will be with the nucleons on the "photon side" of the nucleus. The nucleons which are placed deeper inside the nucleus will add to the secondary interactions. Thus they will be screened from the hadronic structure of the incoming photon. This means that

$$\sigma(A) < A \cdot \sigma(1).$$

Since the surface density of nucleons is proportional to $A^{2/3}$ then the total cross section dependence should be similar. This expectation was first pointed out by Stodolsky [171] in the framework of the VDM. Later, Gribov [172], Brodsky and Pumplin [173] arrived to similar conclusions on more general grounds.

Experimentally the shadowing effects are estimated in terms of the effective nucleon number, A_{eff}.

$$\frac{A_{eff}}{A} = \frac{\sigma_{\gamma A}}{Z\sigma_{\gamma p} + (A - Z)\sigma_{\gamma n}}$$

where $\sigma_{\gamma p}$ and $\sigma_{\gamma n}$ are the photoproduction cross sections on the proton and neutron, respectively. There exist variations of the above formula in which the denominator is replaced by either the average photon–nucleon cross section or the cross section deduced from the photon–deuteron data. The measurements [174, 175, 176, 177, 178] show that A_{eff} is smaller than unity which demonstrates the presence of shadowing effects. They appear to be photon energy dependent and set up for the photon energy around 2 GeV. One should note that the measurements were carried out for nuclei ranging between carbon and uranium and were performed for rather small W values - the photon energy below 40 GeV.

Obviously, the study of shadowing effects will be extended to a whole $x - Q^2$ plane to investigate in detail the process limiting the growth of F_2 structure function. For a review of different models cf. [179].

One should note that the nucleus-side of the detector will enable the tagging of the nucleus final state. This will make feasible an on-line experimental triggering on events due to the coherent and non-coherent processes. In particular, a wide domain of diffraction from nuclei can be investigated. The analysis of events from a nuclear target characterised by the large rapidity gap will allow the determination of the pomeron structure and its comparison to the one observed in processes from a free nucleon. The study of diffractive vector meson production will serve as a test of the color transparency effect which predicts a non-shadowed cross section i.e. $\sigma \sim A$. Moreover, all the studies can be performed in correlation with the nucleus final state.

Investigation of the photon showed that "*the photon has a rich structure that makes it far more interesting in its own right than as a mere probe of the charge distribution of other particles*" [26]. With advent of the electron–ion accelerator we can learn more about this structure and its impact on our understanding of the matter.

Acknowledgments

Bibliography

[1] V. Baronne and E. Predazzi, High-Energy Particle Diffraction, Springer-Verlag, ISBN: 3-540-42107-6 and references therein.

[2] A. Donnachie and P.V. Landshoff, Phys. Lett. **B296** (1992) 227.

[3] W. Heisenberg, Z. Phys. **(**133) (1952) 65.

[4] AKENO (Agasa) Collab., M. Honda et al., Phys. Rev. Lett. **70** (1993) 525.

[5] Fly's Eye Collab., R. M. Baltrusaitis et al., Phys. Rev. Lett. **52** (1984) 1380.

[6] M. Froissart, Phys. Rev. **123** (1961) 1053;
A. D. Martin, Phys. Rev. **129** (1963) 1432.

[7] COMPETE Collab., J. R. Cudell et al., Phys. Rev. **D65** (2002) 074024.

[8] I. Ya. Pomeranchuk, Zh. Exp. Teor. Phys. **34** (1958) 725.

[9] T. Regge, Nuovo Cimento **14** (1959) 951;
T. Regge, Nuovo Cimento **18** (1960) 947.

[10] P.D.B. Collins, *An Introduction to Regge Theory and High Energy Physics*, Cambridge University Press (1977).

[11] V. Gribov, Sov. Phys. JETP **8** (1961) 40;
V. Gribov, Sov. Phys. JETP **14** (1962) 478

[12] L. Lukaszczuk and B. Nicolescu, Lett. Nuovo Cim. **8** (1973) 405;
D. Joyson, E. Leader, C. Lopez and B. Nicolescu, Nuovo Cim. **A30** (1975) 34

[13] E. M. Levin and L. L. Frankfurt, JETP lett. **2** (1965) 65;
H. J. Lipkin and F. Scheck, Phys. Rev. Lett **16** (1966) 71.

[14] J. J. Sakurai, Ann. Phys. (NY) **11** (1960) 1;
J. J. Sakurai, Phys. Rev. Lett **22** (1969) 981.

[15] H1 Collab., S. Aid et al., Z. Phys. **C69** (1995) 27.

[16] ZEUS Collab., M. Derrick et al., Phys. Lett. **B293** (1992) 465;
ZEUS Collab., M. Derrick et al., Z. Phys. **C63** (1994) 391.

[17] ZEUS Collab., S. Chekanov et al., Nucl. Phys. **B627** (2002) 3.

[18] J. Chwastowski and J. Figiel, Photoproduction at HERA, hep-ex/0311044, submitted to Physics of Particles and Nuclei.

[19] E. Barrelet, J. Chwastowski and M. W. Krasny, Interaction Region Compromises, In Proc. of the 2nd eRHIC Workshop, New Haven, April 6–8, 2000, BNL-52592; presented by J. Chwastowski at the Workshop.

[20] J. Chwastowski, Physics Results and Future Plans of ZEUS Experiment, presented at 12th Int. Seminar on High Energy Physics, QUARKS '2002, 1-7 June 2002, Novgorod the Great, Russia.

[21] J. Chwastowski, Aspects of eA Interactions at HERA, presented during the Workshop on Physics at HERA as eA Collider, 25–26 May 1999, DESY, Hamburg, Germany.

[22] F. J. Gilman, Phys. Rev. **129** (1968) 1365.

[23] L. N. Hand, Phys. Lett. **B129** (1963) 1834.

[24] V. Gribov et al., Sov. Phys. JETP**14** (1962) 1308; K. F. v. Weizsäcker, Z. Phys **88** (1934) 612; E. J. Williams, Phys. Rev. **45** (1934) 729.

[25] A. B. Kaidalov, hep-ph/0103011.

[26] T.H. Bauer et al., Rev. Mod. Phys. **50** (1978) 261.

[27] J. J. Sakurai and D. Schildknecht, Phys. Lett. **B40** (1972) 121.

[28] B. Gorczyca and D. Schildknecht, Phys. Lett. **B47** (1973) 71.

[29] H. Fraas, B. J. Read and D. Schildknecht, Nucl. Phys. **B86** (1975) 346.

[30] D. Schildknecht and H. Spiesberger, hep-ph/9707477; D. Schildknecht, Acta Phys. Pol. **B11** (1997) 2453.

[31] H1 Collab., S. Aid et al., Nucl Phys. **B470** (1996) 3; H1 Collab., C. Adloff et al., Nucl. Phys. **B497** (1997) 3.

[32] H1 Collab., T. Ahmed et al., Nucl. Phys. **B429** (1994) 477.

[33] ZEUS Collab., M. Derrick et al., Z. Phys. **C72** (1996) 399; ZEUS Collab., J. Breitweg et al., Phys. Lett. **B407** (1997) 432.

[34] ZEUS Collab., M. Derrick et al., Phys. Lett. **B315** (1993) 481.

[35] G. Cvetic, D. Schildknecht, B. Surrow and M. Tentyukkov, E. Phys. J. **C20** (2001) 77.

[36] A. Donnachie and P.V. Landshoff, Phys. Lett. **B437** (1998) 408.

[37] J. R. Cudell et al, Phys. Rev. **D61** (2000) 034019, Erratum-ibid. **D63** (2001) 059901.

[38] Particle Data Group, K. Hagiwara et al., Phys. Rev. **D66** (2002) 010001.

[39] H. Abramowicz, E. Levin, A. Levy and U. Maor, Phys. Lett. **B269** (1991) 465.

[40] H. Abramowicz, E. Levy, DESY-97-251.

[41] M.M. Block et al., Phys. Rev. **D60** (1999) 054024;
M.M. Block, F. Halzen and T. Stanev, Phys. Rev. **D62** (2000) 077501.

[42] M.M. Block et al., Phys. Rev. **D41** (1990) 978.

[43] M. M. Block and R. N. Cahn, Rev. Mod. Phys. **57** (1985) 563.

[44] M. M. Block and A. B. Kaidalov, Phys. Rev. **D64** (2001) 076002.

[45] J. Kwieciński and B. Badełek, Z. Phys. **C43** (1989) 251.

[46] B. Badełek and J. Kwieciński, Phys. Lett. **B295** (1992) 263.

[47] A. Capella et al., Phys. Lett. **B337** (1994) 358.

[48] A. Kaidalov, L. Ponomarev, K. A. Ter-Martirosyan, Sov. J. Nucl. Phys. **44** (1986) 468.

[49] K. Golec-Biernat and M. Wüsthoff, Phys. Rev. **D59** (1998) 014017.

[50] K. Golec-Biernat, Habilitation Thesis, IFJ rep. 1877/PH.

[51] A. M. Staśto, K. Golec-Biernat ad J. Kwieciński, Phys. Rev. Lett. **86** (2001) 596.

[52] H1 Collab., S. Aid et al., Nucl. Phys. **B470** (1996) 399;
H1 Collab., C. Adloff et al., Nucl. Phys. **B497** (1997) 3.

[53] ZEUS Collab., M. Derrick et al., Z. Phys. **C72** (1996) 399.

[54] ZEUS Collab., M. Derrick et al., Eur. Phys. J. **C7** (1999) 609.

[55] K. Golec-Biernat and M. Wüsthoff, Phys. Rev. **D60** (1999) 114023.

[56] H1 Collab., C. Aldloff et al., Z. Phys. **C76** (1997) 613.

[57] ZEUS Collab., J. Breitweg et al., Eur. Phys. J. **C6** (1999) 43.

[58] E. Kogan, Ph. D. thesis, Weizmann Institute, Rehovot, Israel (unpublished).
See also [26] p. 270.

[59] H. Alvensleben et al., Phys. Rev. Lett. **30** (1973) 328.

[60] B. L. Ioffe, Phys. Lett. **B30** (1969) 123;
B. L. Ioffe, V. A. Khoze and L. N. Lipatov, Hard Proccesses, vol 1 (1984) 155.

[61] G. A. Schuler and T. Sjöstrand, Nucl. Phys. **B407** (1993) 529;
G. A. Schuler and T. Sjöstrand, CERN-TH 6796/93;
C. Friberg and T. Sjöstrand, J. High Energy Phys. **09** (2000) 10.

94

[62] M. Krawczyk, A. Zembrzuski and M. Staszel, Phys. Rep. **345** (2001) 265.

[63] H. Abramowicz and A. Caldwell, Rev. Mod. Phys. **71** (1999) 1275. C. Friberg and T. Sjöstrand, J. High Energy Phys. **09** (2000) 10.

[64] ZEUS Collab., J. Breitweg et al., Eur. Phys. J. **C2** (1998) 247;
ZEUS Collab., M. Derrick et al., Z. Phys. **C69** (1995) 39.

[65] ZEUS Collab., M. Derrick et al., Z. Phys. **C73** (1996) 73.

[66] ZEUS Collab., M. Derrick et al., Phys. Lett. **B377** (1996) 259.

[67] H1 Collab., S. Aid et al., Nucl. Phys. **B463** (1996) 3.

[68] ZEUS Collab., M. Derrick et al., Z. Phys. **C73** (1997) 253.

[69] OMEGA Photon Collab., D. Aston et al., Nucl. Phys. **B209** (1982) 56;
W. G. Jones et al., Phys. Rev. Lett. **21** (1968) 586;
C. Berger et al., Phys. Lett. **39B** (1972) 659;
SBT Collab. J. Ballam et al. Phys. Rev. **D5** (1972) 545;
G. E. Gladding et al., Phys. Rev. **D8** (1973) 3721.

[70] P. Fleischmann for H1 Collab., to appear in proceedings of DIS 2003, 23 -27 April 2003, St. Petersburg, Russia.

[71] H1 Collab., C. Aldoff et al., Phys. Lett. **B483** (2000) 23.

[72] H1 Collab., Paper submitted to XXI int. Europhysics Conference on High Energy Physcis, July 17-23 2003, Aachen, abstract 108.

[73] ZEUS Collab., S. Chekanov et al., Eur. Phys. J. **C24** (2002) 345.

[74] M. Ryskin, Z. Phys. **C57** (1993) 89.

[75] M. Ryskin et al., Z. Phys. **C76** (1997) 231.

[76] ZEUS Collab., J. Breitweg et al., Phys. Lett. **B437** (1998) 432.

[77] L. Frankfurt, M. McDermott and M. Strickman, J. High Energy Phys. **02** (1999) 002.

[78] A.D Martin, M.G. Ryskin and T. Teubner, Phys. Lett. **B454** (1999) 339.

[79] T.J. Chapin et al., Phys. Rev. **D31** (1985) 17.

[80] H1 Collab., C. Adloff et al., Z. Phys. **C74** (1997) 221.

[81] ZEUS Collab., J. Breitweg et al., Z. Phys. **C75** (1997) 421.

[82] G. Ingelmann and P. E. Schlein, Phys. Lett. **B152** (1985) 256.

[83] J. D. Bjorken, Phys. Rev. **D47** (1993) 101.

[84] ZEUS Collab., M. Derrick et al., Phys. Lett. **B356** (1995) 129.

[85] H1 Collab., T. Ahmed et al., Nucl. Phys. **B435** (1995) 3.

[86] H1 Collab., C. Adloff et at., Eur. Phys. J. **C6** (1999) 421.

[87] ZEUS Collab., J. Breitweg et al., Eur. Phys. J. **C5** (1998) 45.

[88] H1 Collab., contribution to International Europhysics Conference on High Energy Physics, EPS03, July 17-23, 2003, Aachen, abstract 087.

[89] ZEUS Collab., M. Derrick et al., Phys. Lett. **B369** (1996) 55.

[90] H1 Collab., C. Adloff et al., Eur. Phys. J. **C24** (2002) 517.

[91] H. N. Chehimine and D. Zeppenfeld, MAD/PH/814 (1994).

[92] CDF Collab., F. Abe et al., Phys. Rev. Lett. **74** (1995) 855.

[93] D0 Collab., S. Abachi et al., Phys. Rev. Lett. **76** (1996) 734.

[94] ZEUS Collab., S. Chekanov et al., Eur. Phys. J. **C26** (2003) 389.

[95] J. R. Forshaw and G. Poludniowski, Eur. Phys. J. **C26** (2003) 411.

[96] J. Bartels et al., Phys. Lett. **B375** (1996) 301;
D. Yu. Ivanov et al., Phys. Lett. **B478** (2000) 101, Erratum ibid. **B348** (2001) 295.

[97] ZEUS Collab., J. Breitweg et al., Eur. Phys. J. **C14** (2000) 213.

[98] R. Enberg, L. Motyka and G. Poludniowski, Acta Phys. Pol. **B33** (2002) 3511.

[99] M. Klasen, Rev.Mod.Phys. **74** (2002) 1221.

[100] JADE Collab., W. Bartel et al., Z. Phys. **C24** (1984) 231;
TASSO Collab., M. Althoff et al., Z. Phys. **C31**(1986) 527;
PLUTO Collab., C. Berger et al., Nucl. Phys. **B281** (1987) 365;
TPC/Two-Gamma Collab., H. Aihara et al., Z. Phys. **C34**(1987) 1;
OPAL Collab., G. Abbiendi et al., Eur. Phys. J. **C18** (2000) 15;
OPAL Collab., K. Ackerstaff et al., Phys. Lett **B411** (1997) 387;
OPAL Collab., K. Ackerstaff et al., Z. Phys. **C74** (1997) 33;
OPAL Collab., K. Ackerstaff et al., Phys. Lett. **B412** (1997) 225;
OPAL Collab., K. Akers et al., Z. Phys. **C61** (1994) 199;
DELPHI Collab., P. Abreu et al., Z. Phys. **C69** (1996) 223;
L3 Collab., M. Acciari et al., Phys. Lett. **B447** (1999) 147;
L3 Collab., M. Acciari et al., Phys. Lett. **B436** (1998) 403.

[101] H1 Collab., C. Adloff et al., Eur. Phys. J. **C29** (2003) 497.

[102] ZEUS Collab., S. Chekanov et al., Phys. Lett. **B560** (2003) 7.

[103] M. Glück, E. Reya and A. Vogt, Phys. Rev., **D45** (1992) 3986;
M. Glück, E. Reya and A. Vogt, Phys. Rev., **D46** (1992) 1973.

[104] P. Aurenche, J. P. Guillet and M. Fontanaz, Z. Phys. **C64** (1994) 621.

[105] CTEQ Collab., H. L. Lai et al., Eur. Phys. J. **C12** (2000) 375.

[106] A. D. Martin, R. G. Roberts, W. J. Stirling and R. S. Thorne, Eur. Phys. J. **C14** (2000) 133.

[107] S. Bethke, J. Phys. **G26** (2000) R27;
S. Bethke, hep-ex/0211012.

[108] ZEUS Collab., J. Breitweg et al., Phys. Lett. **B507** (2001) 70;
ZEUS Collab., S. Chekanov et al., Phys. Lett. **B547** (2002) 164.

[109] H1 Collab., C. Adloff et al., Eur. Phys. J. **C19** (2001) 289.

[110] CDF Collab., T. Affolder et al., Phys. Rev. Lett. **88** (2002) 042001.

[111] ZEUS Collab., M. Derrick et al., Phys. Lett. **B348** (1995) 665.

[112] H1 Collab., C. Adloff et al., Eur. Phys. J. **C25** (2002) 13.

[113] ZEUS Collab., S. Chekanov et al., Eur. Phys. J. **C23** 2002 615.

[114] S. Frixione and G. Ridolfi, Nucl. Phys. **B507** (1997) 4007;
S. Frixione, Nucl. Phys. **B507** (1997) 295.

[115] A Proposal for a Large Electron - Proton Colliding Beam Facility at DESY, DESY HERA 81-10 (1981);
B. H. Wiik, Electron - Proton Colliding Beams, The Physics Programme and the Machine, Proc. 10th SLAC Summer Institute, ed. A. Mosher, 233 (1982).

[116] ZEUS Collaboration, The ZEUS Detector, Technical Proposal, (1986);
The ZEUS Detector, Status Report 1993, ed. U. Holm, DESY (1993);
http://www-zeus.desy.de/bluebook/bluebook.html.

[117] B. Foster et al., NIM **A338** (1993) 254.

[118] M. Derrick et al., NIM **A309** (1993) 77;
A. Berstein et al., NIM **A336** (1993) 23;
A. Anderson et al., NIM **A309** (1991) 101.

[119] H. Bethe and W. Heitler, Proc. Roy. Soc. **A146** (1934) 83.

[120] K. J. F. Gaemers, M. van der Horst, Nucl. Phys. **B316** (1989) 269;
A. A. Akhundov, D. Yu. Bardin, L. V. Kalinovskaya, Z. Phys **C51** (1991) 557;
M. van der Horst, Nucl. Phys **B347** (1990) 149;
M. van der Horst, Phys. Lett. **B244** (1990) 107.

[121] J. Andruszków et al., DESY 92-066 (1992);
J. Andruszków et al., Acta Phys. Polon. **B32** (2001) 2025.

[122] G. L. Kotkin, V. G. Serbo, A. Schiller, Int. J. Mod. Phys. **A7** (1992) 4707 and references therein.

[123] W. H. Smith et al., The ZEUS Trigger System, ZEUS Note 89-094 (1989);
H. A. J. R. Uijterwaal, The Golobal Second Level Trigger, Ph. D. thesis, University of Amsterdam (1992);
C. Youngman, The ZEUS data Acquisition System, DESY-92-150A (1992).

[124] F. Bernard, R. S. Orr, S. Polenz, D. Simmons, ZEUS Note 95-164.

[125] Glasgow-Sheffield-DNPL Collab., T. A. Armstrong et al., Phys. Rev. **D5** (1972) 1640;
Glasgow-Sheffield-DNPL Collab., T. A. Armstrong et al., Nucl. Phys. **B41** (1972) 445.

[126] J. Ballam et al., Phys. Rev. Lett. **21** (1968) 1544.

[127] I. F. Ginzburg et al., NIM **A219** (1984) 5.

[128] V. I. Telnov, NIM **A294** (1990) 72.

[129] SLAC-Tufts-UC Berkeley Collab., J. Ballam et al., Phys. Rev. Lett. **23** (1969) 498.

[130] SLAC-UC Berkeley-Tufts Collab., J. Ballam et al., Phys. Rev. **D5** (1972) 545.

[131] SLAC-UC Berkeley Collab., H. H. Bingham et al., Phys. Rev. **D8** (1973) 1277.

[132] G. Levman, ZEUS-Note 95-088.

[133] A. I. Lebedev, In. Proc. Workshop on Physics at HERA, ed. W. Buchmüller and G. Ingelman, 1991, vol. 1, p. 613.

[134] L. Adamczyk, private communication.

[135] B. Holzer, Private communication.

[136] K. Piotrzkowski and L. Suszycki, In Proc. Worskhop on Physics at HERA, ed. W. Buchmüller and G. Ingelman, 1991, vol.3, p. 1463.

[137] A. Kwiatkowski, H. Spiesberger and H.J. Möhring, Computer Phys. Commun. **69** (1990) 155;
H. Spiesberger, Heracles 4.6 Manual, `http://www.desy.de/ hspiesb/heracles.html`

[138] A. Arbuzov, D. Bardin, J.Bluemlein, P. Christova, L. Kalinovskaya and T. Riemann, Comp. Phys. Commun. **94** (1996) 128.
Hector 1.10 Manual, DESY **95-185**, hep-ph/9511434.

[139] H. Spiesberger et al., Radiative Corrections at HERA, in Proc. of Physics at HERA, Hamburg 1991, p.798.

[140] T. Sjöstrand, PYTHIA 5.7, hep-ph-/9508391;
T. Sjöstrand, Computer Phys. Commun. **82** (1994) 74.

[141] G. Marchesini and B. R. Webber, Nucl. Phys. **B238** (1984) 1;
B. R. Weber, Nucl. Phys. **B238** (1984) 492;
G. Marchesini and B. R. Webber, Nucl. Phys. **B310** (1988) 461;
G. Marchesini et al., Computer Phys. Commun. **67** (1992) 465;
G. Marchesini et al., HERWIG 5.9, hep-ph/9607393.

[142] T. Sjöstrand and M. van Zijl, Phys. Rev. **D36** (1987) 2019;
UA5 Collab., R. E. Ansorge et al., Z. Phys **C43** (1989) 357.

[143] D. Amati and G. Veneziano, Phys. Lett. **B83** (1979) 87;
G. Marchesini, L. Trentadue and G. Veneziano, Nucl. Phys. **B181** (1981) 335.

[144] B. Webber, Nucl. Phys. **B238** (1984) 492.

[145] UA5 Collab., G. J. Alner et al., Nucl. Phys **B291** (1987) 445.

[146] J. Mainusch, Ph.D. Thesis Hamburg University, 1995.

[147] CTEQ Collab., H. L. Lai et al., Phys. Rev. **D55** (1997) 1280.

[148] R. Brun et al., GEANT3, CERN DD/EE/84-1 (1987) with later improvements.

[149] R. Kose, Private communication.

[150] K. Olkiewicz, Private communication.

[151] ZEUS Collaboration, "The ZEUS Detector", Status Report 1993, DESY 1993, Chapter 17.6: ZEUS Monte Carlo Program MOZART.

[152] ZGANA user manual and documentation, http://www.nikhef.nl/pub/experiments/zeus/zgana.

[153] K. Olkiewicz, Private communication.

[154] F.W. Brasse et al., Nucl. Phys. **B110** (1976) 413;
SLAC E61 Collaboration, S. Stein et al., Phys. Rev. **D12** (1975) 1884.

[155] M. Glück, E. Reya and A. Vogt, Z. Phys., **C48** (1990) 471;
M. Glück, E. Reya and A. Vogt, Z. Phys, **C53** (1992) 127;
M. Glück, E. Reya and A. Vogt, Z. Phys., **C67** (1995) 433.

[156] COMPETE Collab., J. R. Cudell et al., Phys. Rev. Lett. **89** (2002) 201801;
see also http://nuclth02.phys.ulg.ac.be/compete/predictor.html/2003_08_08/index.html

[157] K. Golec-Biernat, Private Communication.

[158] T. Pietrycki and A. Szczurek, Private Communication.

[159] T. Pietrycki and A. Szczurek, Eur.Phys.J. **C31** (2003) 379.

[160] ZEUS Collab., paper 792 submitted to ICHEP98 Vancouver, July 1998.

[161] HERA and Compass Groups, S. I. Alekhin et al., CERN-HERA-8701 (1987).

[162] L3 Collab., M. Acciarri et al., Phys. Lett. **B519** (2001) 33.

[163] OPAL Collab., G. Abbiendi et al., Eur. Phys. J. **C14** (2000) 199.

[164] I. Ben – Zvi, J. Kewisch, J. Murphy and S. Peggs, Accelerator Physics Issues in eRHIC, In Proc. of the 2nd eRHIC Workshop, New Haven, April 6–8, 2000, BNL-52592.

[165] The Electron Ion Collider, White Paper, eds. A. Deshpande, R. Milner and R. Venu-gopalan, BNL-68933-02/07-Rev.

[166] Proc. of the EIC Workshop, 28 February – 2 March, 2002, BNL-52663-V.2.

[167] Future Physics at HERA, Proc. of the Workshop 1995/96, vol. 2, eds. G. Ingelman, A. De Roeck and R. Klanner.

[168] M. W. Krasny, Physics of eA Collisions at RHIC and HERA, In Proc. of the 2nd eRHIC Workshop, New Haven, April 6–8, 2000, BNL-52592.

[169] H1 SpaCal Group, T. Nicholls et al., NIM **A374** (1976) 149.

[170] E. Barrelet, In Proc. of EIC Workshop, BNL-52663-V.2, BNL Feb. 26- March 2, 2002.

[171] L. Stodolsky, Phys,. Rev. Lett. **18**, (1967) 135.

[172] V. N. Gribov, Zh. Eksp. Teor. Fiz. **57** (1969) 1306 also Sov. Phys. JETP **30** (197) 709.

[173] S. J. Brodsky and J. Pumplin, Phys. Rev. **182** (1969) 1794.

[174] DESY–Hamburg Collab., V. Heynen et al., Phys. Lett. **B34** (1971) 651.

[175] Santa Barbara–SLAC Collab., D. O. Caldwell et al., Phys. Rev. **D7** (1973) 1362.

[176] Sheffield–Glasgow–DNPL Collab., G. R. Brookes et al., Phys. Rev. **D8** (1973) 2826.

[177] Yerevan–Lebedev-IHEP Collab., G. L. Bayatyan et al., Phys. Lett. **B56** (1975) 197.

[178] Cornell Collab., S. Michalowski et al., Phys. Rev. Lett. **39** (1977) 737.

[179] M. Arneodo, Phys. Rep. **240** (1994) 301.